Belly roll: an Ly6 protein regulating nociceptive escape behaviors by modulating peptidergic interneuron excitability in *Drosophila melanogaster*

LI, Kai

Table of Contents

Abstract

Ensuring an appropriate response to threatening stimuli is essential for the survival of organisms. Nociception, the sensory mechanism that enables animals to perceive and avoid potentially harmful stimuli, is a critical component of this process. Although considerable research has been conducted on nociceptive circuitry, our understanding of how genetic factors impact relevant escape responses is still limited.

In this study, I investigated the natural variation in nociceptive escape behavior among Drosophila larvae and conducted a comprehensive genome-wide association analysis to identify genetic variations underlying the behaviors. Through this analysis, I identified Belly roll (Bero), a member of the Ly6/α-neurotoxin family, as a potential regulator of nociceptive escape behavior in Drosophila. Using pan-neuronal knockdown screens and bero null mutant animal, I discovered the inhibitory role of Bero on escape behavior. Further investigations revealed that Bero is expressed in multiple subgroups of peptidergic neurons, including abdominal leucokinin-producing neurons (ABLK neurons). Knockdown of bero in ABLK neurons resulted in an enhanced escape behavior, while overexpression of bero led to suppression of the behavior. Additionally, I demonstrated that ABLK neurons respond to nociceptor activation, and optogenetic activation of ABLK neuron elicits bending behavior, which represents the initial phase within the overall sequence of escape behavior. Intriguingly, the knockdown of bero in ABLK neurons resulted in a reduction of persistent neuronal activity and an increase in evoked nociceptive responses. Given that the knockdown of bero enhanced escape behavior, these results suggest that the presence of Bero in these neurons acts as an inhibitory factor.

In summary, this study unveils the genetic regulation of nociceptive escape behavior in Drosophila larvae, highlighting the significance of ABLK neurons and the inhibitory influence of Bero. These findings contribute to our understanding of modulation of escape responses in Drosophila melanogaster larvae.

Abbreviation

5-HT1B	5-hydroxytryptamine receptor 1B
ABLK	Abdominal leucokinin-producing neurons
ALK	Anterior LK neurons
ATR	All-*trans* retinal
Bero	Belly roll
bHLH	Basic Helix-Loop-Helix
CNS	Central Nervous System
CRISPR	Clustered Regularly Interspaced Short Palindromic Repeats
DGRP	*Drosophila* melanogaster Genetic Reference Panel
DH44	Diuretic hormone 44
DnB neurons	Down-and-Back neurons
DSPR	*Drosophila* Synthetic Population Resource
EH neurons	Eclosion Hormone-producing neurons
GABAergic	Gamma-aminobutyric acid-ergic
GPI	Glycosylphosphatidylinositol
Gr28b	Gustatory receptor 28b
GtACR1	*Guillardia theta* anion channelrhodopsin-1
GWA	Genome-wide association
HPA	Heat Probe Assay
InR	Insulin-like receptor
IPC	Insulin-Producing Cell
Kir2.1	Inward rectifying potassium channel 2.1
LHLK	Lateral horn LK neurons
LK	Leucokinin
Lkr	Leucokinin receptor
LHLK	Lateral horn LK neurons
LY6/α-neurotoxin	Lymphocyte antigen 6/alpha-neurotoxin
mCSIs	Medial clusters of C4 da second-order interneurons
nAChR	Nicotinic acetylcholine receptor

OA	Octopamine
PCR	Polymerase Chain Reaction
Qvr	Quiver
Rdl	Resistance to dieldrin
RNAi	RNA interference
SELK	Suboesophageal LK neurons
SNP	Single Nucleotide Polymorphism
sNPF	Short neuropeptide F
Sss	Sleepless
TA	Tyramine
Tβh	Tyramine beta-Hydroxylase
Tdc2	Tyrosine Decarboxylase 2
TRPA1	Transient receptor potential ankyrin 1
UAS	Upstream activating sequence
UV	Ultraviolet
VNC	Ventral Nerve Cord
YFP	Yellow fluorescent protein

Chapter 1

Introduction

Chapter 1. Introduction

1-1. *Drosophila* larval escape behavior

Appropriate response to threatening stimuli is of utmost importance for the survival of organisms (Branco and Redgrave, 2020; Burrell, 2017; Chin and Tracey, 2017; Im and Galko, 2012; Peirs and Seal, 2016). Nociception, a fundamental sensory mechanism that allows animals to perceive and avoid potentially harmful stimuli, plays a critical role in this process. Nociception involves the activation of specialized neurons called nociceptors, which are responsible for detecting different forms of potentially damaging stimuli in the environment, including heat, mechanical pressure, and chemical irritants. Notably, in response to harmful stimuli like aggressive mechanical stimulation caused by parasitoid wasp attacks, *Drosophila melanogaster* larvae exhibit standard escape responses characterized by an instantaneous and abrupt bending motion followed by a subsequent rolling motion in a spiraling pattern (Hwang et al., 2007; Onodera et al., 2017; Tracey et al., 2003). Class IV dendritic arborization neurons (Class IV neurons), located beneath the body wall, have been identified as the nociceptors involved in this process (Tracey et al., 2003). Class IV neurons serve as polymodal nociceptors, capable of responding to diverse classes of noxious stimuli characterized by distinct physical properties. These stimuli include mechanical stimuli, noxious high temperature, as well as UV or blue light (Hwang et al., 2007; Im and Galko, 2012; Xiang et al., 2010). Through a series of investigations, researchers have successfully identified the relevant receptors present in Class IV neurons. Specifically, *Drosophila* TRPA1 and Painless receptors have been implicated in mediating thermal nociception (Hwang et al., 2012; Tracey et al., 2003; Zhong et al., 2012) while Gr28b receptor is involved in sensing short-wavelength light stimuli (Xiang et al., 2010). Additionally, other

distinct types of neurons have been elucidated as nociceptors for specific noxious stimuli, including v'td2 neurons, responsive to noxious light stimuli, and Class III dendritic arborization neurons (Class III neurons), activated by noxious cold stimuli (Imambocus et al., 2022; Turner et al., 2016).

1-2. The modulation of *Drosophila* larval escape behavior

The modulation of escape behavior is dependent on environmental conditions, as well as the intensity and modality of stimuli in both vertebrates and invertebrates. These stimuli are detected and processed in a complex neuronal network that is influenced by genetic variation, and which integrates both internal and external sensory information (Burnett et al., 2016; Jennings et al., 2014; Mu et al., 2012; Ohyama et al., 2015). Peptidergic neuromodulation is a vital component of this network, contributing significantly to the processing of neuronal information. (Nässel and Winther, 2010; Taghert and Nitabach, 2012).

In *Drosophila* larvae, recent investigations have revealed several important components within the nociceptive neural circuitry (Burgos et al., 2018; Hu et al., 2017; Ohyama et al., 2015; Takagi et al., 2017; Yoshino et al., 2017). These studies have identified second-order interneurons of Class IV neurons, such as mCSIs, A08n neurons, DnB neurons, Wave neurons, and Basin neurons, as well as higher-order command neurons like Goro neurons. Additionally, a number of genes and neurotransmitters have been identified as context-dependent modulators of the escape behavior (Dason et al., 2019; Hu et al., 2017; Kaneko et al., 2017). Among these modulators, there is the *foraging* gene, which exhibits genetic variations leading to differences in nociceptive responses. Serotonin has been found to inhibit the nociceptor presynaptic terminals, while short neuropeptide F (sNPF) facilitates mechano-nociceptive behavior.

1-3. Overview of this study

Most of the research on the nociceptive neural circuitry has relied on connectomic approaches, but our study utilized a genetic approach to investigate nociceptive modulation further. Notably, I observed considerable natural variation in nociceptive escape behavior among *Drosophila melanogaster* larvae. This broad range of behavioral differences enabled us to conduct an objective genome-wide association (GWA) analysis aimed at identifying genetic variations that impact nociceptive escape behaviors.

This study has shown that the Ly6/α-neurotoxin family protein Belly roll (Bero) acts as a modulator of peptidergic interneuron excitability, thereby facilitating *Drosophila* nociceptive escape behaviors. The *bero* gene was identified through GWA analysis, and its role in regulating nociception was validated using pan-neuronal *bero* knockdown and null mutant animals. ABLK neurons were identified as the *bero*-expressing neurons, and I found that *bero* knockdown in ABLK neurons enhanced escape behaviors similar to *bero* mutants. Additionally, ABLK neurons were found to respond to nociceptor activation and initiate nociceptive escape behavior. Our findings suggest that ABLK neurons may integrate external and internal sensory stimuli, thereby orchestrating nociceptive escape behaviors, and that *bero* plays an essential role in regulating their persistent activities and evoked nociceptive responses.

Chapter 2

Results

Chapter 2. Results

Section 1. Identification of *belly roll*

2-1-1. Wild-type strains of the *Drosophila melanogaster* Genetic Reference Panel displays natural variation in their nociceptive responses

When exposed to harmful thermal stimuli, *Drosophila* larvae display predictable nociceptive reactions characterized by bending and rolling movements (Figure 1; Tracey et al., 2003). Using the Heat Probe Assay (HPA), a technique developed by Tracey et al. (2003), we observed a significant difference in escape behavior (characterized by rolling latency) between two commonly used *Drosophila melanogaster* strains, w^{1118} and *Canton-S* (Figure 2). To evaluate the natural variation in nociceptive responses, we utilized the *Drosophila melanogaster* Genetic Reference Panel (DGRP; Huang et al., 2014; MacKay et al., 2012), a collection of wild-caught *Drosophila* lines. We measured rolling behavior in 38 representative inbred wild-type strains of DGRP and found considerable variation in behavior, with strain-specific median rolling latency ranging from 2.83 s to 10 s and rolling probability within 10 seconds ranging from around 30% to almost 100% (Figures 3A and 3B). We classified the probability of rolling into three response categories (rolling probability within 2 seconds, 5 seconds, and 10 seconds) using previous research as a basis (Onodera et al., 2017; Terada et al., 2016; Tracey et al., 2003). A correlation analysis was employed, revealing a strong association among the three response classes (Figure 3C). In order to detect genetic variants associated with the behavioral differences, we conducted numerous rounds of Genome-Wide Association (GWA) mapping analyses with the aid of a publicly accessible online tool called DGRP 2.0. The analyses utilized four statistical metrics that are mutually dependent to some extent to characterize larval rolling behavior, which include

median latency, average latency, rolling probability within 5 seconds, and rolling probability within 10 seconds (Figure 4A; Materials and Methods). At a commonly used P-value threshold of 1.0×10^{-5} in previous DGRP studies, we discovered a total of 42 genetic variants associated with the nociceptive behavioral variation, which comprised 37 single nucleotide polymorphisms (SNPs), two deletions, and three insertions located in or near 36 candidate genes (Figure 4B, Table S1 and S2; Mackay and Huang, 2018).

2-1-2. *CG9336*, also referred to as *belly roll* (*bero*), was identified via an RNAi knockdown screening of potential candidate genes

To investigate the effects of the candidate genes identified by the GWA analyses on nociceptive responses, a secondary functional screen was conducted using the Heat Probe Assay (HPA) in combination with pan-neuronal RNAi-mediated gene knockdown. Through the evaluation of 17 currently available RNAi strains, we observed a notable reduction in rolling latency upon pan-neuronal knockdown of the *CG9336* gene (Figure 5; Table S2). The gene was named as "*belly roll*" (*bero*), inspired by a high-jump style in athletics.

In order to ascertain the specificity of the phenotype resulting from *CG9336* suppression, we generated two distinct short-hairpin RNAs (shRNAs) targeting *CG9336* (shRNA#1 and #2; Figure 6A; Methods). In an initial HPA assessment, both shRNAs demonstrated a decrease in rolling latency, with shRNA#2 exhibiting a more pronounced effect (Figure 6B). Consequently, the efficacy of shRNA#2 was confirmed by employing a protein-trap strain, *bero*-YFP (CPTI-001654; Lowe et al., 2014), wherein the native Bero protein is fused with the mVenus, a variant of yellow fluorescent protein (Figures 6C and 6D; Methods). During the further evaluation, I performed the HPA using two sets of animals: the *nSyb>attP2* control group and the pan-neuronal *bero* knockdown group (*nSyb>bero RNAi*$^{shRNA\#2}$) and observed significant reduction of

rolling latency upon the *bero* knockdown (Figure 7). To prevent any potential non-specific effects from leaky expression of UAS transgenes, I conducted effector-control tests for *UAS-bero shRNA#2* (as well as other UAS transgenes in subsequent experiments). Since the genomic background can influence the observed phenotype (Figure 2), and considering that the driver strains used in this study may have distinct genomic backgrounds, I compared the phenotypes of three pairs of effector-control tests for *UAS-bero shRNA#2* with different genomic backgrounds. Although the *UAS-bero shRNA#2* control animal with different backgrounds exhibited varying rolling latency, within each group, both the *UAS-bero shRNA#2* control animal and their corresponding controls exhibited comparable rolling behavior (Figure 7). This suggests that there was no leaky expression of the UAS transgenes.

2-1-3. The Bero protein is a member of the Ly6/α-neurotoxin protein superfamily

bero encodes a member of the Ly6/α-neurotoxin protein superfamily. This protein family is distinguished by its three-finger structure, encompassing a diverse range of membrane-tethered and secreted polypeptides (Loughner et al., 2016). Several bioinformatics tools were employed to analyze and characterize the Bero protein (Figure 8). The amino terminal signal peptide was identified using SignalP - 5.0 (Almagro Armenteros et al., 2019). Two potential glycosylation sites were identified through NetNGlyc - 1.0 (Gupta and Brunak, 2001). The presence of a GPI-anchor site was predicted using Big-PI Predictor (Eisenhaber et al., 1999). Additionally, the putative transmembrane region was determined using TMHMM - 2.0 (Krogh et al., 2001). Furthermore, a three-dimensional model of Bero, including its five putative disulfide bridges, was generated using AlphaFold2 and visualized utilizing PyMOL (Jumper et al., 2021; Figure

8C). These structural characteristics are commonly observed in the Ly6/α-neurotoxin protein superfamily.

2-1-4. Nociceptive escape behavior is negatively regulated by neuronal expression of *bero*

The SNP associated with *bero*, identified in GWA analyses as 2L_20859945_SNP, resides within the second intron of *CG9336* isoform A (FBtr0081427). The DGRP core 40 lines exhibit two nucleotide variations for this SNP, with a minor allele (Cytosine) and a major allele (Thymine). Upon reviewing the HPA results of the 38 DGRP core lines, it was observed that the majority of lines carrying the minor allele (C) of *bero* exhibited increased sensitivity to rolling in response to noxious thermal stimuli compared to lines with the major allele (T) (Figure 9A). Given these observations and the results of our *bero* knockdown experiments, I hypothesized that individuals carrying the minor allele (C) of *bero* might exhibit lower expression levels of the gene compared to those carrying the major allele (T). To test this hypothesis, we performed reverse transcriptase PCR to compare the expression levels of *bero* in the larval central nervous system (CNS) among four DGRP strains that displayed markedly rapid or slow behavioral responses. The results indicated that individuals with the minor allele (C) exhibited reduced expression levels of *bero* (Figure 9B). By employing an online sequence analysis tool utilizing JASPAR 2022 (Castro-Mondragon et al., 2022), I conducted predictions regarding the adjacent nucleotide sequences of the *bero*-associated SNP. The analysis suggested that these sequences may serve as potential target sites for specific transcription factors that regulate the expression of *bero* within CNS (Table S3).

Moreover, we created a *bero* null mutant strain through the application of CRISPR-mediated mutagenesis, resulting in the complete deletion of the entire protein-coding sequence

(Figure 10A; Methods). Subsequently, the *bero* null strain was subjected to eleven generations of outcrossing with *Canton-S*, leading to the establishment of an isogenic line. By employing the HPA, a shortened rolling latency was observed in both *bero* heterozygous ($bero^{KO}$/+) and homozygous ($bero^{KO}/bero^{KO}$) mutant animals in comparison to the wild-type *Canton-S* control animals (Figure 10B). Collectively, these findings provide compelling evidence supporting the notion that neuronal expression of *bero* exerts a negative regulatory influence on nociceptive escape behavior.

2-1-5. *bero* is expressed in several subgroups of peptidergic neurons in the larval CNS

Subsequently, our aim was to identify the specific neuronal populations within the larval CNS that express *bero*. To achieve this, we investigated the co-localization between candidate neurons, labeled using distinct GAL4-drivers that drive a CD4:tdTomato fusion protein, and *bero*-expressing neurons labeled in the *bero*-YFP strain. I observed the absence of *bero*-YFP expression in the Class IV neurons (nociceptors) as well as in the downstream neurons (Basin neurons and Goro neurons) known to be essential for the nociceptive escape behavior (Figure 11A; Ohyama et al., 2015). In accordance with these findings, targeted knockdown of *bero* specifically in these nociceptive neurons did not induce any changes in the rolling latency (Figure 11B). In contrast, we detected the expression of *bero*-YFP in distinct clusters of peptidergic neurons, identified by the bHLH transcription factor *dimmed* (*dimm*). These include insulin-producing cells (IPCs) and a specific subgroup of Eclosion hormone-producing neurons (EH neurons) within the larval brain. Furthermore, *bero*-YFP expression was also observed in abdominal Leucokinin-producing neurons (ABLK neurons) situated in the lateral area of the abdominal ganglia within the larval ventral nerve cord (VNC; Figures 12A and 12B). Consistent

with our findings, a recent study on single-cell transcriptomic atlas demonstrated a notable enrichment of *bero/CG9336* specifically in peptidergic neurons (Corrales et al., 2022). Moreover, Bero expression was detected in specific non-neuronal tissues, including midline glia (Figure 12A). However, I did not investigate the function of Bero in non-neuronal tissues as it falls outside the scope of this study.

Section 2. Explore the function of ABLK neurons and the role of *bero* in ABLK neurons

2-2-1. The impact of *bero* expression in ABLK neuron on nociceptive escape behavior

To determine the specific neuronal subgroups reliant on *bero* expression for the negative regulation of nociceptive escape behavior, I performed the HPA and measured the rolling latency of larvae subjected to cell type-specific RNAi knockdown targeting *bero*. The experiment revealed that the suppression of *bero* through the utilization of *Lk-GAL4*, a driver specific to Leucokinin-producing neurons, resulted in a notable augmentation of escape behavior (Figure 13). Conversely, the inhibition of *bero* expression through the implementation of either *Eh-GAL4*, a driver specific to EH neurons, or *Ilp2-GAL4*, a driver specific to IPCs, did not yield any discernible alterations in nociceptive escape behavior (Figure 13).

Drosophila larval LK neurons in the CNS can be categorized into four different subgroups based on their anatomical distribution: anterior LK neurons (ALKs) and lateral horn LK neurons (LHLKs) in the brain region, suboesophageal LK neurons (SELKs) in the suboesophageal zone; and abdominal LK neurons (ABLKs) in the VNC (de Haro et al., 2010). Through the analysis of the co-localization between *bero*-YFP and CD4:tdTomato, driven by the

Lk-GAL4 driver, in high-resolution individual optical sections, I observed the expression of *bero* specifically in the seven pairs of ABLK neurons and their neurites, while no expression was detected in any other LK neurons (Figures 14). In agreement with these findings, all seven pairs of neurons labeled with *bero*-YFP showed immunoreactivity for Leucokinin (Figure 14B). Using high-resolution individual optical sections, it was further revealed that Bero is localized on both the plasma membrane and internal membrane of ABLK neurons (Figure 14B). In order to investigate whether the neurites expressing Bero corresponded to dendrites or axons, we employed DenMark as an axon terminal marker and synaptotagmin-eGFP (syt:eGFP) as a dendrite marker. The intersectional flip-out technique (Bohm et al., 2010; Simpson, 2016) was employed to selectively express these markers in ABLK neurons, revealing the distribution of Bero in both dendritic and axonal regions of the neurons (Figure 15).

Moreover, to examine the influence of *bero* expression in ABLK neurons on the modulation of nociceptive escape behavior, we generated a *UAS-Bero:FLAG* transgenic strain and employed the intersectional flip-out method to induce targeted overexpression of *bero* exclusively in ABLK neurons (Materials and Methods; Figures 16A and B). Subsequently, I observed that the larvae with overexpression of *bero* in ABLK neurons exhibited an increased rolling latency in HPA (Figure 16C). In contrast, during the effector-control test, both the *UAS-Bero:FLAG* control animal and the corresponding control groups exhibited similar rolling latency (Figure 16C). These observations highlight the influential role of *bero* in the modulating nociceptive responses within the ABLK neurons. Therefore, the focus of my research revolves around exploring the physiological characteristics of ABLK neurons and elucidating the functional significance of *bero* within these neurons.

2-2-2. ABLK neurons showed sustained oscillatory activities and stimulus-induced nociceptive responses

We proceeded to investigate whether ABLK neurons function as components of downstream circuits in nociceptive pathways by assessing their responsiveness to nociceptor (Class IV neurons) stimulation. We monitored calcium responses in ABLK neurons by measuring changes in fluorescence intensity of jRCaMP1b (Dana et al., 2016), a red fluorescence Ca^{2+} indicator, in *Drosophila* larval fillet preparations. Consistent with previous research, spontaneous sustained fluctuations in intracellular calcium concentration were observed within both the cell bodies and neurite regions of ABLK neurons (Figure 17; Okusawa et al., 2014). Significantly, the optogenetic stimulation of nociceptors using ChR2.T159C (a modified form of channelrhodopsin-2; Berndt et al., 2011) elicited modest yet reliable acute neuronal responses in ABLK neurons, indicating their capacity to detect nociceptive stimulation (Figures 18A and 17C; Hu et al., 2020). Given that optogenetic activation in *Drosophila* requires the presence of supplementary all-*trans* retinal (ATR) in the food, larvae raised on a medium without supplementary ATR were utilized as a control group. The control larvae also exhibited an increase in Ca^{2+} levels upon optogenetic stimulation of nociceptors, however, the rising phase of the Ca^{2+} response occurred prior to the initiation of blue light illumination, suggesting that the increase in Ca^{2+} levels may be explained by the sustained oscillatory calcium concentration observed in ABLK neurons.

2-2-3. In ABLK neurons, *bero* facilitates sustained oscillatory activities and suppresses stimulus-induced nociceptive responses

In order to gain deeper insights into the physiological functions of *bero* in ABLK neurons, we conducted experiments to examine the potential impact of *bero* knockdown on both sustained

oscillatory activities and acute nociceptive responses of these neurons. Our investigation revealed that the knockdown of *bero* significantly reduced the sustained oscillatory activities in ABLK neurons (Figures 17A and 17B). On the other hand, the knockdown of *bero* resulted in a surge in the level of optogenetic-induced nociceptive responses (Figures 18). Considering the observed enhancement of nociceptive escape behavior in the HPA experiments due to *bero* knockdown (Figure 13), it is reasonable to conjecture that the acute nociceptive responses in ABLK neurons play a crucial role in facilitating the escape behavior.

Based on the observed phenotype of *bero* knockdown affecting spontaneous sustained activities in ABLK neurons, we conducted a thorough behavioral analysis of undisturbed free locomotion in larvae with *bero* knockdown. Average velocity, the fraction of frames with forward movement out of the total frames, and the fraction of frames with head casting out of the total frames were measured as characteristic parameters of free locomotion. We observed that the free locomotion of larvae was not affected by *bero* knockdown (Figures 19).

Notably, in the presence of supplementary ATR, *bero* knockdown animals exhibited a notable enhancement in the sustained fluctuations observed in ABLK neurons when compared to the control group (Figure 18A). This can be explained by the fact that the 561-nm laser employed for jRCaMP1b excitation can mildly activate nociceptors through the activation of ChR2.T159C. Subsequently, the weak activities in nociceptors elicited neuronal responses in ABLK neurons. In addition, the suppression of *bero* expression rendered ABLK neurons more responsive to these nociceptive inputs than control groups, elucidating the reason behind the increased sustained fluctuations. Hence, the baseline neural activities observed in the presence of supplementary ATR may not accurately reflect the spontaneous sustained activity. Therefore, we focused solely on comparing the spontaneous activity in the absence of supplementary ATR.

2-2-4. Optogenetic activation of ABLK neurons elicited bending behavior

To investigate the relationship between activities in ABLK neurons and nociceptive escape behaviors, I employed optogenetic techniques to directly stimulate the neurons using CsChrimson, a red light-activated cation channel (Klapoetke et al., 2014). Initially, I stimulated all LK neurons and observed a prominent induction of rolling behavior upon exposure to red light illumination, a response that was absent in control larvae (Figure 20A). Subsequently, I utilized the intersectional flip-out technique to specifically express CsChrimson in either ABLK or SELK neurons (Figure 20B and 20C). Unexpectedly, the optogenetic stimulation of ABLK neurons predominantly elicited bending behavior rather than rolling (Figure 20A). The bending behavior is regarded as the initial phase within the overall sequence of escape behavior (Burgos et al., 2018). On the other hand, the activation of SELK neurons elicited vigorous rolling behavior in all larvae tested (Figure 20A). The recorded videos of larval behaviors were further subjected to analysis using FIMTrack software (Risse et al., 2017) and a customized MATLAB classifier based on support vector machine (SVM) algorithm. The FIMTrack analysis enabled the tracking and generation of distinct behavioral features exhibited by the larvae. Subsequently, a decoding analysis was conducted using the MATLAB classifier to identify the occurrence of escape behavior in each frame of the video. This impartial automated analysis further demonstrated that the activation of both LK neurons and SELK neurons consistently induced robust and sustained rolling behavior in all tested larvae (Figures 21A, 21B and 21D). However, the activation of ABLK neurons resulted in only sporadic instances of abrupt escape behavior, which does not qualify as complete rolling (Figures 21B and 21C).

2-2-5. Proper dynamics of evoked nociceptive activities in ABLK neurons plays a crucial role in governing the nociceptive escape behavior

Given these findings and the outcomes of *bero* knockdown experiments, I postulate that the evoked activity of ABLK neurons has the potential to facilitate nociceptive escape behavior. To investigate this hypothesis, I performed the HPA with animals expressing Kir2.1, an inward rectifying potassium channel, selectively in ABLK neurons. Remarkably, the larvae with ABLK neurons silenced by Kir2.1 exhibited a slight decrease in rolling latency (Figure 22). In the Discussion Chapter, I explore multiple scenarios to explain the unexpected results. In short, this outcome can be ascribed to the suppression of sustained activity in ABLK neurons, which potentially disinhibits the evoked nociceptive activity. In an alternative scenario, the prolonged inhibition of ABLK neurons has the potential to induce adaptations in the nociceptive circuitry throughout the developmental stage of larvae.

To address the limitations associated with prolonged manipulation, I employed transient optogenetic manipulation in the HPA to modulate the activities of the neurons. In greater detail, I synchronized the optogenetic activation or inhibition of ABLK neurons with the initial one second of noxious thermal stimulation, ensuring that both the heat stimulation and optical modulation of the neurons occurred nearly simultaneously (Figure 23A; see Method for detailed information). To transiently silence ABLK neurons, I specifically expressed *Guillardia theta* anion channelrhodopsin-1 (GtACR1; Mohammad et al., 2017) in ABLK neurons. This resulted in a strong impairment of escape behavior and an increase in rolling latency in the larvae raised with supplementary ATR (Figure 23C). In the effector-control tests for *UAS-GtACR1,* both control groups, with or without supplementary ATR, exhibited similar rolling latency (Figure 23C). These observations indicated that evoked activity of ABLK neurons plays a critical role in

facilitating nociceptive escape behavior. Surprisingly, simultaneous stimulation of ABLK neurons via CsChrimson in the HPA led to a notable increase in rolling latency as well, while the effector-control tests for *UAS-CsChrimson* showed similar rolling latency in both control groups, with or without supplementary ATR (Figure 23D). These observed contrasting findings highlight the significance of the appropriate dynamics of acute activity in ABLK neurons for the facilitation of nociceptive escape behavior. Additionally, it suggests that the neuronal activity elicited through optogenetic stimulation does not align with the naturally evoked nociceptive activity in ABLK neurons. I also discuss additional alternative scenarios to explain results in the Discussion Chapter. The rolling latency of larvae expressing myr:GFP in ABLK neurons was similar in both groups, with or without supplementary ATR, during light stimulation, suggesting that the addition of supplementary ATR does not affect the nociceptive escape behavior (Figure 23B).

2-2-6. DH44 and octopamine serve as vital neurotransmitters in ABLK neurons, facilitating nociceptive escape behavior

Finally, my investigation focused on the functional neurotransmitters originating from ABLK neurons that contribute to the augmentation of nociceptive escape behavior. Earlier investigations have documented the synthesis of corticotropin-releasing factor (CRF)-like diuretic hormone (diuretic hormone 44, DH44; Zandawala et al., 2018) and leucokinin (LK; de Haro et al., 2010) within ABLK neurons. Through the analysis of the co-localization between distinct neurotransmitter markers and CD4:tdGFP, driven by the *Lk-GAL4* driver, we further detected the expression of tyrosine decarboxylase 2 (Tdc2) in ABLK neurons (Figure 24A). This enzyme plays a crucial role in the synthesis of octopamine (OA) and tyramine (TA) (Figure

24B). In addition, our immunohistochemistry staining revealed that ABLK neurons do not exhibit immunoreactivity for GABAergic, glutamatergic or cholinergic markers (Figure 24A).

I then proceeded to investigate the necessity of these neurotransmitters synthesized in ABLK neurons in facilitating nociceptive escape behavior. To achieve this, I conducted tests on the rolling escape behavior of larvae with suppressed expression of *Dh44*, *Lk*, or *Tyramine β hydroxylase (Tβh)* in ABLK neurons using RNA interference. Among them, *Tβh* serves as a critical enzyme for the conversion of tyramine into octopamine (Figure 24B). I observed that the inhibition of *Dh44* or *Tβh* resulted in an increase in the rolling latency, suggesting the functional significance of DH44 and octopamine in facilitating nociceptive escape behavior (Figure 25A). In the effector-control experiments involving *UAS-DH44 RNAi and UAS-Tβh RNAi,* both the control groups and the *RNAi* transgene groups displayed comparable rolling latency (Figure 25A). Nevertheless, although there was an increase in the rolling latency when *Lk* was suppressed in ABLK neurons, the *UAS-Lk RNAi* transgene group in the effector-control test also exhibited a significant elevation in rolling latency (Figure 25B). This suggests that the observed phenotype could potentially be attributed to unintended leaky expression of the UAS transgene.

2-2-7. Examining the relevance of ABLK neuronal receptors in facilitating nociceptive escape behavior

A prior investigation demonstrated that, under the condition of weak nociceptor stimulation, the suppression of the ionotropic $GABA_A$ receptor Resistance to dieldrin (Rdl) specifically in LK neurons resulted in an augmented rolling probability (Hu et al., 2020). In line with this finding, my study revealed that the specific suppression of *Rdl* in ABLK neurons resulted in a decreased rolling latency in response to thermal stimulations with a relatively lower temperature of 44°C (Figure 26A).

It has been reported that the modulation of the 5-HT1B receptor affects the sustained oscillatory activity level of ABLK neurons, subsequently influencing larval turning behavior (Okusawa et al., 2014). Therefore, I investigated the impact of selectively suppressing the 5-HT1B receptor in ABLK neurons on nociceptive escape behavior through HPA experiments. My results revealed that the inhibition of *5-HT1B* did not produce any notable effects (Figure 26B).

In conclusion, our results provide evidence that ABLK neurons play a crucial role in facilitating nociceptive escape behavior in *Drosophila melanogaster* larvae. We have identified DH44 and octopamine as significant neurotransmitters involved in the modulation of ABLK neurons for this behavior. Moreover, our study highlights the pivotal role of *bero* in both generating a heightened level of sustained oscillatory activities and suppressing the induced nociceptive responses in ABLK neurons. Consequently, the presence of *bero* in ABLK neurons inhibits the occurrence of nociceptive escape behavior (Figure 27).

Chapter 3

Discussion

Chapter 3. Discussion

3-1. Natural variability in *Drosophila* larval nociceptive escape behaviors

In this investigation, I have unveiled a wide range of naturally occurring variations in nociceptive escape behaviors observed in *Drosophila melanogaster* larvae. Nociceptive escape behavior has been documented as an effective mechanism employed by larvae to evade parasitization by *Leptopilina boulardi* parasitoid wasps, as reported in previous studies (Hwang et al., 2007). These parasitoid wasp species lay their eggs inside the bodies of *Drosophila* larvae. The eggs develop as parasites, consuming the tissues of their host. Subsequently, they undergo pupation and emerge as independent adults. Since the process inevitably leads to the death of the host, the parasitization serves as a crucial factor in regulating the *Drosophila* population size. Therefore, the behavioral variations observed within the *Drosophila* population can confer adaptive benefits in dynamic environments, particularly in the presence of geographically and seasonally diverse parasitoid wasp species (Bergland et al., 2014; Fleury et al., 2004). In scenarios where parasitoid wasp abundance is elevated, it can be advantageous for larvae to exhibit heightened responsiveness to noxious stimuli. Conversely, in environments with lower wasp populations, excessive nociceptive sensitivity may offer limited protective benefits or hinder the efficient execution of vital behaviors, such as foraging.

Through an impartial genome-wide association (GWA) analysis (Figure 4B, Table S1 and S2), I successfully identified genetic variants associated with nociception. I opted to employ the DGRP2.0 approach as it is a more suitable method for elucidating the genetic factors underlying the observed behavioral variations (Mackay and Huang, 2018). Despite the availability of the *Drosophila* Synthetic Population Resource (DSPR), which primarily focuses

on evaluating the influence of local haplotypes on specific phenotypes, it poses challenges in identifying the specific molecular variants associated with the phenotype (Long et al., 2014). Furthermore, although the DSPR provides certain advantages for behavioral studies through the use of recombinant inbred lines derived from multiple founder strains, it cannot encompass the full spectrum of genetic variations present in natural populations. Therefore, the DGRP2.0 approach was considered superior for analyzing behavioral variations due to its more comprehensive representation of genetic diversity.

The nociception-associated single nucleotide polymorphism (SNP) within the *bero* locus (2L_20859945_SNP) resides in an intronic region, indicating its potential influence on gene expression. Remarkably, our investigation revealed a substantial association between this SNP and the expression level of *bero*: individuals carrying a homozygous Cytosine allele exhibited lower *bero* expression levels and demonstrated heightened sensitivity to noxious heat stimuli in comparison to those with a homozygous Thymine allele. In line with these findings, experiments involving pan-neuronal knockdown of *bero*, as well as animals carrying *bero* heterozygous mutant ($bero^{KO}/bero^{+}$) and homozygous mutant ($bero^{KO}/bero^{KO}$) genotypes, consistently exhibited reduced rolling latency. These observations suggest that the downregulation of *bero* expression significantly influences nociceptive escape behavior. Noteworthy, the majority of animals with a homozygous mutant ($bero^{KO}/bero^{KO}$) genotype in the *Canton-S* background did not reach adulthood, indicating that *bero* has a crucial role in animal development, in addition to its involvement in nociception.

During the secondary functional RNAi screen, which aimed to evaluate the nociception-related function of 17 candidate genes, it was observed that only a single pan-neuronal RNAi knockdown exhibited a notable impact on nociceptive escape behavior (Figure 5). One possible

explanation for the low number of identified variants is that the majority of the variants detected through GWA analysis may be false positives. This inference is supported by the fact that the *P*-values associated with these variants do not reach the Bonferroni-corrected significance threshold of 6.95×10^{-8}. Another plausible explanation is that certain detected variants may be gain-of-function mutations, which could account for the inability of RNAi knockdown to replicate the observed phenotype. A third potential scenario is that certain detected variants may be necessary exclusively in non-neuronal tissues to influence the behavior, which falls outside the scope of this study. It will be interesting to validate the potential gain-of-function variants and variants in non-neuronal tissues in future research. I also observed that the variants in crucial nociception-related genes, such as *Transient receptor potential cation channel A1* (*TRPA1*) and *painless*, had minimal impact on the escape behaviors. One possible explanation is that these genes are indispensable for survival in natural environments and therefore lack functional variants in natural populations.

3-2. Mechanisms underlying neuronal activity regulation by *bero*

Bero has been characterized as a constituent of the Ly6/α-neurotoxin protein superfamily (Hijazi et al., 2009); nevertheless, there remains a dearth of knowledge regarding its biological functionalities (Khan et al., 2017). Significantly, Ly6 proteins in mammals demonstrate diverse effects on the functional activity of distinct subtypes of nicotinic acetylcholine receptors (nAChR), thereby effectively modulating neuronal excitability (Tsetlin, 2015). In various insect species, including the firefly *Pyrocoelia rufa* and the brown planthopper *Nilaparvata lugens*, the presence of *Pr-lynx1* and *Nl-lynx1/Nl-lynx2*, respectively, has been documented to augment the amplitudes of currents elicited by acetylcholine administration (Choo et al., 2008; Liu et al., 2009). Within *Drosophila*, the Ly6-like protein known as Quiver (Qvr)/Sleepless (Sss) exerts a

dual effect on sleep regulation, as it not only diminishes cholinergic synaptic transmission through the antagonistic modulation of nAChR but also diminishes neuronal excitability by amplifying the expression levels and open probability of Shaker potassium channels (Wu et al., 2014, 2010). Within the scope of my research, the downregulation of *bero* was found to eliminate sustained oscillatory activities and elicit heightened nociceptive responses in ABLK neurons. The role of *bero* in these two different neuronal activities can be attributed to at least two plausible mechanisms. A plausible interpretation suggests that *bero* exerts regulation over the two neuronal activities by independently interacting with two different transmembrane proteins. Alternatively, it is conceivable that *bero* targets a specific protein essential for initiating sustained oscillatory activities, subsequently constraining the elicited nociceptive responses in ABLK neurons and consequentially suppressing nociceptive escape behavior (Figure 28). In the latter circumstance, the protein targeted by *bero* could potentially increase the intracellular calcium concentration, leading to interference with the opening of voltage-gated cation channels (Budde et al., 2002; Oh et al., 2021). As a result, the elicited nociceptive responses in ABLK neurons are suppressed. While the current model proposed is grounded in preliminary observations, it holds potential to serve as a conceptual framework for forthcoming investigations pertaining to the roles of *bero* and ABLK neurons in regulating nociceptive escape behaviors.

In both circumstances, the identification of Bero-interacting membrane proteins in ABLK neurons emerges as a crucial matter. Earlier investigations have demonstrated the expression of 5-hydroxytryptamine receptor 1B (5-HT1B; Okusawa et al., 2014), Insulin-like receptor (InR; Luo et al., 2013), Leucokinin receptor (Lkr; Okusawa et al., 2014), RYamide receptor (Veenstra and Khammassi, 2017), Ecdysis-triggering hormone receptor (ETHR; Kim et al., 2006), and

Leucine-rich repeat-containing G protein-coupled receptor 4 (Lgr4; Imambocus et al., 2022) within ABLK neurons. Among these receptors, 5-HT1B has been previously implicated in the preservation of sustained oscillatory activities (Okusawa et al., 2014). Nevertheless, my preliminary findings, employing the HPA, indicate that it is unlikely for 5-HT1B to function as the effectors of Bero protein (Figure 26B). Nonetheless, the determination of the specific Bero-interacting counterparts remains a crucial aspect that requires further investigation.

3-3. LK neurons and nociceptive escape behaviors

This research reveals the expression of *bero* within ABLK neurons, which governs the modulation of nociceptive escape behaviors. Consistent with my independent study (Figures 20A and 21A), prior investigations have reported that the activation of all LK neurons is adequate to elicit a robust rolling escape behavior (Hu et al., 2020; Imambocus et al., 2022). Moreover, through the application of the intersectional flip-out technique, I achieved precise activation of two discrete subgroups of LK neurons, namely ABLK and SELK neurons. Notably, both subgroups demonstrated responsiveness to nociceptive stimuli (Figure 18A; Hu et al., 2020). In a previous study, it was postulated that LK neurons decipher decision-related neuronal activity, and the activation of these neurons gives rise to nociceptive escape behavior (Hu et al., 2020). In this study, I demonstrated that the targeted activation of ABLK neurons does not elicit complete rolling behavior; instead, it induces bending behavior, which is recognized as an initial posture preceding rolling (Burgos et al., 2018; Figure 20A and 21A). Drawing from this observation, I postulate that the activation of ABLK neurons prompts the onset of rolling behavior. In line with this concept, my findings demonstrate that the downregulation of *bero* in LK neurons leads to heightened nociceptive responses in ABLK neurons (Figures 18A and 18D), coinciding with a reduction in rolling latency and an increased probability of rolling (Figure 13). Significantly,

within this study, I have provided the initial evidence showcasing that the activation of SELK neurons leads to the robust rolling behavior (Figures 20A and 21A), akin to the phenotype observed with the activation of well-known rolling command neurons, such as Goro or mCSI neurons (Ohyama et al., 2015; Yoshino et al., 2017). While not the primary focus of this study, it is imperative to investigate the presynaptic and postsynaptic circuitry associated with SELK neurons as a critical command circuitry underlying nociceptive rolling behavior.

Additionally, I demonstrated that both optogenetic stimulation and inhibition of ABLK neurons during noxious thermal stimulation in HPA impede rolling behavior (Figures 23C and 23D). These findings indicate that the maintenance of ABLK neuronal activity within a suitable physiological range and/or dynamic state is crucial for facilitating the observed behavior. This parallels a prior discovery that emphasized the significance of maintaining an optimal level of ABLK neuronal activity in regulating noxious light-evoked turning behavior (Okusawa et al., 2014). In more precise terms, I put forth a scenario that builds upon the Ca^{2+}-dependent inhibition of elicited excitation within ABLK neurons, as elucidated in the preceding discussion. Within this proposed scenario, the optogenetic stimulation of CsChrimson initiates membrane depolarization within ABLK neurons, leading to a significant influx of Ca^{2+} ions into the cytoplasm. This pronounced surge of Ca^{2+} ions hold the capability to inhibit voltage-gated cation channels (Budde et al., 2002; Oh et al., 2021), consequently suppressing subsequent nociceptive responses within ABLK neurons over an extended duration and impairing rolling behavior. An alternative scenario suggests that the optogenetic activation of ABLK neurons can induce not only prompt bending behavior but also impose a delayed inhibitory influence on subsequent nociceptive escape behaviors by modulating downstream circuits. In contrast, under optogenetic

inhibition, the activation of GtACR1 inhibits nociceptive responses in ABLK neurons, leading to an increased rolling latency.

Previous studies have demonstrated that the suppressing of LK neurons through Kir2.1-mediated mechanisms resulted in an augmented mechanonociceptive responses (Imambocus et al., 2022). In accordance with these previous findings, my results revealed that the Kir2.1-mediated suppressing of ABLK neurons led to a slight decrease of rolling latency in the HPA experiments (Figure 22). This effect differed from the impact observed with GtACR1-mediated inhibition (Figure 23C), which prompted the proposal of two potential scenarios to elucidate the distinction. In the first scenario, the hyperpolarization induced by Kir2.1 diminishes the sustained oscillatory activities, resulting in the disinhibition of elicited nociceptive responses in ABLK neurons and promoting nociceptive escape behavior. An alternative hypothesis proposes that persistent inhibition of ABLK neurons could potentially modulate the nociceptive circuitry during larval development, thereby contributing to an elevated level of nociceptive sensitivity. On the other hand, optogenetic inhibition mediated by GtACR1 transiently interferes nociceptive responses without altering the excitability of the neuronal network.

3-4. ABLK neurons: a neuromodulatory center for nociceptive escape behaviors

A neuromodulatory hub comprises a compact cluster of neurons that produce neuromodulators, receive a wide range of sensory and internal inputs, and regulate multiple physiological processes and behavioral outputs (Flavell et al., 2022). In this context, ABLK neurons possess the distinctive characteristics of such an organized network.

A previous investigation documented that ABLK neurons exhibit evoked neuronal activities following stimulation with blue light or UV, and these activities are necessary for eliciting light-avoidance behavior (Imambocus et al., 2022). Notably, the functions attributed to ABLK neurons in facilitating noxious light-avoidance behavior, as reported in prior studies, and initiating nociceptive rolling escape behavior, as evidenced by my research, are not contradictory or mutually exclusive. In fact, the simultaneous activation of nociceptors and exposure to blue light stimulation can synergistically promote the nociceptive rolling escape behavior (Wietek et al., 2017). These results suggest that in response to different types of noxious stimuli, ABLK neurons integrate multiple inputs and exhibit varied outputs, highlighting their capacity for sensory integration and modulation. Specifically, during noxious heat stimulation, the transient activities of ABLK neurons, characterized by appropriate dynamics, facilitate the rolling behavior. On the other hand, in response to blue light or UV stimulation, the evoked responses of ABLK neurons contribute to light-avoidance behavior. In future, it would be of great interest to explore whether the expression of *bero* in ABLK neurons exerts inhibitory effects on the UV light-induced responses within these neurons, leading to the suppression of light-avoidance behavior. Alternatively, it is worth investigating whether the inhibitory function of *bero* in ABLK neurons is specific to the activity induced by noxious heat stimulation.

ABLK neurons have established roles in controlling water balance and food intake in adult *Drosophila* (Liu et al., 2015; Zandawala et al., 2018b), indicating that the sustained oscillatory activities of these neurons may be associated with stresses related to dehydration and lack of nutrition. In this research, I have demonstrated that Bero protein plays a crucial role in maintaining the sustained oscillatory activities of ABLK neurons. Thus, if the hypothesis proposed in the previous section, stating that the sustained activities of ABLK neurons suppress

the elicited nociceptive responses, holds true, it suggests that the presence of *bero* facilitates the integration of stress signals with nociceptive signals in these neurons. In essence, the expression of *bero* in ABLK neurons potentially enables the down-regulation of nociceptive escape behavior based on the level of stress experienced by the organism. Conversely, in cases of *bero* knockdown or mutation, the sustained oscillatory activities of ABLK neurons are abolished, leading to a potential decoupling of stress inputs from nociceptive inputs in these neurons, thereby preventing stress signals from influencing nociceptive escape behavior. In specific natural environments, such as those characterized by an increased abundance of parasitoid wasps, *Drosophila* individuals harboring the minor allele (C) of *bero*, which results in reduced expression of *bero* in ABLK neurons, may potentially benefit from the postulated decoupling of stress inputs from the down-regulation of nociceptive responses.

My investigation uncovered the essential involvement of octopamine and DH44, released by ABLK neurons, in the facilitation of nociceptive escape behavior of *Drosophila* larvae. In mammals, corticotropin-releasing factor (CRF), which is an ortholog of DH44 in *Drosophila*, has been shown to enhance mechanosensitivity and nocifensive reflexes when released in the central amygdala (Bourbia et al., 2010; Ji et al., 2013; Johnson et al., 2015). CRF-expressing neurons in the central amygdala also play a significant role in mediating conditioned flight behavior, known as jump escape behavior, in mice (Fadok et al., 2017). Furthermore, CRF has been found to mediate stress-induced thermal hyperalgesia in rats (Itoga et al., 2016). These findings indicate a potential evolutionary conservation of DH44's role in facilitating nociceptive responses across insects and mammals.

In conclusion, my investigations have uncovered that *bero* exerts modulation over sustained oscillatory activities and stimulus-induced nociceptive activities within a specific

subset of *bero*-expressing neurons known as ABLK neurons in *Drosophila melanogaster* larvae. These neurons are responsible for initiating and facilitating the nociceptive escape behavior (Figure 27). Consequently, my findings propose the intriguing possibility that *bero* plays a vital role in ABLK neurons by detecting the stress levels experienced by larvae, integrating them with nociceptive inputs, suppressing the evoked nociceptive activities, and subsequently down-regulating the nociceptive escape behavior (Figure 28).

Chapter 4

Materials and methods

Chapter 4. Materials and methods

4-1. *Drosophila* strains

Drosophila melanogaster larvae were raised under controlled conditions, including a temperature of 25°C, 75-80% humidity, and a 12-hour light/dark cycle. They were fed standard fly food throughout the experiment. The transgenic strains used in this study were primarily maintained in either *yellow vermillion* (y^1, v^1) or *white* (w^{1118}) mutant backgrounds, unless specified otherwise. The detail genotypes and source of the fly lines used can be found in the Table S4, and they were mainly acquired from the Bloomington *Drosophila* Stock Center (BDSC), unless otherwise specified. No specific effects related to the sex of the flies were investigated in this study. Behavioral analysis involved the use of wandering 3rd instar larvae of both sexes, unless specified otherwise (at approximately 120 hours ± 12 hours after egg laying). For calcium imaging experiments, only female wandering 3rd instar larvae were used. The specific genotypes of the experimental and control animals can be found in the corresponding figure legends.

4-2. Production of plasmids and development of transgenic strains

- UAS-*bero* $^{\text{sh RNA\#1}}$ and UAS-*bero* $^{\text{sh RNA\#2}}$

The *bero* RNAi strains were produced following the procedure outlined by previous research (Ni et al., 2008). In brief, a pVALIUM20 vector was used to clone an annealed oligo DNA hybrid harboring one of the 21-nucleotide sequences targeting the coding region of *bero* (sh RNA#1: GCACCAAGGACGAGTGCAACG; sh RNA#2: CCTCTATGCCGTTCGTTAAGC). The complete sequences of the oligo DNA are provided in Table S5. The transgenic strain was

generated through φC31-mediated genomic integration into the *attP2* landing site on the 3rd chromosome of *Drosophila* (WellGenetics Inc., Taipei, Taiwan).

- UAS-Bero:FLAG

The Bero cDNA was amplified by PCR from clone FI02856 (DGRC Stock 1621396; https://dgrc.bio.indiana.edu//stock/1621396 ; RRID: DGRC_1621396), acquired from the *Drosophila* Genetics Resource Center (DGRC). To create FLAG-tagged Bero, the FLAG sequence was inserted downstream of the signal peptide sequence at position 26 of the Bero cDNA using overlap-PCR technique. Primers harboring the FLAG-tag sequence were utilized for amplification and cloning of the Bero cDNA into the pJFRC7-20XUAS-IVS-mCD8::GFP vector via NotI and XhaI restriction sites (refer to Supplementary Table S5 for primer sequences). The pJFRC7-20XUAS-IVS-mCD8::GFP vector was graciously provided by Gerald Rubin (Addgene plasmid #26220 ; http://n2t.net/addgene:26220 ; RRID:Addgene_26220). The transgenic strain was generated through φC31-mediated genomic integration into the *attP2* landing site (WellGenetics Inc.).

- *bero* knockout strains

CRISPR-mediated mutagenesis was conducted by WellGenetics Inc. employing modified protocols based on previous research (Kondo and Ueda, 2013). The process involved cloning the upstream gRNA sequence CAGACTGATCATAACGGCCA[CGG] and the downstream gRNA sequence CATCCTGCTCTTCTTCGGCG[TGG] separately into U6 promoter plasmids. A donor template for repair, consisting of a *3xP3-RFP* cassette with two *loxP* sites and two homology arms, was cloned into pUC57 Kan (refer to Table S5 for the primers utilized). The DNA plasmids containing the *CG9336/bero* targeting gRNAs and *hs-Cas9*, along with the donor

plasmid, were microinjected into embryos of the control strain w^{1118}. F1 flies carrying the *3xP3-RFP* selection marker were subsequently confirmed through genomic PCR and sequencing (refer to Table S5 for the primers used). This CRISPR procedure resulted in a 1629-bp deletion allele within the *CG9336/bero* gene, completely replacing its coding sequence with the *3xP3-RFP* cassette (Figure 10A). The *bero* knockout (KO) strain was then outcrossed with *Canton-S* wildtype strain for eleven generations to establish an isogenic line, employing *3xP3-RFP* as a selection marker.

4-3. Immunohistochemical staining and confocal microscopy

Wandering 3rd instar larvae were dissected in phosphate-buffered saline (PBS) and fixed with 4% formaldehyde in PBS for 20 minutes at room temperature. Following that, the larvae underwent a series of five washes using PBST (PBS supplemented with 0.3% Triton X-100) and were subsequently subjected to blocking with PBST containing 2% bovine serum albumin (BSA) that had been filtered through a 0.22 μm filter for a duration of 30 minutes at room temperature. Subsequently, the specimens were subjected to a 2-day incubation at 4°C in the presence of primary antibodies. Following the completion of five PBST washes, the samples were exposed to the appropriate secondary antibodies and incubated at room temperature for a duration of one hour. After undergoing further washes, the samples were mounted using ProLong Glass Antifade Mountant (Thermo Fisher, Carlsbad, CA, USA). Subsequently, imaging was carried out utilizing a Nikon C1Si confocal microscope, while Fiji (ImageJ, NIH, Bethesda, MD, USA) was employed for image processing.

The figure legends provide comprehensive information regarding the primary and secondary antibodies used in this study. Specific details regarding the concentration of each antibody can be found in the corresponding figure legends.

4-4. Verification of the functional efficacy of *bero RNAi*$^{shRNA\#2}$

A validation study was conducted to assess the level of Bero expression (Bero-YFP, anti-GFP) in ABLK neurons of both control and pan-neuronal *bero* RNAi larvae (*nSyb>bero RNAi* $^{shRNA\#2}$). The *bero*-expressing neurons were specifically labeled using *bero*-YFP (CPTI-001654) and subjected to immunohistochemistry using chicken anti-GFP (1:1000) and Alexa Fluor 488 anti-chicken secondary antibody (1:500). The immunohistochemistry procedure followed the above-mentioned protocol. Z-stack images were captured utilizing a Nikon C1Si confocal microscope, and subsequent image processing was carried out using Fiji software (ImageJ, NIH, Bethesda, MD, USA). The optical settings, including laser power and detector gain, remained consistent across all samples. For analysis purposes, the cell bodies of individual ABLK neurons were manually chosen as regions of interest (ROI) with consistent dimensions. The fluorescence intensity was normalized by calculating the ratio $F_{\text{Bero-YFP}}/F_{\text{background}}$, where $F_{\text{Bero-YFP}}$ represents the mean fluorescence intensity of the ROI, and $F_{\text{background}}$ represents the mean fluorescence intensity of the background region.

4-5. Genome-wide association analysis

The rolling behavior phenotypes of 38 representative DGRP lines were subjected to analysis using the DGRP2 web-based analysis tool (http://dgrp2.gnets.ncsu.edu; Huang et al., 2014; MacKay et al., 2012), employing four distinct statistical metrics. Initially, a linear mixed model was employed to adjust the rolling phenotypes for the impact of Wolbachia infection and five major chromosomal inversions (In(2L)t, In(2R)NS, In(3R)P, In(3R)K, and In(3R)Mo) (MacKay et al., 2012). Following that, association tests were performed on genetic variants with minor allele frequencies (MAF) equal to or greater than 0.05 using a linear mixed model implemented with the FaST-LMM algorithm (Lippert et al., 2011). Genetic variants that showed significant

associations (Table S1) were defined based on a *P*-value threshold of 1.0×10^{-5}, a commonly used nominal threshold in previous DGRP researches (Mackay and Huang, 2018). The resulting data were visualized using a custom MATLAB script (The MathWorks, Inc., Natick, MA, USA). Genes positioned within a 1 kb region upstream or downstream of the genetic variants showing significant associations were regarded as associated genes (Table S2).

4-6. Gene expression of *bero*

To assess the expression of the *bero* gene in the central nervous system (CNS) across different strains, expression analysis was conducted using pooled CNS samples from two wandering 3rd-instar larvae representing various strains. The selected strains for analysis encompassed the *Canton-S* strain as a control, the *bero* knockout (KO) strain derived from eleven generations of outcrossing with the *Canton-S* control, and four DGRP lines (RAL_208, RAL_315, RAL_391, RAL_705) exhibiting either remarkably strong or weak rolling behavioral responses. The total RNA present in the central nervous system (CNS) samples was isolated using Sepasol-RNA I (Nacalai tesque, Kyoto, Japan), and subsequent purification was carried out utilizing the RNeasy Mini Kit (QIAGEN N.V., Venlo, Netherlands). Following the RNA purification step, cDNA synthesis was performed using the ReverTra Ace™ qPCR RT Master Mix with gDNA Remover, according to the protocols provided by the manufacturer (Toyobo Co., Ltd., Osaka, Japan). RT-PCR carried out on a Mastercycler gradient thermocycler (Eppendorf, Hamburg, Germany) using KOD-Plus-Neo as the DNA polymerase (Toyobo). The expression levels of the target mRNA of *bero* were standardized relative to the expression levels of *αTub84B* mRNA in the corresponding samples. The specific primers used for this analysis can be found in Table S5.

4-7. Heat Probe Assay

The Heat Probe Assays were conducted in accordance with established protocols, with minor adjustments, as outlined in previous studies (Onodera et al., 2017; Tracey et al., 2003). The experimental animals, both male and female wandering 3rd-instar larvae, were reared under controlled conditions in a temperature-controlled environment at 25°C, adhering to a 12-hour light/dark cycle. They were provided with standard fly food as their nutrient source. The humidity was manually regulated within the range of 75-80%. Prior to the experiments, larvae of both genders were carefully collected from their respective vials. They were then subjected to two rinses with deionized water and subsequently transferred to a 140×100 mm Petri dish containing a fresh 2% agarose gel bed. The larvae were exposed to a lateral abdominal stimulation targeting segments A4-A6 using a noxious heat probe, specifically a modified soldering iron, adjusted to a temperature of 46°C, unless specified otherwise.

The behavioral responses of the larvae were recorded during the experiments and subsequently analyzed. The response latency, defined as the time interval between the initiation of the heat stimulation and the larvae's first complete 360° rotation, was measured. If the latency exceeded 10 seconds, it was recorded as 10.05 seconds. The sample sizes were determined by referring to previous studies conducted in the relevant field (Jovanic et al., 2016; Ohyama et al., 2015). To minimize potential variations, each control and experimental group underwent multiple testing sessions on different days, and the analysis of behavioral responses was conducted in a blinded manner. The data were further processed and visualized using a customized MATLAB script (The MathWorks, Inc.).

4-8. Free locomotion assay

For locomotion analysis, the animals were raised in a dark environment at a temperature of 25°C for four days on standard fly food, with manual control of humidity within the range of 75-80%. During the experiments, individual larvae in the wandering third-instar stage were carefully positioned at the center of a 100 x 100 mm matte-coated aluminum plate that was coated with a layer of 2% agarose gel bed. The locomotion of the larvae was recorded using a CMOS imager (EG130-B; Shodensha, Osaka, Japan) at a frame rate of 30 frames per second for a duration of 1 minute. Larvae that extended beyond the boundaries of the recording area were excluded from further analysis. The characteristics of larval locomotion were automatically tracked and quantified by analyzing the recorded videos using the FIMTrack software (https://github.com/kostasl/FIMTrack; Risse et al., 2017). The total number of frames exhibiting "left-bended" and "right-bended" labels in FIMTrack was used to determine the number of frames exhibiting head casting behavior. The total number of frames exhibiting "go" labels in FIMTrack was used to determine the number of frames exhibiting moving forward. The average velocity was calculated using a moving window of 15 frames.

4-9. Optogenetic behavioral assays

Animals used for optogenetic manipulation experiments were raised under specific conditions, including growth in the dark at 25°C for a duration of five days on fly food supplemented with 0.5 mM all-*trans* retinal (R2500; Sigma-Aldrich). The humidity was manually controlled within a range of 75-80%.

The optogenetic behavioral assay system employed a dark chamber equipped with a circuitry that controlled two arrays of LEDs strategically positioned to ensure uniform

illumination across the entire experimental arena. For experimental procedures, individual wandering 3rd-instar larvae were carefully positioned at center of a 100×100 mm copper plate with a matte coating. The plate was prepared by covering it with a thin layer of 10 mL deionized water, creating a water film that allowed the larvae to crawl or roll during the experiments. An illumination of 590 nm orange light with a duration of 30 seconds was delivered utilizing Amber LUXEON Rebel LEDs, with an intensity of 29.3 μW/mm² (Quadica Developments Inc., Alberta, Canada). The light intensity at the surface of the water was assessed using a HIOKI optical sensor (HIOKI E.E. CORPORATION, Nagano, Japan). Infrared LED lights were used to facilitate recording of larval behaviors in darkness (LDR2-90IR2-850; CCS Inc., Kyoto, Japan). The experimental setup utilized custom software programmed in LabVIEW (National Instruments, Austin, TX, USA) and a multifunction DAQ device (NI USB-6210; National Instruments) to control the LED light pulses and record behaviors of larvea with a GE60 CCD imager (Library Co., Ltd, Tokyo, Japan). The recorded videos were manually examined and subsequently analyzed using FIMTrack software.

The unique behavioral features of the larvae were tracked and generated through the analysis performed using FIMTrack. A decoding analysis was further conducted using a support vector machine (SVM)-based customized MATLAB script to determine the occurrence of rolling behavior in each frame of the video. Larval rolling behavior was defined as a complete 360° rotation along the body axis, while bending referred to C-shaped twitching without complete rolling. The data, both manually examined and automatically analyzed, were visualized using custom MATLAB scripts (The MathWorks, Inc.).

For experiments combining the Heat Probe Assay with the optogenetic manipulation, individual wandering 3rd-instar larvae were placed at center of a 140×100 mm Petri dish, as

described previously. Light illumination and heat stimulation were administered in close temporal proximity to each other. A 1-second pulse of 590-nm LED orange light (M590L3; ThorLabs, Newton, NJ, USA) with an intensity of around 30 μW/mm² or 565-nm LED lime light (M565L3; ThorLabs) with an intensity of around 80 μW/mm² was employed for optogenetic activation or inhibition, respectively, using a TTL-controlled LED driver (LEDD1B; Thorlabs). The initiation of the TTL pulse for the LED driver was synchronized with the heat stimulation using an Arduino® Nano Every microcontroller board (Arduino.cc, Lugano, Switzerland) with a custom program (Arduino IDE 2.0; Arduino). The heat stimulation was conducted in accordance with the above-mentioned protocol. The behavioral responses were recorded and subsequently analyzed offline following the previously described procedures.

4-10. Bioinformatic analysis of Bero protein

The amino terminal signal peptide of Bero was identified using SignalP-v5.0 (Almagro Armenteros et al., 2019; https://services.healthtech.dtu.dk/service.php?SignalP-5.0), while two potential glycosylation sites were identified using NetNGlyc-v1.0 (Gupta and Brunak, 2001; https://services.healthtech.dtu.dk/service.php?NetNGlyc-1.0). The putative transmembrane region was determined using TMHMM-v2.0 (Krogh et al., 2001; https://services.healthtech.dtu.dk/services/TMHMM-2.0/). The presence of a GPI-anchor site was predicted using the Big-PI Predictor (Eisenhaber et al., 1999; https://mendel.imp.ac.at/gpi/gpi_server.html). Furthermore, a three-dimensional model of the Bero protein, incorporating potential disulfide bridges, was constructed using the AlphaFold2 algorithm and visualized through PyMOL software (Jumper et al., 2021).

4-11. Calcium imaging of ABLK neurons

The animals employed for calcium imaging were raised on fly food supplemented with 0.5 mM all-*trans* retinal (R2500; Sigma-Aldrich). The dissection of wandering 3rd-instar larvae was carried out in a calcium-free external saline solution, following a modified protocol described in prior studies (Xiang et al., 2010). The composition of the solution consisted of 120 mM NaCl, 3 mM KCl, 4 mM $MgCl_2$, 10 mM NaHCO3, 5 mM TES, 10 mM HEPES, 10 mM Glucose, 10 mM Sucrose, 10 mM Trehalose, and 1 mM sodium L-Glutamate, with adjustments made to achieve an osmolality of 305 mOsm/kg and a pH of 7.25 using NaOH. Before the imaging, the buffer was replaced with oxygenated external saline solution, supplemented with 1.5 mM $CaCl_2$.

For optogenetic activation of nociceptors, a 470-nm LED blue light (M470L5; ThorLabs) was applied 250 seconds after the start of imaging. The light emission was facilitated through the utilization of a TTL-controlled LED driver (LEDD1B; Thorlabs), with precise control over the timing of the TTL pulse achieved by an Arduino® Uno R3 microcontroller board (Arduino.cc) with a custom-written program using Arduino IDE 1.0 (Arduino.cc). The application of blue light was conducted at an intensity of 0.37 mW/mm^2, spanning a duration of 2.5 seconds. The excitation of jRCaMP1b was accomplished using a 561-nm diode laser (Sapphire 561 LP; Coherent) at an intensity of 0.45 mW. The cell bodies of ABLK neurons were subjected to imaging at a frequency of one frame per second. The images were obtained at a resolution of 512x512 pixels, with an exposure time of 250 ms. The fluorescence emission was recorded using an inverted microscope (IX-71; Olympus, Tokyo, Japan) equipped with 610/60 nm bandpass filters (Chroma Technology Corp., Bellows Falls, VT, USA), an EMCCD camera (iXon X3; Andor Technology Ltd., Belfast, UK) and a 20X objective lens (UCPlanFLN 20x/0.45; Olympus). The data analysis was performed using a custom MATLAB script (The MathWorks,

Inc.). The region of interest (ROI), representing the cell body of each ABLK neuron, was manually identified and selected from the confocal time series dataset.

For the analysis of sustained activities, the fluorescence change was calculated using the following formula:

$$\frac{\Delta F^{\text{Persistent}}}{F_0} = \frac{F(t) - \big(B(t) - B_0(t)\big) - F_0(t)}{F_0(t)} \times 100$$

The variables $B(t)$ and $F(t)$ represent the fluorescence intensity of the background region and the ROI at a specific time point t, respectively. The variables $B_0(t)$ and $F_0(t)$ represent the median of the five lowest fluorescence intensity values of the background region and the ROI respectively, within the time interval from t = -10 s to t = 10 s. The cumulative sum of $\Delta F^{\text{Persistent}}/F_0(t)$ values was used to calculate the area under the curve (AUC).

For the analysis of evoked nociceptive responses, the fluorescence change was determined using the formula:

$$\frac{\Delta F}{F_0} = \frac{F(t) - (B(t) - B_0) - F_0}{F_0} \times 100$$

The variables $B(t)$ and $F(t)$ represent the fluorescence intensity of the background region and the ROI at a specific time point t, respectively. The variables B_0 and F_0 represent the median of the five lowest fluorescence intensity values of the background region and the ROI, respectively, within a 50-second period immediately preceding the onset of blue light illumination. F_0 was considered as the baseline fluorescence. The highest value of $\Delta F/F_0(t)$ within the time interval from t = 0 s to t = 5 s was identified as the $\Delta F_{max}/F_0$.

4-12. Statistics

Sample sizes in this study were comparable to those reported in previous studies. When comparing two groups, an unpaired Welch's t-test or a nonparametric Wilcoxon rank sum test was employed, as indicated in the figure legends. To conduct multiple comparisons, a Kruskal-Wallis test followed by Dunn's multiple comparison test was employed. To assess differences in optogenetic activation-induced behaviors, a Chi-squared test was applied. Statistical significance was determined for *P*-values less than 0.05 (*$P < 0.05$, **$P < 0.01$, ***$P < 0.001$, ****$P < 0.0001$). Statistical analyses were conducted using R (version 3.6.1, R Development Core Team) or MATLAB (The MathWorks, Inc.). Detailed information regarding the specific statistical tests conducted and the corresponding *P*-values for all quantitative data comparisons can be located within the respective figure legends.

Acknowledgements

I would like to express my deep appreciation to my esteemed supervisors, Prof. Tadashi Uemura and Dr. Tadao Usui, for their unwavering support and guidance throughout my Ph.D. studies and related research. Their invaluable expertise, patience, and motivation have been instrumental in shaping my academic journey and the completion of this thesis. I am particularly grateful to Dr. Tadao Usui for generating essential reagents and creating innovative homemade devices for my research.

I extend my heartfelt gratitude to Yuma Tsukasa, Misato Kurio, Akimitsu Tsumadori, and Shumpei Baba for their dedicated efforts in optimizing and conducting calcium imaging of ABLK neurons. I am also thankful to Kaho Maeta for her contributions to the free locomotion assay and to Akira Murakami for developing the SVM-based customized MATLAB classifier. Furthermore, I would like to express my appreciation for the preceding research carried out by Risa Nishimura and Koun Onodera, upon which this thesis is founded and expanded. I would like to express my gratitude to the fellow members of Uemura's lab for their stimulating discussions and valuable advice. Special thanks go to Mayumi Futamata, Kanae Oki, and Hiroko Imai for their exceptional technical support. I am also grateful to Prof. James Hejna for providing insightful feedback on the manuscript.

I am grateful to the Bloomington *Drosophila* Stock Center (BDSC), *Drosophila* Stocks of Ehime University, Kyoto *Drosophila* Stock Center, J. Simpson, T. Sakai, A. Claridge-Chang, and K. Emoto for generously providing the fly stocks and other necessary reagents. I gratefully acknowledge the financial support I received from the Top Global University Project, the Japanese Government Scholarships (MEXT).

Lastly, I would like to express my deepest appreciation to my parents for their unwavering spiritual support not only throughout the process of writing this thesis but also in every aspect of my life. Thank you!

This thesis is based on material contained in the following scholarly paper.

Kai Li, Yuma Tsukasa, Misato Kurio, Kaho Maeta, Akimitsu Tsumadori, Shumpei Baba, Risa Nishimura, Akira Murakami, Koun Onodera, Takako Morimoto, Tadashi Uemura, and Tadao Usui

"Belly roll, a GPI- anchored Ly6 protein, regulates *Drosophila melanogaster* escape behaviors by modulating the excitability of nociceptive peptidergic interneurons"

eLife, Jun 13, 2023

https://doi.org/10.7554/eLife.83856

https://elifesciences.org/articles/83856#content

Figures

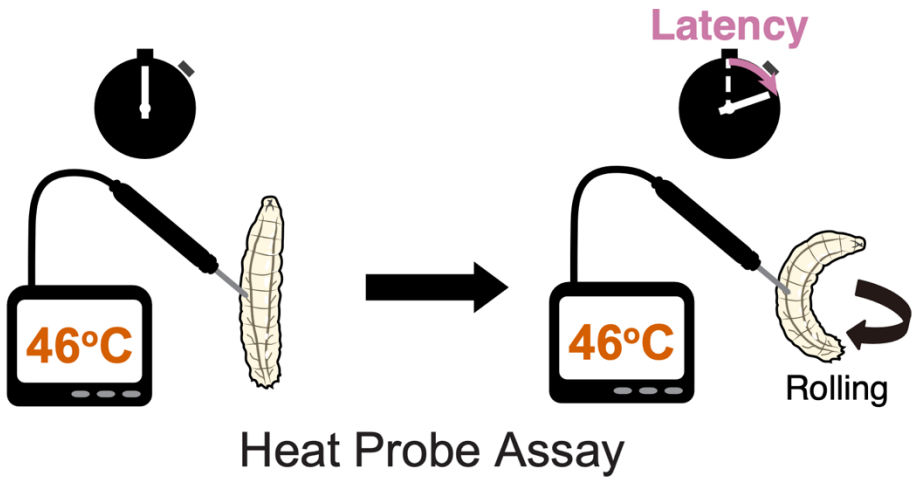

Figure 1. A diagram illustrating the Heat Probe Assay

Larvae of both genders were collected from vials and prepared for the experiments by rinsing them with deionized water. They were then transferred to a Petri dish with agarose gel and exposed to a noxious heat probe targeting specific abdominal segments. The heat probe, a modified soldering iron, was set to a temperature of 46°C, unless stated otherwise. The response latency was determined as the time from the start of heat stimulation to the larvae's first full 360° rotation. Latencies exceeding 10 seconds were recorded as 10.05 seconds.

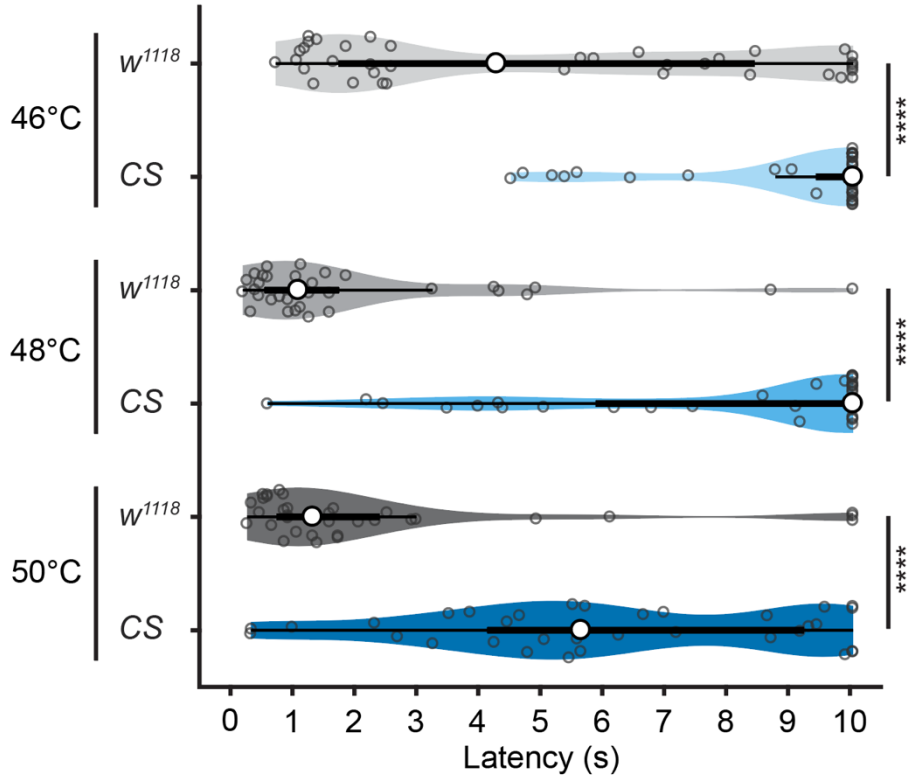

Figure 2. Rolling latency differs between w^{1118} and *Canton-S* (CS) wild-type strains

The rolling latency, which measures the time delay for nociceptive escape behavior, exhibits significant differences between two strains, w^{1118} and *Canton-S* (CS), with heat stimulation at different temperatures.

- With 46°C stimulation, [w^{1118}] n = 40, [*CS*] n = 38, P <0.0001, Wilcoxon rank sum test.
- With 48°C stimulation, [w^{1118}] n = 32, [*CS*] n = 33, P <0.0001, Wilcoxon rank sum test.
- With 50°C stimulation, [w^{1118}] n = 33, [*CS*] n = 33, P <0.0001, Wilcoxon rank sum test.

Violin plots in this and subsequent figures depict the kernel density estimation of the data. The median is represented by the central circle, while the boxplot shape illustrates the 25th and 75th percentiles. Whiskers extending from the box indicate the 90th and 10th percentiles. Each data point corresponds to an individual sample. The HPA experiment was performed by Risa Nishimura.

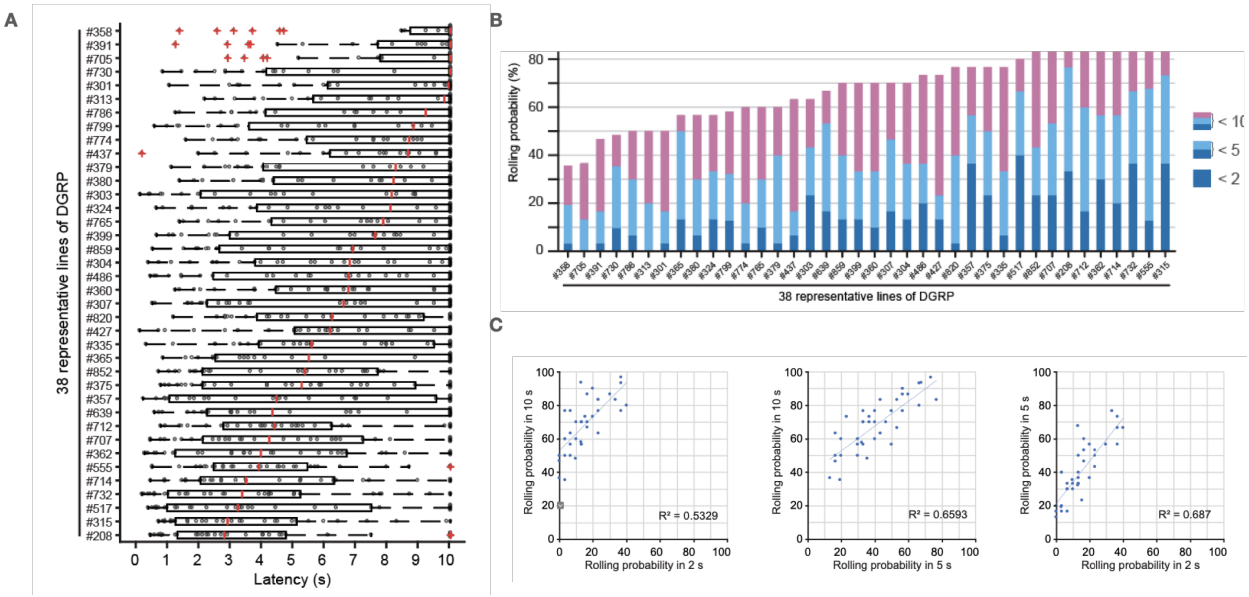

Figure 3. Rolling behavior in 38 representative inbred wild-type strains of DGRP

(A) The rolling latency of 38 representative inbred wild-type strains is presented in ascending order. The boxplots in this and subsequent figures represent the median, 25th and 75th percentiles, while the whiskers extend to the 90th and 10th percentiles. Each strain consists of 30 or 31 larvae. The HPA experiment was performed by Risa Nishimura.

(B) The ascending order of rolling probability for the strains in the same experiment is depicted in the figure. The stacked bar chart illustrates the probability of rolling within 2, 5, and 10 seconds, respectively.

(C) The three plots present a correlation analysis depicting the relationship between rolling probability in three response classes (rolling probability in 2 seconds, 5 seconds, and 10 seconds) of 38 representative DGRP lines. The corresponding squared Pearson's correlation coefficient (R^2) is 0.5329 (2 sec vs 10 sec), 0.6593 (5 sec vs 10 sec), 0.687 (2 sec vs 5 sec), revealing a strong association among the three response classes.

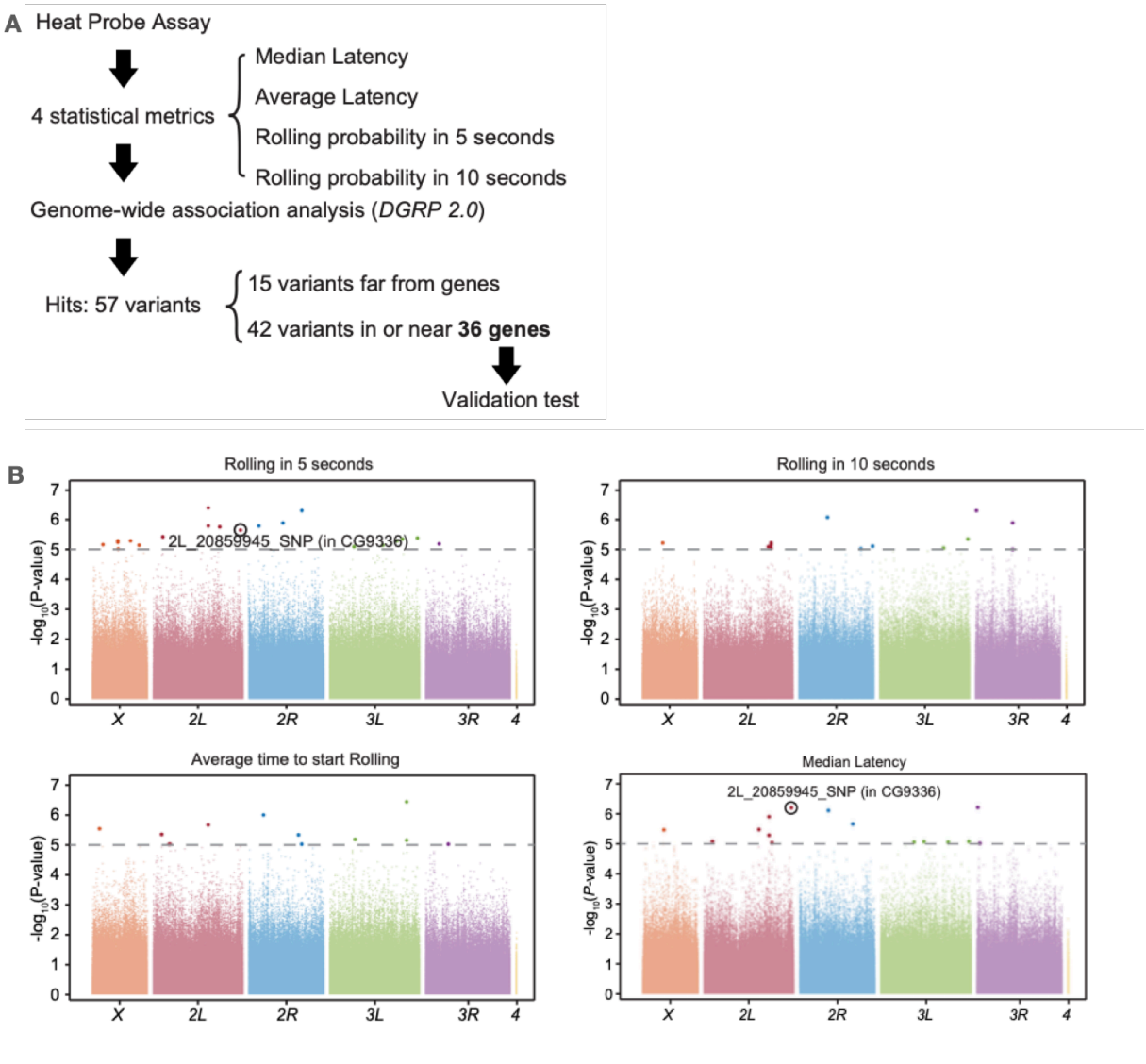

Figure 4. GWAS results

(A) A schematic illustrating the experimental procedures employed for the Genome-Wide Association (GWA) analysis.

(B) The Manhattan plots depicts the Genome-Wide Association analysis conducted for the the rolling escape behavior with 4 distinct statistical metrics. Each colored point corresponds to a specific genetic variant, including single nucleotide polymorphisms, deletions, or insertions. The arrangement of data points reflects their relative chromosome position, with different colors indicating the respective chromosomes. The *P*-values are represented on the y-axis after being transformed into -$\log_{10}$ scale. The grey dotted line indicates the nominal *P*-value threshold of 1.0×10^{-5}. The points above the grey dotted line are the hits. The SNP associated with *bero*, 2L_20859945_SNP, is labeled in the plots.

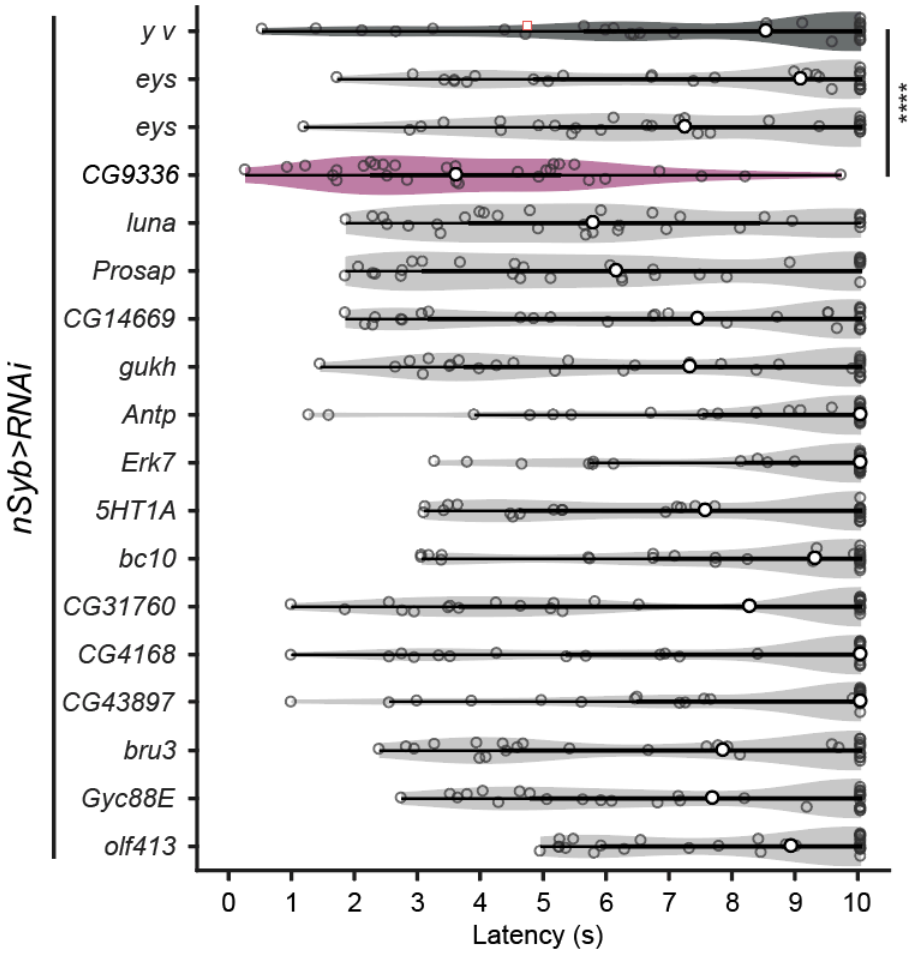

Figure 5. A secondary screen performed using the HPA with pan-neuronal RNAi knockdown of 16 candidate genes

The rolling latency of each knockdown candidate group was presented, with each group consisting of 30 or 31 larvae. The detailed genotypes are as follows:

- *nSyb > yv*: *y[1] w[1118]/y[1] v[1]; +/+; nSyb-GAL4/+*
- *nSyb > Candidate RNAi*: *y[1] w[1118]/y[1] v[1]; +/+; nSyb-GAL4/UAS-Candidate RNAi*

The *P*-values, indicating the significance between the control group and each experimental group, are as follows: 0.95146, 0.81246, <0.0001, 0.06555, 0.14600, 0.62217, 0.54814, 0.15318, 0.05314, 0.79911, 0.43823, 0.89514, 0.40105, 0.19534, 0.76084, 0.92053, 0.40055 respectively. Wilcoxon rank sum test. The HPA experiment was performed by Risa Nishimura and Koun Onodera.

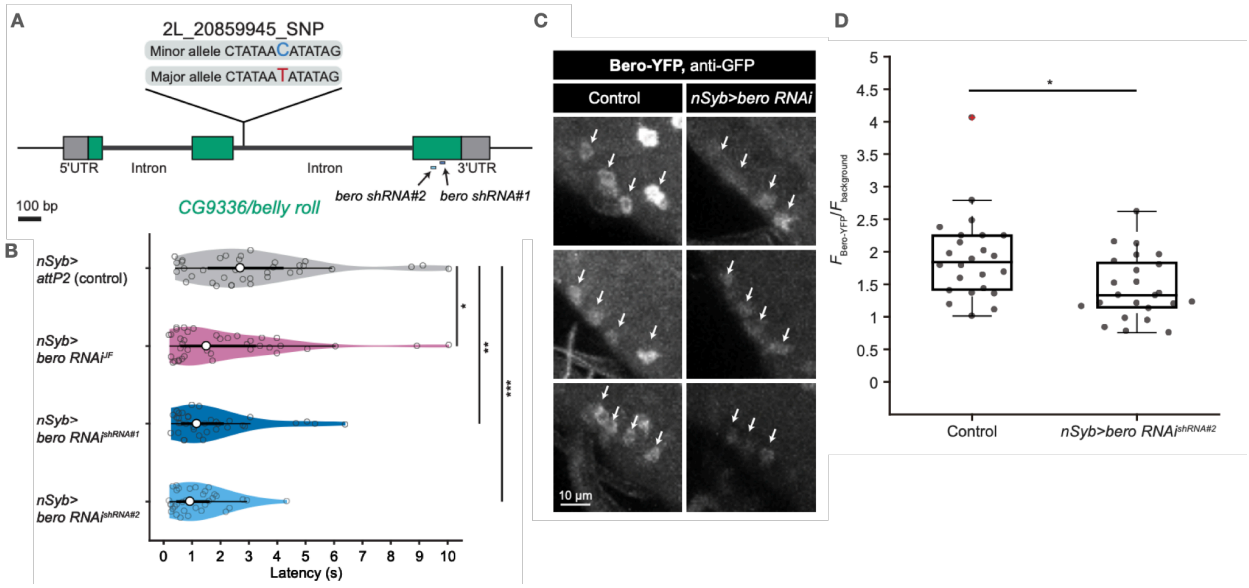

Figure 6. Production and validation of shRNAs targeting *CG9336*

(A) A diagram illustrating the target region of two distinct shRNAs. The depicted green region corresponds to the coding sequence (CDS) of the *bero* gene. It also illustrates the *bero*-associated single nucleotide polymorphism (SNP) located at position 2L_20859945 (minor allele: Cytosine; major allele: Thymine). The construction of shRNA lines was undertaken by Tadao Usui.

(B) The rolling latency of *nSyb>attP2* control was compared to that of pan-neuronal *bero* knockdown animals. The genotypes and sample numbers for each group were as follows:

- *nSyb>attP2* (control, n = 36): *y[1] w[1118]/y[1] v[1]; +/+; nSyb-GAL4/attP2*
- *Syb>bero RNAi*^{JF} (n = 40): *y[1] w[1118]/y[1] v[1]; +/+; nSyb-GAL4/UAS-bero[JF03422]*
- *nSyb>bero RNAi*$^{shRNA\#1}$ (n = 36): *y[1] w[1118]/y[1] v[1]; +/+; nSyb-GAL4/UAS-bero[shRNA#1]*
- *nSyb>bero RNAi*$^{shRNA\#2}$ (n = 35): *y[1] w[1118]/y[1] v[1]; +/+; nSyb-GAL4/UAS-bero[shRNA#2]*

The corresponding *P*-values were determined as 0.02331, 0.00206, and 0.00001. Wilcoxon rank sum test. The HPA experiment was performed by Koun Onodera.

(C) Confocal images representing the expression level of Bero (Bero-YFP, detected using anti-GFP antibodies) in ABLK neurons of control and pan-neuronal bero knockdown larvae (*nSyb>bero RNAi*$^{shRNA\#2}$) are displayed. Arrows mark the location of ABLK neurons. The optical settings and analysis procedure were identical for both groups. Scale bar measuring 10 µm is included in the image. The experiment was performed by Tadao Usui.

(D) A quantitative analysis was conducted to compare the expression level of Bero (normalized fluorescence intensities; refer to the methods section for specific details) in ABLK neurons of control larvae (n = 24 neurons from 3 animals) and pan-neuronal *bero* knockdown larvae (*nSyb>bero RNAi*$^{shRNA\#2}$, n = 24 neurons from 3 animals). Statistical significance was assessed using an unpaired Welch's t-test, with significance *P*-value of 0.01371.

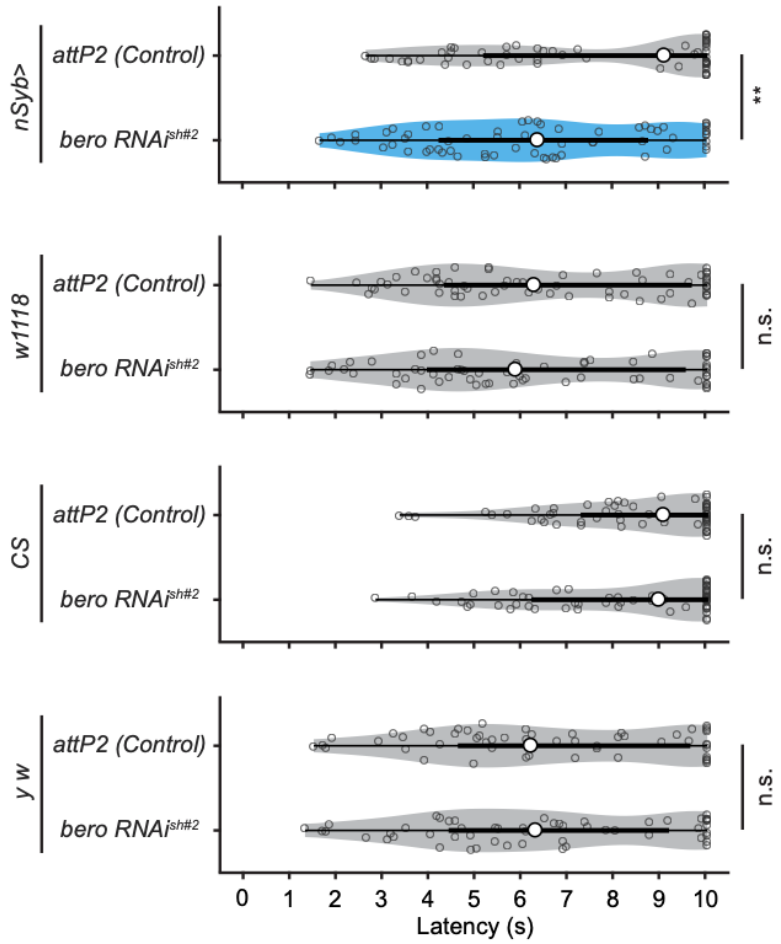

Figure 7. Reduction of rolling latency upon the *bero* knockdown

The rolling latency of *nSyb>attP2* control was compared to that of pan-neuronal *bero* knockdown animals. Three sets of effector-controls in different background are also presented. The genotypes and sample numbers for each group were as follows:

- *nSyb>attP2* (control, n = 63): *y[1] w[1118]/y[1] v[1]; +/+; nSyb-GAL4/attP2*
- *nSyb>bero RNAi$^{shRNA\#2}$* (n = 65): *y[1] w[1118]/y[1] v[1]; +/+; nSyb-GAL4/UAS-bero[shRNA#2]*
- *w^{1118}, attP2* (n = 64): *w[1118]/y[1] v[1]; +/+; attP2/+*
- *w111,8 bero RNAi$^{shRNA\#2}$* (n = 60): *w[1118]/y[1] v[1]; +/+; UAS-bero[shRNA#2]/+*
- *Canton-S, attP2* (n = 60): *y[1] v[1]/+; +/+; attP2/+ (Canton-S background*
- *Canton-S, bero RNAi$^{shRNA\#2}$* (n = 60): *y[1] v[1]/+; +/+; UAS-bero[shRNA#2]/+ (Canton-S background)*
- *y w, attP2* (n = 55): *y[1] w[1118]/y[1] v[1]; +/+; attP2/+*
- *y w, bero RNAi$^{shRNA\#2}$* (n = 55): *y[1] w[1118]/y[1] v[1]; +/+; UAS-bero[shRNA#2]/+*

The *P*-values obtained from the statistical analysis using the Wilcoxon rank sum test were as follows: 0.00768, 0.49399, 0.55580, and 0.66802.

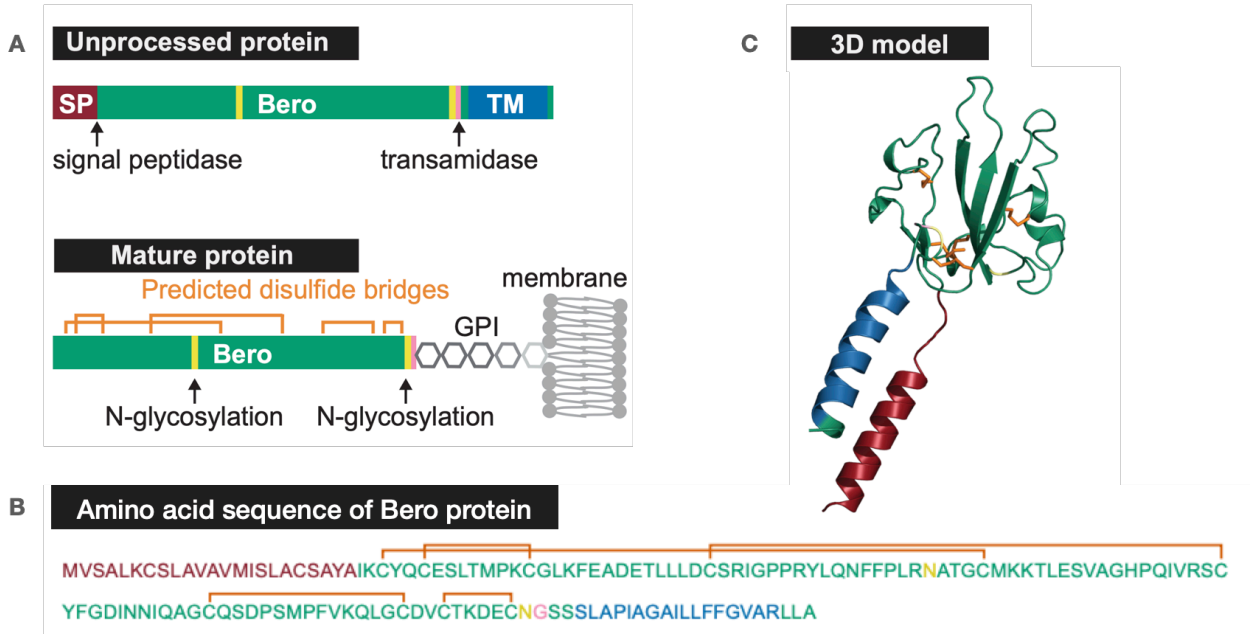

Figure 8. Bioinformatic structure prediction of Bero

(A) A diagram illustrating the structure of unprocessed and mature Bero protein is presented. The signal peptide (SP) and transmembrane region (TM) are indicated. The predicted disulfide bonds are depicted by orange lines, while the predicted N-glycosylation sites are indicated by yellow lines. The predicted GPI-modification site is marked by pink lines.
(B) A diagram illustrating annotated amino acid sequences of unprocessed Bero protein. The text colors indicate the predicted signal peptide (red), the predicted transmembrane region (blue), the predicted N-glycosylation sites (yellow), and the predicted GPI-modification site (pink). The orange brackets mark the predicted disulfide bonds.
(C) A diagram illustrating the three-dimensional protein structure prediction of unprocessed Bero protein generated using AlphaFold2. The predicted structure is represented with different color-coded regions: the red region represents the signal peptide, the blue region corresponds to the transmembrane region, the yellow region represents the predicted N-glycosylation sites, and the pink region indicates the predicted GPI-modification site. The orange sticks indicate the predicted disulfide bonds.

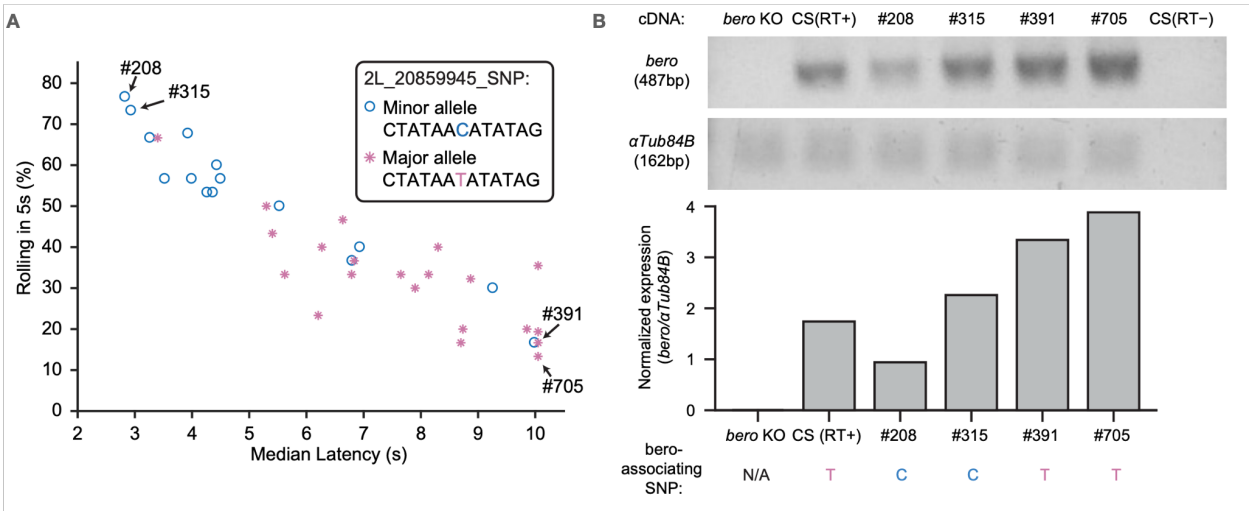

Figure 9. Larvae with the minor allele (C) exhibited increased sensitivity and reduced expression levels of *bero*

(A) A scatter plot illustrates the responsiveness of DGRP core 38 lines in the Heat Probe Assay, with the *bero* minor allele represented by blue circles and the major allele represented by red asterisks. The majority of lines carrying the *bero* minor allele exhibited higher responsiveness compared to those with the major allele. Four lines with extremely high (DGRP_391, DGRP_705) or low (DGRP_208, DGRP_315) rolling latency are labeled by arrows.

(B) A histogram illustrates the *bero* gene expression in the larval central nervous system (CNS) of *Canton-S* control, *bero* homozygous ($bero^{KO}/bero^{KO}$) mutant, and four DGRP lines with distinct rolling latency phenotypes (DGRP_391, DGRP_705 with high latency; DGRP_208, DGRP_315 with low latency). The expression levels of *bero* were normalized to *αTub84B* expression. The top panel displays a photograph of the DNA agarose gel, while the bottom panel indicates the nucleotide variations of the *bero*-associated SNP (2L_20859945_SNP) in each line (n = 1). The experiment was performed by Tadao Usui.

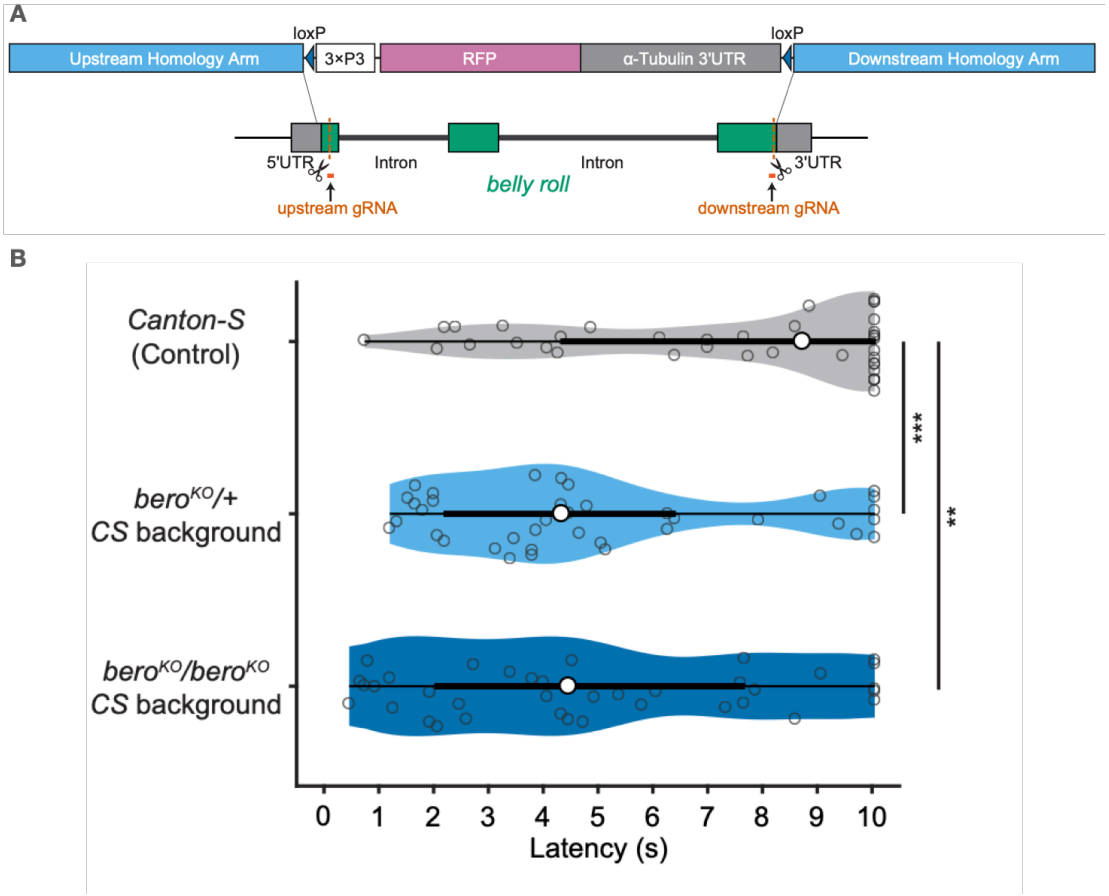

Figure 10. Implications of *bero* Knockout on nociceptive escape behavior

(A) A diagram illustrating the CRISPR/Cas9-mediated knockout of the *bero* gene through homology-dependent repair (HDR). The depicted green region corresponds to the coding sequence (CDS) of the *bero* gene. The blue region depicted in the figure represents the homology arms, while the orange region represents the CRISPR guide RNA used for targeting the specific gene sequence. This technique results in a 1629-bp deletion within the bero gene, which is then replaced by a 3xP3-RFP cassette. Please refer to the Methods section for a more detailed description of the procedure.
(B) The rolling latency was measured in three groups: *Canton*-S control, *bero* heterozygous mutant larvae, and homozygous mutant larvae. It is important to note that the *bero* KO strain had undergone eleven generations of outcrossing to *Canton*-S.
The genotypes and sample numbers for each group were as follows:

- *Canton-S* (control, n = 38): *Canton-S*
- *bero* heterozygous (n = 38): *bero[KO]/+* (Canton-S background)
- *bero* homozygous (n = 37): *bero[KO]/bero[KO]* (Canton-S background)

The obtained *P*-values from statistical analysis were as follows: 0.00096 and 0.00102, determined using the Wilcoxon rank sum test.

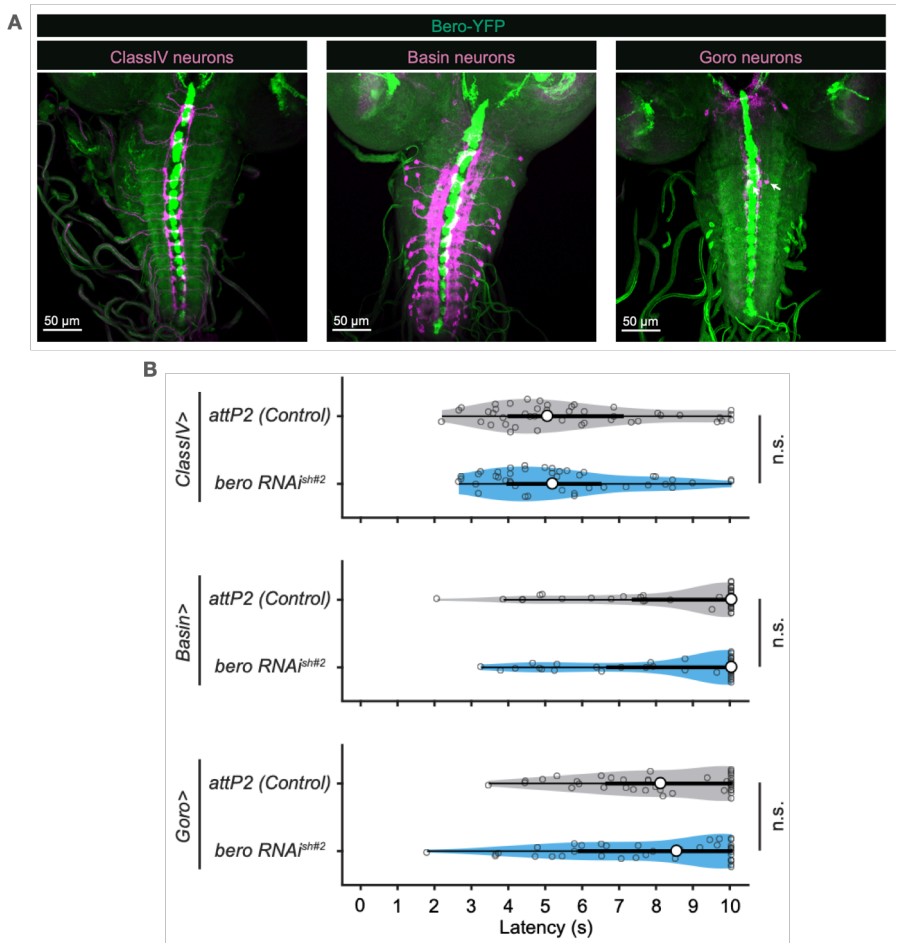

Figure 11. *bero* knockdown in nociceptive neurons did not affect escape behavior

(A) A maximum projection of confocal image stacks is presented, demonstrating the co-localization of endogenous Bero reporter, Bero-YFP (depicted in green), with nociceptive neurons (ClassIV neurons marked by *ppk>CD4-tdTomato*, basin neurons marked by *R72F11>CD4-tdTomato*, and goro neurons marked by *R69F06>CD4-tdTomato*; depicted in magenta) in VNC region of third instar larvae. The scale bars represent 50 µm.
(B) The rolling latency of *attP2* control was compared to that of corresponding *bero* knockdown animals. The genotypes and sample numbers for each group were as follows:

- *ClassIV>attP2* (control, n = 44): *w[*]/y[1] v[1]; +/+; ppk-GAL4/attP2*
- *ClassIV>bero RNAi$^{shRNA\#2}$* (n = 43): *w[*]/y[1] v[1]; +/+; ppk-GAL4/UAS-bero[shRNA#2]*
- *Basin>attP2* (control, n = 40): *w[1118]/y[1] v[1]; +/+; Basin-GAL4(R72F11)/attP2*
- *Basin>bero RNAi$^{shRNA\#2}$* (n = 39): *w[1118]/y[1] v[1]; +/+; Basin-GAL4(R72F11)/UAS-bero[shRNA#2]*
- *Goro>attP2* (control, n = 39): *w[1118]/y[1] v[1]; +/+; Goro-GAL4(R69F06)/attP2*
- *Goro>bero RNAi$^{shRNA\#2}$* (n = 40): *w[1118]/y[1] v[1]; +/+; Goro-GAL4(R69F06)/UAS-bero[shRNA#2]*

The *P*-values obtained from the statistical analysis using the Wilcoxon rank sum test were as follows: 0.54941, 0.90921, and 0.71051.

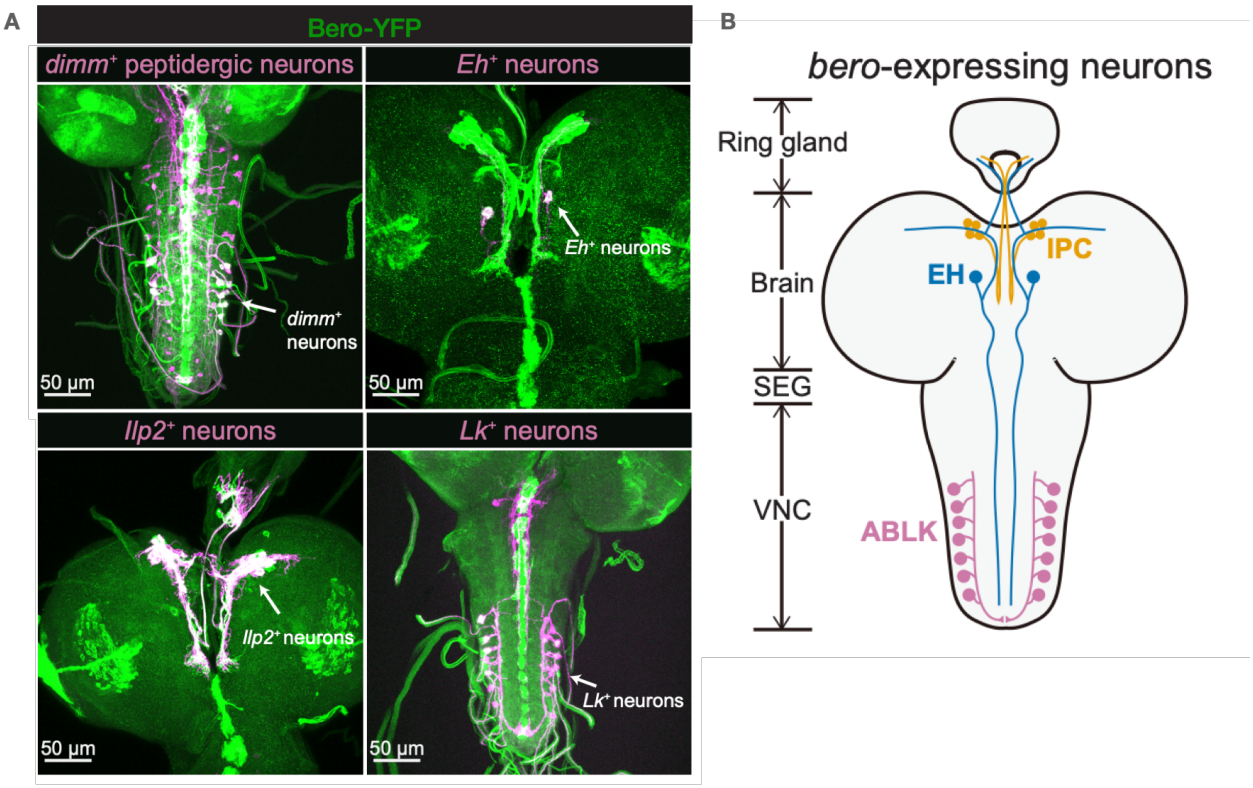

Figure 12. *bero*-expressing neurons

(A) A maximum projection of confocal image stacks is presented, demonstrating the co-localization of endogenous Bero reporter, Bero-YFP (depicted in green), with peptidergic neurons marked by *UAS-CD4-tdTomato* (depicted in magenta) in VNC region of third instar larvae. The neurons are indicated by arrows. The scale bars represent 50 µm. The experiment was performed by Tadao Usui.
(B) A diagram illustrating the distribution of bero-expressing neurons in the nervous system. The identified neuronal populations include IPC (insulin-producing cells, depicted in yellow), EH (Eclosion hormone-producing neurons, depicted in blue), ABLK (abdominal Leucokinin-producing neurons, depicted in magenta).

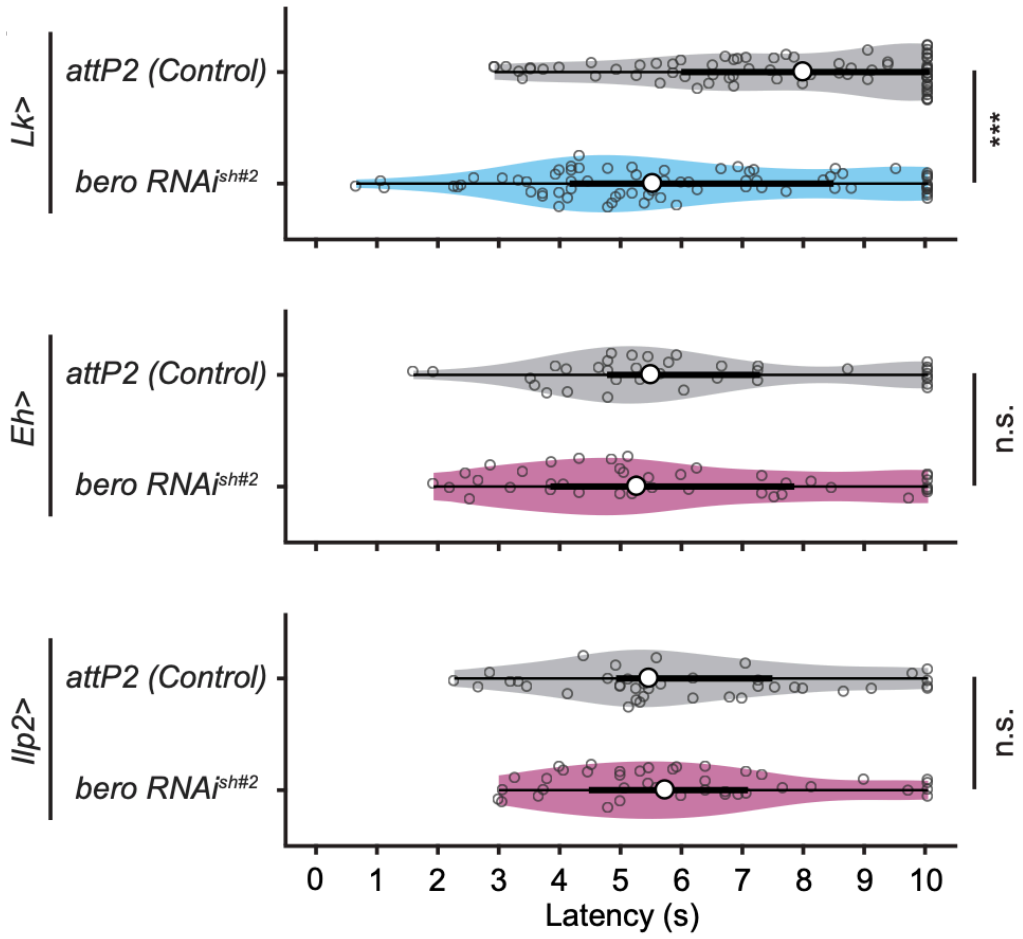

Figure 13. *bero* knockdown in LK neurons promoted escape behavior

The rolling latency of *attP2* control was compared to that of animals with *bero* knockdown in corresponding *bero*-expressing neuron. The genotypes and sample numbers for each group were as follows:

- *Lk>attP2* (control, n = 75): *w[1118]/y[1] v[1]; Lk-GAL4/+; attP2/+*
- *Lk>bero RNAi*$^{shRNA\#2}$ (n = 73): *w[1118]/y[1] v[1]; Lk-GAL4/+; UAS-bero[shRNA#2]/+*
- *Eh>attP2* (control, n = 41): *w[*]/y[1] v[1]; Eh.2.4-GAL4/+; attP2/+*
- *Eh>bero RNAi*$^{shRNA\#2}$ (n = 38): *w[*]/y[1] v[1]; Eh.2.4-GAL4/+; UAS-bero[shRNA#2]/+*
- *Ilp2>attP2* (control, n = 39): *w[*]/y[1] v[1]; Ilp2-GAL4.R/+; attP2/+*
- *Ilp2>bero RNAi*$^{shRNA\#2}$ (n = 40): w[*]/y[1] v[1]; Ilp2-GAL4.R/+; UAS-bero[shRNA#2]/+

The *P*-values obtained from the statistical analysis using the Wilcoxon rank sum test were as follows: 0.00020, 0.63999, and 0.84057.

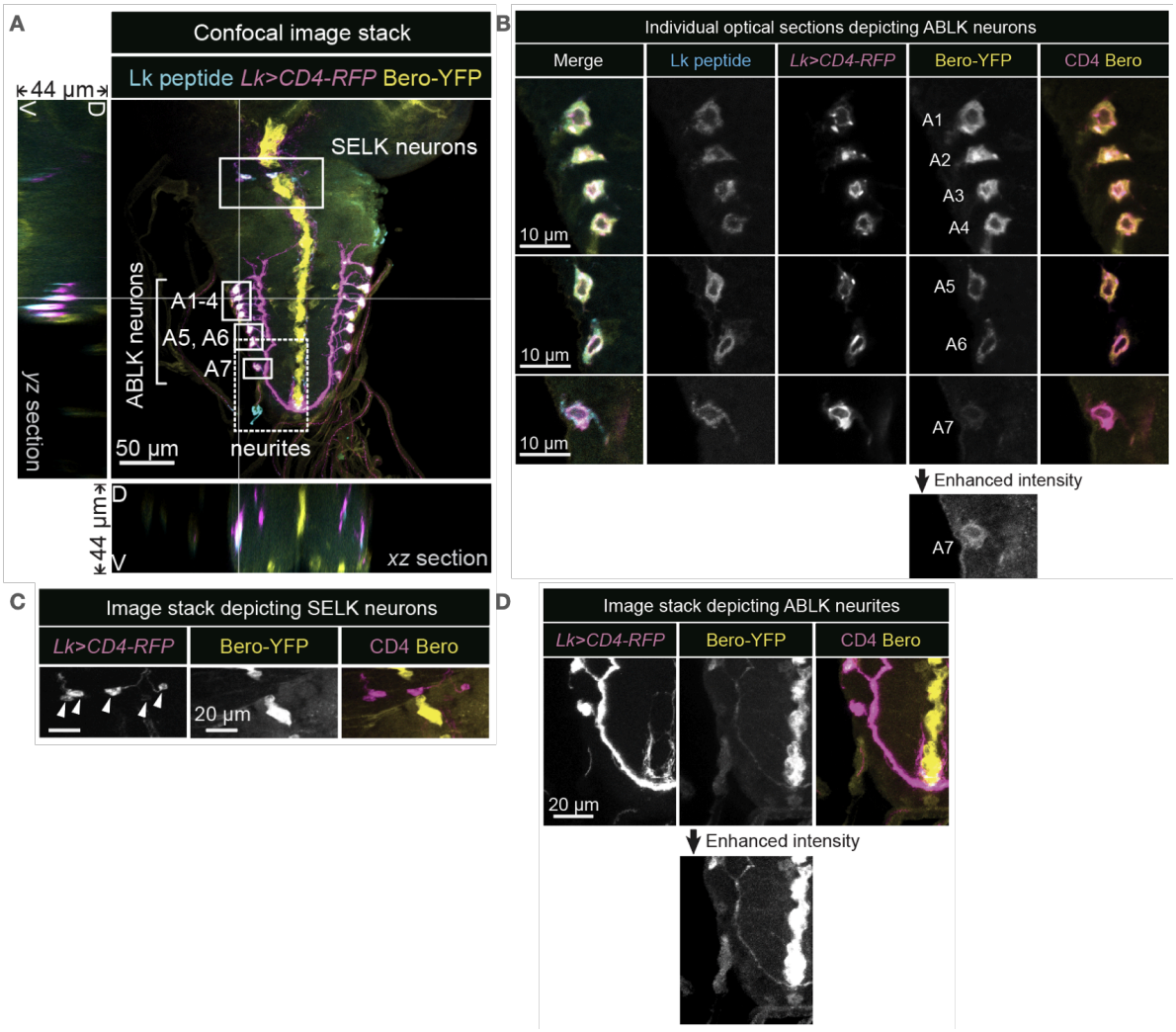

Figure 14. Expression of *bero* specifically in ABLK neurons and their neurites

(A) A maximum projection of confocal image stacks is presented, displaying the endogenous expression of Bero (visualized by Bero-YFP in yellow), LK neurons (labeled with *Lk-GAL4.TH, UAS-CD4-tdTomato* in magenta), and Leucokinin (detected by anti-Lk staining in cyan) in a 3rd instar larva. The bottom and left panels depict cross-sections (XZ and YZ, respectively) of the ABLK somatic region, indicated by horizontal and vertical gray lines in the primary image. The magnified views of the boxed regions are displayed in (B), (C), and (D). The scale bars represent 50 µm.

(B) Individual optical sections of magnified views from the boxed regions are presented, specifically highlighting ABLK neurons. The ABLK neurons are labeled as A1-A7, with a particularly enhanced intensity image of the A7 neuron showcased. Additionally, single channel and dual channel images demonstrating the co-localization of Bero and ABLK neurons are included. The scale bars represent 10 µm.

(C) Image stacks of distinct channel are displayed, specifically highlighting SELK neurons labeled by arrowheads. The scale bars represent 20 µm.

(D) Image stacks are presented, emphasizing ABLK neurites. An image with enhanced intensity is shown to enhance visibility and detail. The scale bars represent 20 µm.

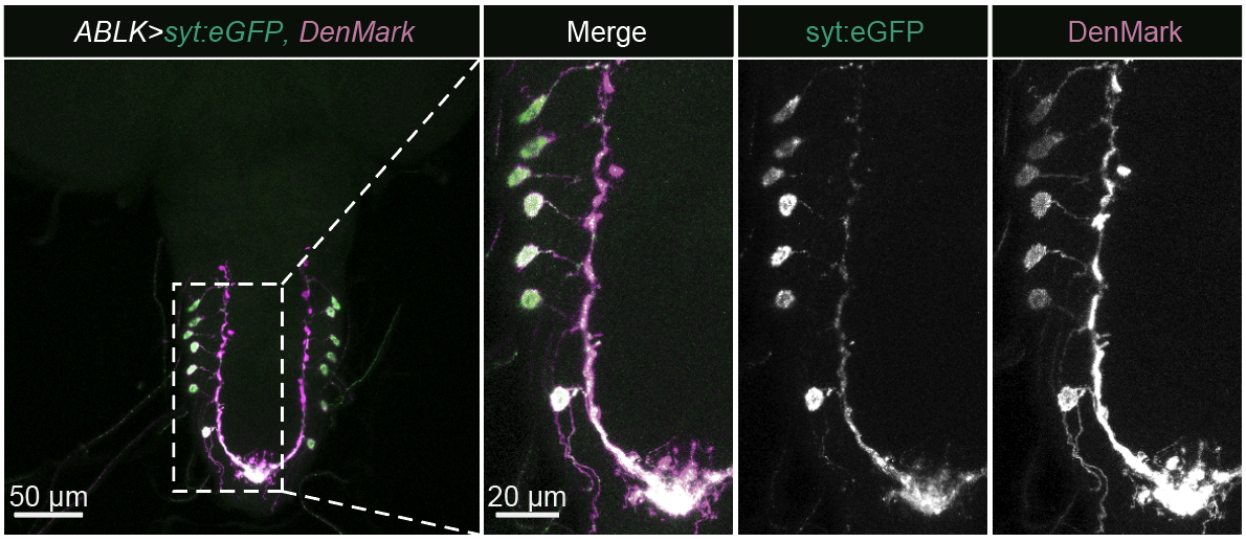

Figure 15. Distribution of Bero in both dendritic and axonal regions of ABLK

A maximum projection of confocal image stacks is presented, illustrating the labeling of dendrites (marked by *ABLK>DenMark* in magenta) and axon terminals (marked by *ABLK>syt:eGFP* in green) in ABLK neurons of a 3rd instar larva. The right panels display the magnified views of the boxed regions, including the single channel images. Scale bars measuring 50 µm and 20 µm are provided for the primary image and magnified view, respectively. The experiment was performed by Tadao Usui.

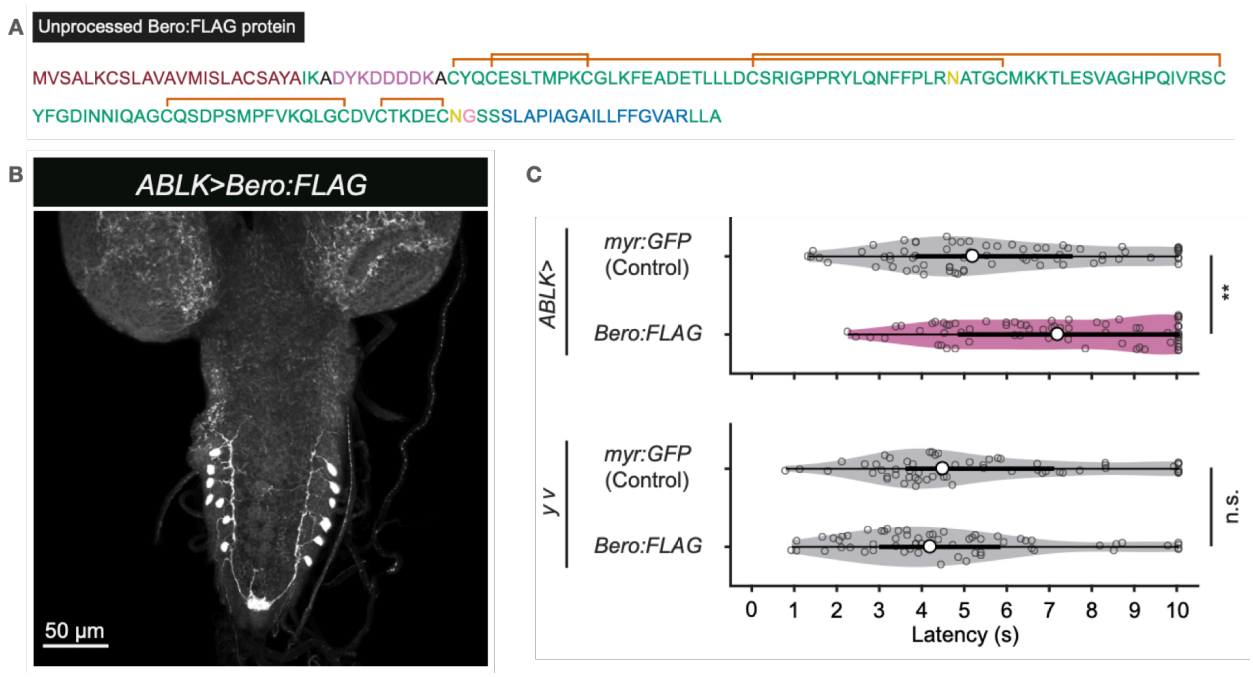

Figure 16. Overexpression of *bero* in ABLK neurons suppressed escape behavior

(A) A diagram illustrating annotated amino acid sequences of unprocessed Bero:FLAG protein. The text colors indicate the predicted signal peptide (red), the predicted transmembrane region (blue), the predicted N-glycosylation sites (yellow), the predicted GPI-modification site (pink), and the FLAG-tag sequence (purple). The orange brackets mark the predicted disulfide bonds.

(B) A maximum projection of confocal image stacks is presented, exhibiting the specific overexpression of Bero:FLAG (detected by anti-FLAG staining) in ABLK neurons of third instar larvae. The scale bars represent 50 µm.

(C) The rolling latency of *ABLK>myr:GFP* control was compared to that of ABLK-specific *bero* overexpression animals. A set of effector-control is also presented. The genotypes and sample numbers for each group were as follows:

- *ABLK>myr:GFP* (control, *n* = 63): *w[*]/y[1] v[1]; Lk-GAL4, tsh-LexA/tubP-FRT-GAL80-FRT; LexAop-FLP.L/UAS-myr:GFP*
- *ABLK>Bero:FLAG* (*n* = 72): *w[*]/y[1] v[1]; Lk-GAL4, tsh-LexA/tubP-FRT-GAL80-FRT; LexAop-FLP.L/UAS-Bero:FLAG*
- *y w, myr:GFP* (*n* = 60): *w[*]/y[1] v[1]; tubP-FRT-GAL80-FRT/+; UAS-myr:GFP/+*
- *y w,Bero:FLAG* (*n* = 61): *w[*]/y[1] v[1]; tubP-FRT-GAL80-FRT/+; UAS-Bero:FLAG/+*

The *P*-values obtained from the statistical analysis using the Wilcoxon rank sum test were as follows: 0.00192 and 0.11907, respectively.

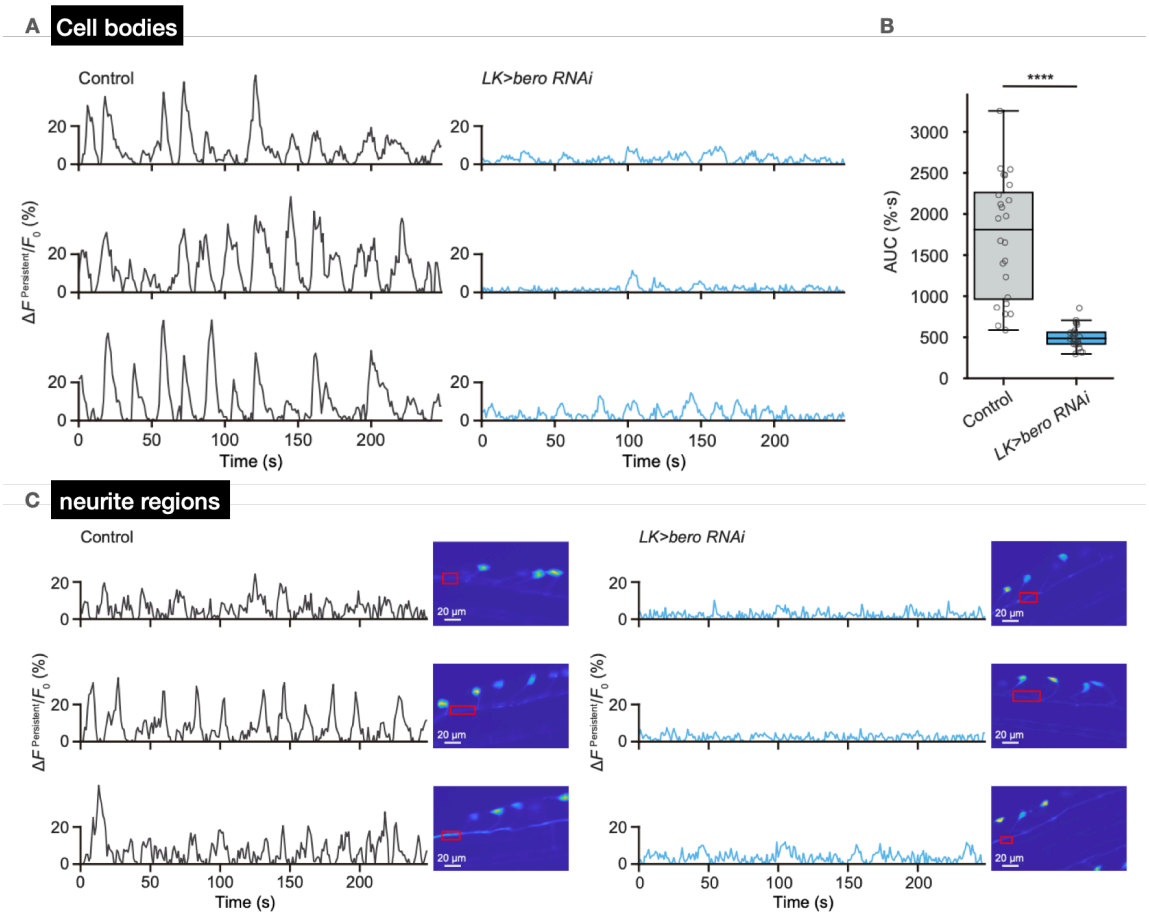

Figure 17. Spontaneous calcium fluctuations observed in ABLK neurons' cell bodies and neurites, and *bero* knockdown suppressed these activities

(A) The figure presents representative results of calcium responses, specifically showcasing the sustained fluctuations in calcium signal ($\Delta F^{\text{Persistent}}/F_0$, as defined in the Method) observed in the cell bodies of ABLK neurons in control larvae and the suppressed fluctuation in *bero* knockdown larvae. It should be noted that the scale of y-axes of the panels are different from those in Figure 18A and B. The genotypes and sample numbers for each group were as follows:

- Control (n = 24 neurons from 3 larvae): *y[1] w[*]/y[1] v[1]; TrpA1-QF, QUAS-ChR2.T159C-HA/Lk-GAL4, UAS-CD4-tdGFP; UAS-jRCaMP1b, P{}attP2/+*
- *LK>bero RNAi* (n = 25 neurons from 3 larvae): *y[1] w[*]/y[1] v[1]; TrpA1-QF, QUAS-ChR2.T159C-HA/Lk-GAL4, UAS-CD4-tdGFP; UAS-jRCaMP1b, P{VALIUM20-bero[shRNA#2]}attP2/+*

(B) A boxplot comparing the area under the curve (AUC) of sustained oscillatory activities of ABLK neurons in control and *bero* knockdown larvae is presented. The statistical analysis using the Wilcoxon rank sum test indicates a significant difference ($P < 0.0001$).

(C) The figure presents representative results of calcium responses, specifically showcasing the sustained oscillatory activities ($\Delta F^{\text{Persistent}}/F_0$) observed at the neurites of ABLK neurons in control larvae and the suppressed activities in *bero* knockdown larvae. Confocal microscopy images illustrating the specific region of interest. It should be noted that the scale of y-axes of the

panels are different from those in Figure 18A and B. Scale bars provided indicate 20 μm. In the above experiments, ATR was not added to the food. The whole calcium imaging experiment was performed by Yuma Tsukasa.

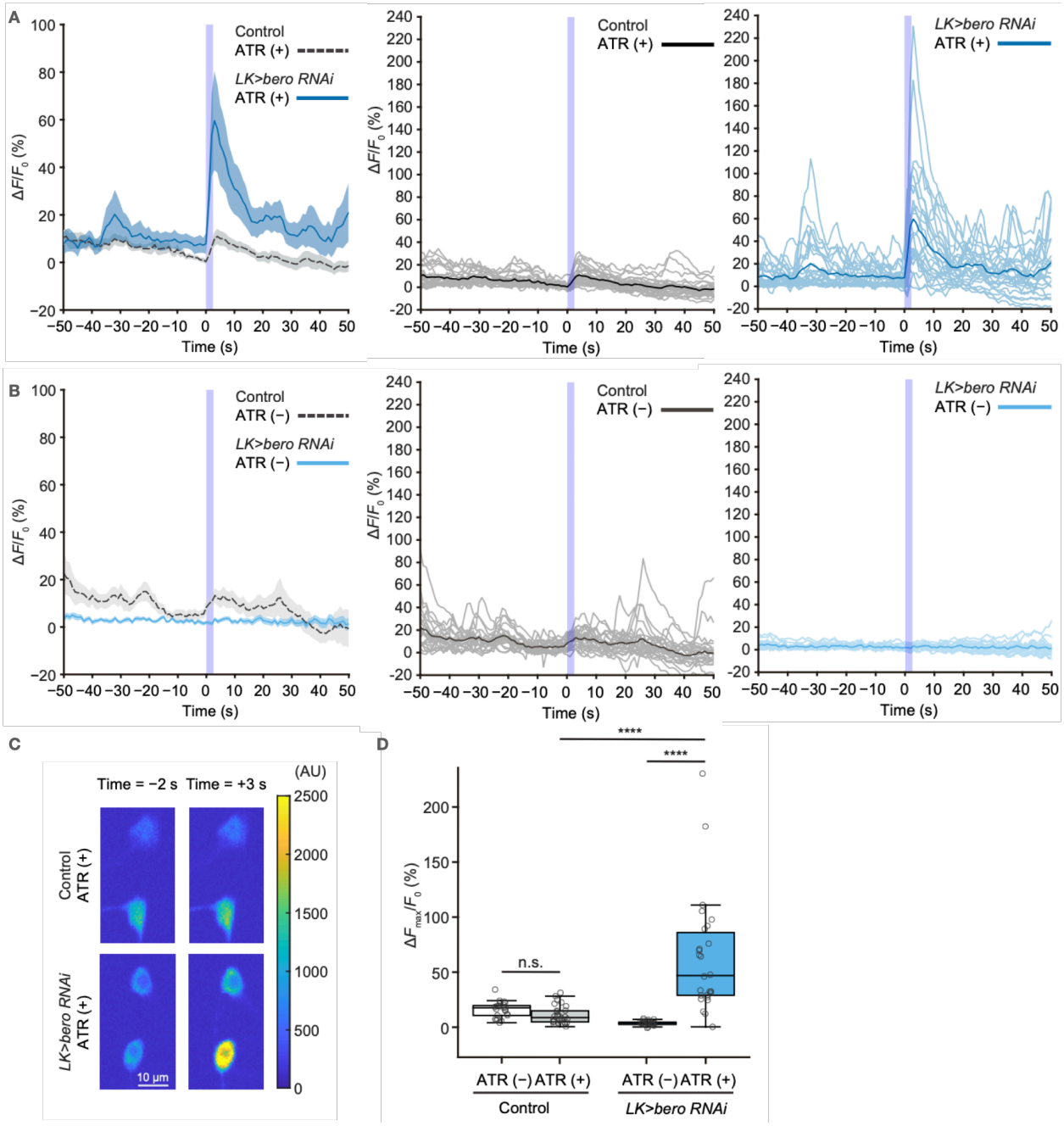

Figure 18. ABLK neurons exhibited immediate nociceptive reactions, and *bero* knockdown augmented these responses

(A) A time course analysis was conducted to examine calcium responses ($\Delta F/F_0$; as defined in the Method) of ABLK neurons in control larvae and *bero* knockdown larvae subjected to optogenetic activation of Class IV neurons, the nociceptors. The activation was achieved using 470-nm blue light for a duration of 2.5 seconds. Both groups of larvae were reared on food supplemented with ATR. The duration of light stimulation is represented by violet shading, while the light blue and gray shading indicated the standard error of the mean (± SEM). The middle and right panels depict detailed calcium response recording traces over time. It should be

noted that the scale of y-axes of the panels are different from those in Figure 17A and C. The averaged traces are represented by dark lines. The genotypes and sample numbers for each group were as follows:

- Control, ATR (+) (n = 29 neurons from 3 larvae): *y[1] w[*]/y[1] v[1]; TrpA1-QF, QUAS-ChR2.T159C-HA/Lk-GAL4, UAS-CD4-tdGFP; UAS-jRCaMP1b, P{}attP2/+*
- *LK>bero RNAi*, ATR(+) (n = 27 neurons from 3 larvae): *y[1] w[*]/y[1] v[1]; TrpA1-QF, QUAS-ChR2.T159C-HA/Lk-GAL4, UAS-CD4-tdGFP; UAS-jRCaMP1b, P{VALIUM20-bero[shRNA#2]}attP2/+*

(B) A time course analysis of calcium responses in ABLK neurons upon optogenetic activation of nociceptors in control larvae and *bero* knockdown larvae reared on food without supplementary ATR. The middle and right panels depict detailed calcium response recording traces over time. It should be noted that the scale of y-axes of the panels are different from those in Figure 17A and C. The averaged traces are represented by dark lines. The genotypes and sample numbers for each group were as follows:

- Control, ATR (−) (n = 24 neurons from 3 larvae): *y[1] w[*]/y[1] v[1]; TrpA1-QF, QUAS-ChR2.T159C-HA/Lk-GAL4, UAS-CD4-tdGFP; UAS-jRCaMP1b, P{}attP2/+*
- *LK>bero RNAi*, ATR (−) (n = 25 neurons from 3 larvae): *y[1] w[*]/y[1] v[1]; TrpA1-QF, QUAS-ChR2.T159C-HA/Lk-GAL4, UAS-CD4-tdGFP; UAS-jRCaMP1b, P{VALIUM20-bero[shRNA#2]}attP2/+*

(C) Representative confocal images depict the altered nociceptive responses of ABLK neurons in control larvae and *bero* knockdown larvae raised on ATR-supplemented food, before and after the optogenetic activation of nociceptors. The intensity of calcium signal is visualized through a heat map. Scale bars measuring 10 μm are included.

(D) The boxplot provides a quantitative comparison of the maximum calcium responses ($\Delta F_{max}/F_0$; as defined in the Method) observed in ABLK neurons of control and *bero* knockdown larvae in (A) and (B) upon the optogenetic activation of nociceptors. Statistical analysis using the Kruskal-Wallis test followed by Dunn's test revealed a significant difference between control and *bero* knockdown larvae raised on ATR food ($P < 0.0001$), as well as between *bero* knockdown larvae raised on food with and without supplementary ATR ($P < 0.0001$). The P-value for the comparison between control larvae raised on food with and without supplementary ATR was 0.0646. The whole calcium imaging experiment was performed by Yuma Tsukasa.

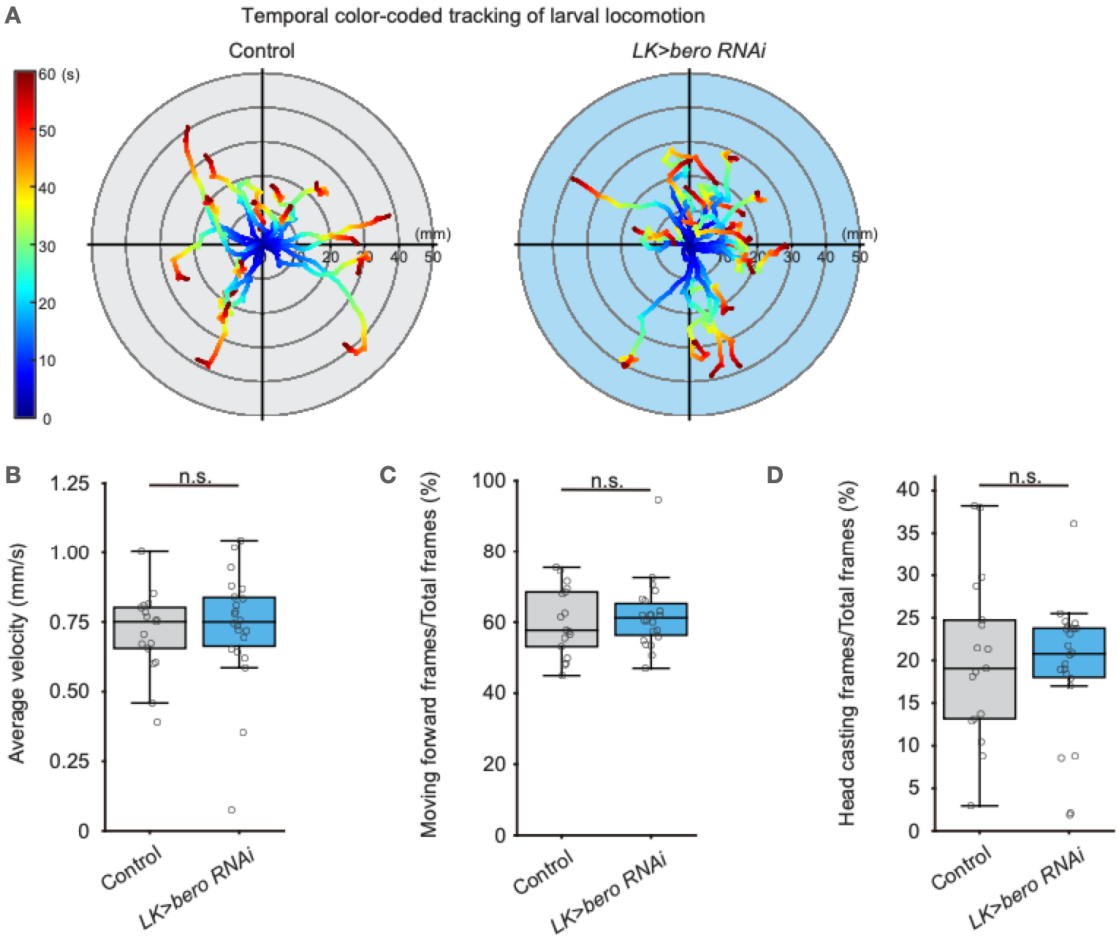

Figure 19. Analysis of undisturbed free locomotion in larvae with *bero* knockdown

(A) Temporal color-coded tracking of free locomotion was conducted on both control larvae and bero knockdown larvae, visualizing the time course through a heat map. Additional analyses are presented in panels (B), (C), and (D). The genotypes and sample numbers for each group were as follows:

- Control (n = 17): *y[1] w[*]/y[1] v[1]; +/Lk-GAL4, UAS-CD4-tdGFP; attP2/+*
- *LK>bero RNAi* (n = 22): *y[1] w[*]/y[1] v[1]; +/Lk-GAL4, UAS-CD4-tdGFP; UAS-bero[shRNA#2]/+*

(B) The average velocity was measured for control larvae and *bero* knockdown larvae. The results did not show a significant difference (P = 0.5101) based on the Wilcoxon rank sum test.
(C) The boxplot illustrates the analysis of the fraction of moving forward frames in control larvae and *bero* knockdown larvae. The comparison between the two groups did not yield a significant difference (P = 0.7002) based on the Wilcoxon rank sum test.
(D) The boxplot illustrates the analysis of the fraction of head casting frames in control larvae and *bero* knockdown larvae. The comparison between the two groups did not yield a significant difference (P = 0.9053) based on the Wilcoxon rank sum test. The locomotion assay was performed by Kaho Maeta.

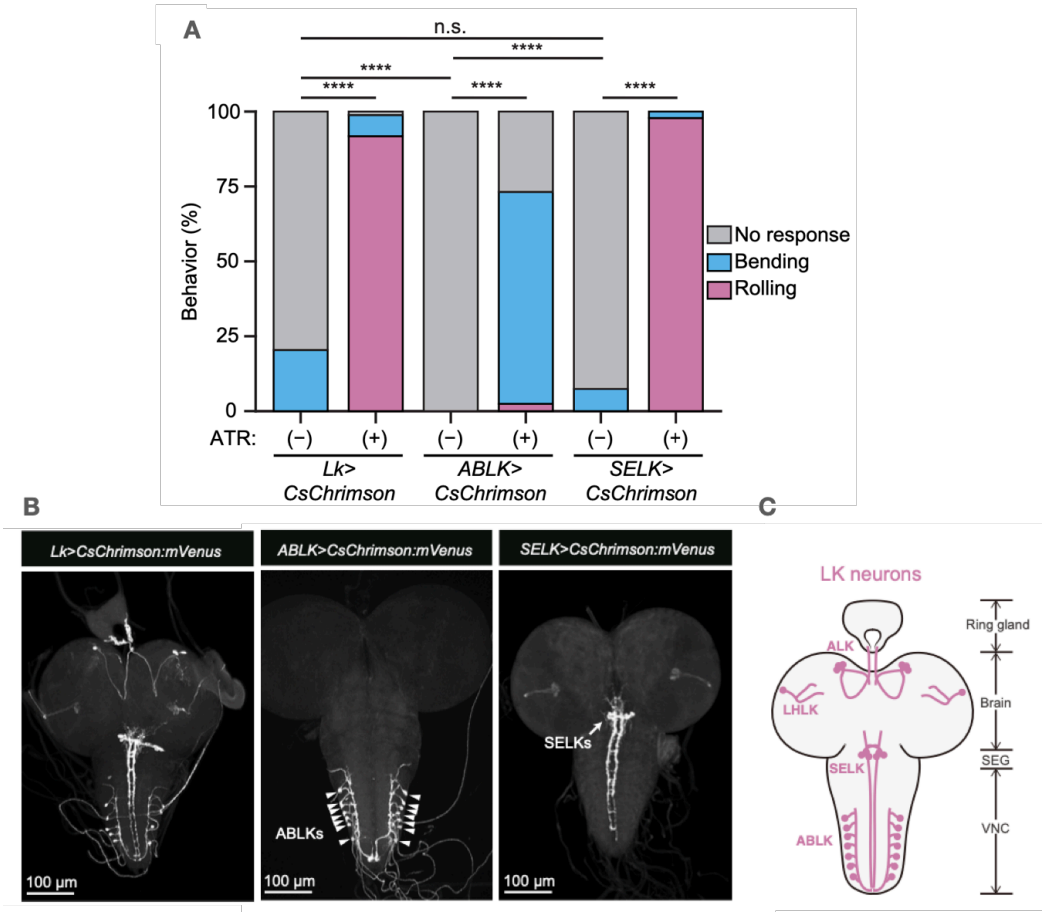

Figure 20. Optogenetic activation of distinct LK neurons

(A) The stacked bar chart illustrates the percentage of larvae exhibiting nociceptive escape behavior, specifically rolling and bending, following optogenetic activation of LK neurons, ABLK neurons, and SELK neurons. The analysis includes larvae raised on food supplemented with and without additional ATR. The genotypes and sample numbers for each group were as follows:

- *Lk>CsChrimson*, ATR (+) (n = 85) and ATR (−) (n = 49): *w[1118]; Lk-GAL4/UAS-CsChrimson.mVenus; +/+*
- *ABLK>CsChrimson*, ATR (+) (n = 41) and ATR (−) (n = 22): *w[*]/y[1] v[1]; Lk-GAL4, tsh-LexA/tubP-FRT-GAL80-FRT; LexAop-FLP.L/UAS-CsChrimson.mVenus*
- *SELK>CsChrimson*, ATR (+) (n = 46) and ATR (−) (n = 54): *w[*]/y[1] v[1]; Lk-GAL4, LexAop-FLP/tubP-FRT-GAL80-FRT; Scr-LexA/UAS-CsChrimson.mVenus*

The *P*-values obtained from the Chi-squared test were all less than 0.0001, except for the comparison between *Lk* and *SELK>CsChrimson* ATR (−) animals, which had a *P*-value of 0.36957.

(B) Confocal image stacks are presented, demonstrating the specific labeling of LK neurons, ABLK neurons, and SELK neurons in 3rd instar larvae with the same genotypes as those used in the panel (A). Scale bars measuring 100 µm are provided.

(C) A schematic map illustrating the different types of LK neurons is presented.

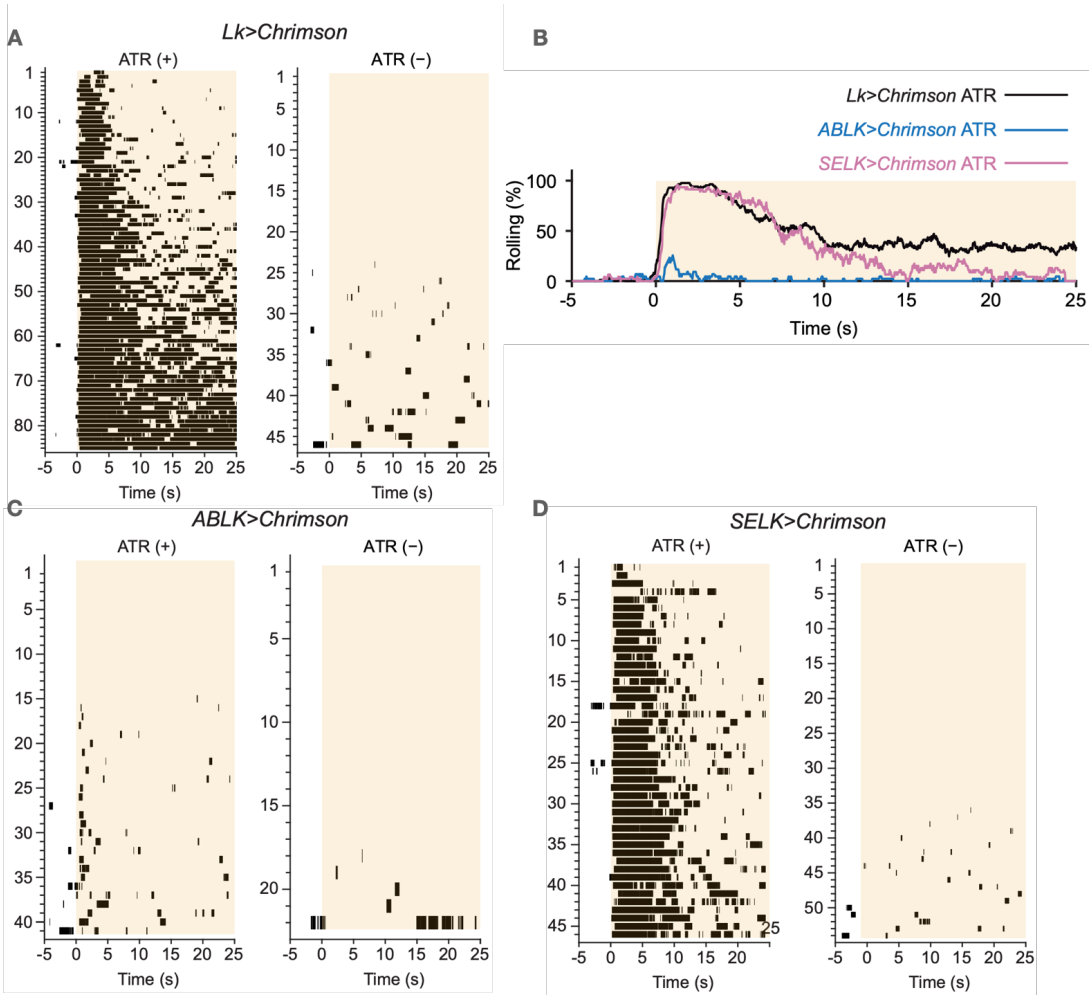

Figure 21. An unbiased automated analysis of larval behavior following the optogenetic activation of distinct LK neurons

(A) Raster plots depicting nociceptive escape events elicited by optogenetic activation of LK neurons are presented. The analysis includes larvae raised on food supplemented with and without additional ATR. The application of 590-nm orange light is indicated by orange shading, commencing at Time 0 s and lasting for 25 s. The Y-axis represents the number of samples. The genotypes of the samples correspond to those depicted in Figure 20.
(B) The figure displays time series data showing the rolling probability upon LK-specific, ABLK-specific, and SELK-specific optogenetic activation of larvae reared on food supplemented with extra ATR. The panels (A), (C), and (D) correspond to the different genotypes analyzed.
(C) Raster plots depicting nociceptive escape events elicited by optogenetic activation of ABLK neurons are presented, including larvae raised on food supplemented with and without additional ATR.
(D) Raster plots depicting nociceptive escape events elicited by optogenetic activation of SELK neurons are presented, including larvae raised on food supplemented with and without additional ATR.

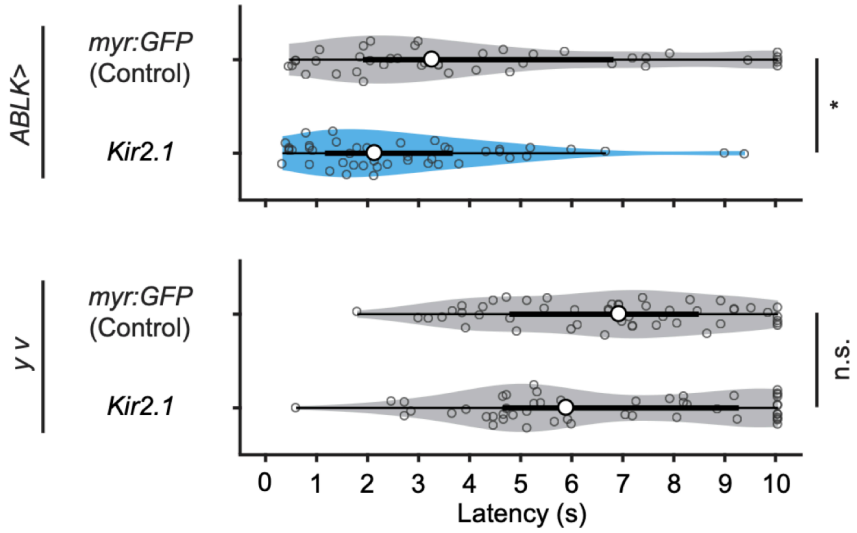

Figure 22. Silencing ABLK neurons through Kir2.1 expression slightly promoted escape behavior

The rolling latency of *ABLK>myr:GFP* control was compared to that of ABLK-specific inhibition animals. A set of effector-control is also presented. The genotypes and sample numbers for each group were as follows:

- *ABLK>myr:GFP* (control, *n* = 42): *w[*]/y[1] v[1]; Lk-GAL4, tsh-LexA/tubP-FRT-GAL80-FRT; LexAop-FLP.L/UAS-myr:GFP*
- *ABLK>Kir2.1* (*n* = 45): *w[*]/y[1] v[1]; Lk-GAL4, tsh-LexA/tubP-FRT-GAL80-FRT; LexAop-FLP.L/UAS-Kir2.1:GFP*
- *y v, myr:GFP* (*n* = 50): *w[*]/y[1] v[1]; tubP-FRT-GAL80-FRT/+; UAS-myr:GFP/+*
- *y v,Kir2.1* (*n* = 50): *w[*]/y[1] v[1]; tubP-FRT-GAL80-FRT/+; UAS-Kir2.1:GFP/+*

The *P*-values obtained from the Wilcoxon rank sum test were 0.02204 and 0.99449, respectively.

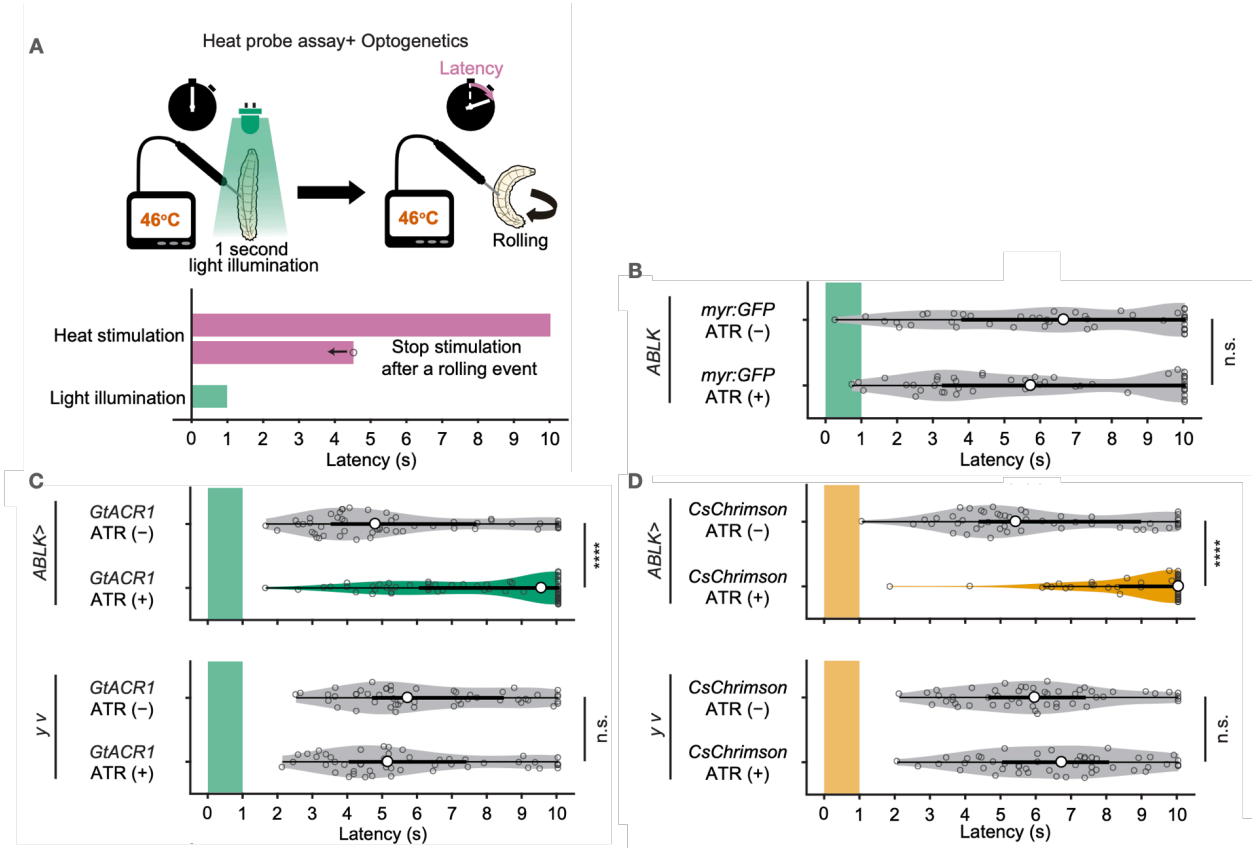

Figure 23. Both optogenetic activation and inhibition of ABLK neurons suppressed escape behavior

(A) A diagram illustrating the Heat Probe Assay in conjunction with optogenetic manipulation is presented (see Methods for detailed information). The heat stimulation and light illumination were administered nearly simultaneously: larvae were gently touched with a heat probe until it initiated the first complete 360° rotation. If the response latency exceeded 10 seconds, it was recorded as 10.05 seconds. A 1-second light illumination was applied for optogenetic manipulation.

(B) The rolling latency of *ABLK>myr:GFP* ATR (−) driver-control was compared to that of animals reared on food with extra ATR. The genotypes and sample numbers for each group were as follows:

- *ABLK>myr:GFP*, ATR (+) (n = 46) and ATR (−) (n = 45): *w[*]/y[1] v[1]; Lk-GAL4, tsh-LexA/tubP-FRT-GAL80-FRT; LexAop-FLP.L/UAS-myr:GFP*

The *P*-values obtained from the Wilcoxon rank sum test was 0.42883.

(C) The rolling latency of *ABLK>GtACR1* ATR (−) control was compared to that of animals reared on food with extra ATR. A set of effector-control is also presented. The genotypes and sample numbers for each group were as follows:

- *ABLK>GtACR1*, ATR (+) (n = 68) and ATR (−) (n = 54): *w[*]/y[1] v[1]; Lk-GAL4, tsh-LexA/tubP-FRT-GAL80-FRT; LexAop-FLP.L/UAS-GtACR1*
- *y v, GtACR1*, ATR (+) (n = 50) and ATR (−) (n = 50): *w[*]/y[1] v[1]; tubP-FRT-GAL80-FRT/+; UAS-GtACR1/+*

The *P*-values obtained from the Wilcoxon rank sum test were < 0.0001 and 0.11262, respectively.

(D) The rolling latency of *ABLK>CsChrimson* ATR (−) control was compared to that of animals reared on food with extra ATR. A set of effector-control is also presented. The genotypes and sample numbers for each group were as follows:

- *ABLK>CsChrimson*, ATR (+) (*n* = 53) and ATR (−) (*n* = 52): *w[*]/y[1] v[1]; Lk-GAL4, tsh-LexA/tubP-FRT-GAL80-FRT; LexAop-FLP.L/UAS-CsChrimson.mVenus*
- *y v, CsChrimson*, ATR (+) (*n* = 50) and ATR (−) (*n* = 50): *w[*]/y[1] v[1]; tubP-FRT-GAL80-FRT/+; UAS-CsChrimson.mVenus/+*

The *P*-values obtained from the Wilcoxon rank sum test were < 0.0001 and 0.17647, respectively.

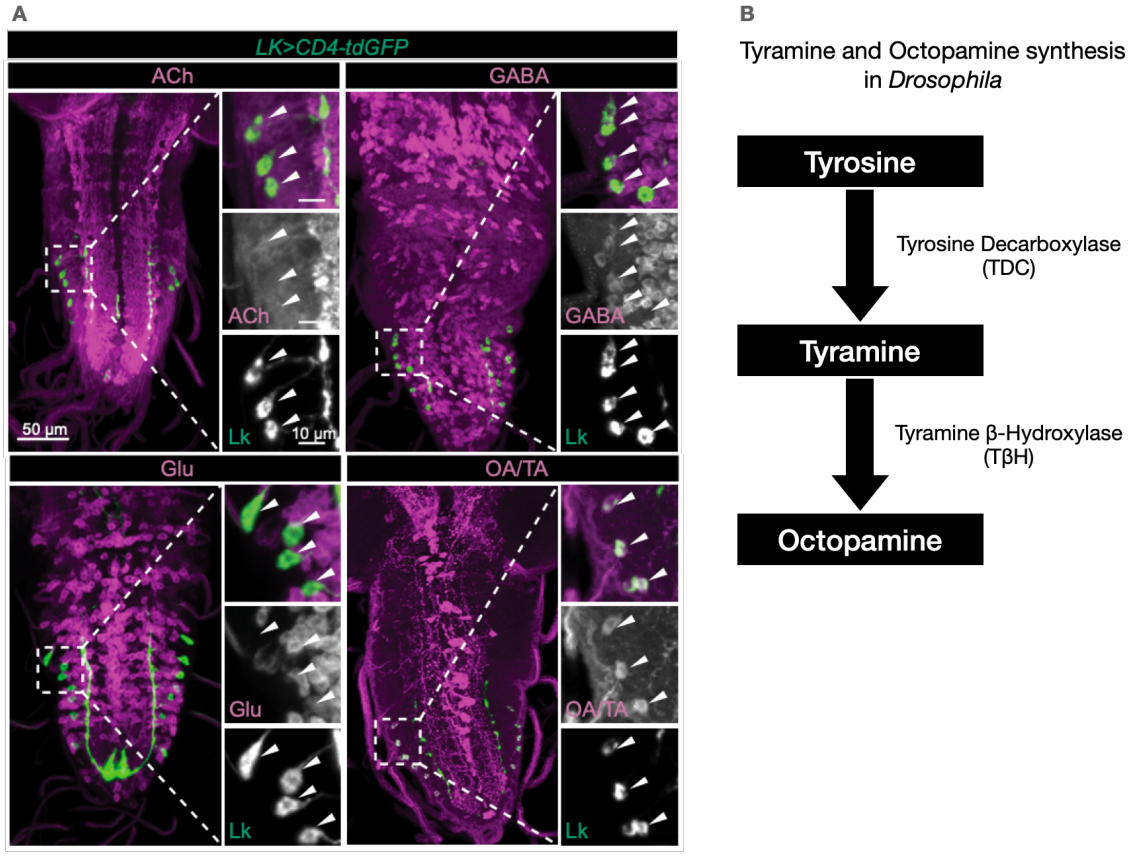

Figure 24. Expression of tyrosine decarboxylase 2 (Tdc2) in ABLK neurons

(A) Maximum projections of confocal image stacks are presented, visualizing LK neurons labeled with *LK>CD4-tdGFP* (shown in green), as well as different types of neurons identified by specific neurotransmitter markers. These included cholinergic neurons labeled with anti-ChAT, GABAergic neurons labeled with anti-GABA, glutamatergic neurons labeled with *VGlut-T2A-LexA>LexAop-jRCaMP1b*, as well as tyraminergic and/or octopaminergic neurons labeled with anti-Tdc2 in 3rd instar larvae (depicted in magenta). Magnified panels provide a detailed view of the selected region of interest. ABLK neurons are marked with arrowheads. The scale bars represent 50 µm for the main images and 10 µm for the enlarged view. The genotypes and used antibodies for each group were as follows:

- ACh: *y[1] w[*]; LK-GAL4, UAS-hCD4-tdGFP; +/+*, Mouse monoclonal anti-ChAT (1:50), Alexa Fluor® 546-conjugated anti-Mouse IgG (1:500)
- GABA: *y[1] w[*]; LK-GAL4, UAS-hCD4-tdGFP; +/+*, Rabbit polyclonal anti-GABA (1:100), Alexa Fluor® 546-conjugated anti-Rabbit IgG (1:500)
- Glu: *y[1] w[*]; LK-GAL4, UAS-hCD4-tdGFP/vGlut-LexA, LexAop-jRCaMP1b; UAS-ChR2.T159C-HA/+*
- GABA: *y[1] w[*]; LK-GAL4, UAS-hCD4-tdGFP; +/+*, Rabbit polyclonal anti-Tdc2 (1:1000), Alexa Fluor® 546-conjugated anti-Rabbit IgG (1:500)

The immunohistochemistry staining was performed by Yuma Tsukasa.

(B) A diagram illustrating Tyrosine Decarboxylase 2 and Tyramine β-Hydroxylase as key synthetic enzymes for Tyramine and Octopamine synthesis in *Drosophila*

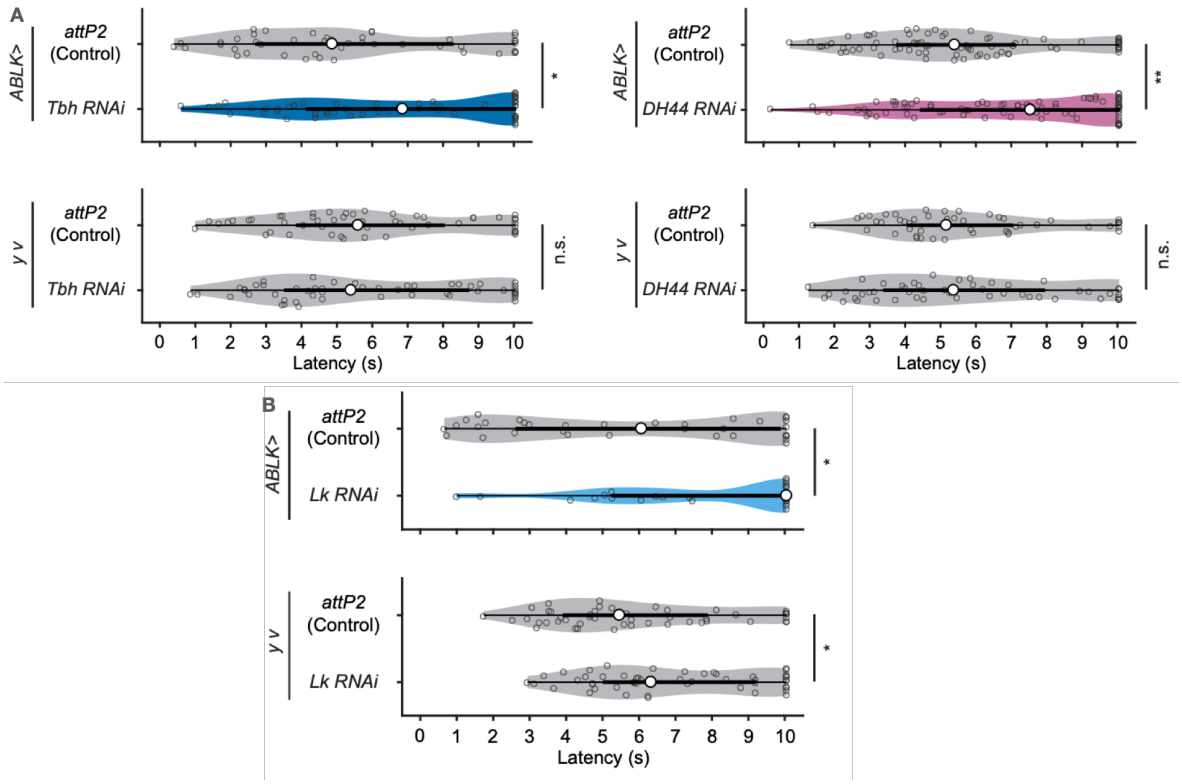

Figure 25. Knockdown of *Dh44* or *Tβh* in ABLK neurons suppressed escape behavior

(A) The rolling latency of control was compared to that of ABLK-specific *Tβh* or *DH44* knockdown larvae. Sets of effector-control are also presented. The genotypes and sample numbers for each group were as follows:

- *ABLK>attP2* ($n = 45$): *w[*]/y[1] v[1]; Lk-GAL4, tsh-LexA/tubP-FRT-GAL80-FRT; LexAop-FLP.L/attP2*
- *ABLK>Tbh RNAi* ($n = 59$): *w[*]/y[1] v[1]; Lk-GAL4, tsh-LexA/tubP-FRT-GAL80-FRT; LexAop-FLP.L/UAS-Tbh-RNAi*
- *y v, attP2* ($n = 52$): *w[*]/y[1] v[1]; tubP-FRT-GAL80-FRT/+; attP2/+*
- *y v, Tbh RNAi* ($n = 51$): *w[*]/y[1] v[1]; tubP-FRT-GAL80-FRT/+; UAS-Tbh-RNAi/+*

The *P*-values obtained from the Wilcoxon rank sum test were 0.02695 and 0.83238, respectively.

- *ABLK>attP2* ($n = 79$): *w[*]/y[1] v[1]; Lk-GAL4, tsh-LexA/tubP-FRT-GAL80-FRT; LexAop-FLP.L/attP2*
- *ABLK>DH44 RNAi* ($n = 83$): *w[*]/y[1] v[1]; Lk-GAL4, tsh-LexA/tubP-FRT-GAL80-FRT; LexAop-FLP.L/UAS-DH44-RNAi*
- *y v, attP2* ($n = 48$): *w[*]/y[1] v[1]; tubP-FRT-GAL80-FRT/+; attP2/+*
- *y v, DH44 RNAi* ($n = 50$): *w[*]/y[1] v[1]; tubP-FRT-GAL80-FRT/+; UAS-DH44-RNAi/+*

The *P*-values obtained from the Wilcoxon rank sum test were 0.00238 and 0.85602, respectively.

(B) The rolling latency of control was compared to that of ABLK-specific *Lk* knockdown larvae. A set of effector-control is also presented. The genotypes and sample numbers for each group were as follows:

- *ABLK>attP2* ($n = 42$): *w[*]/y[1] v[1]; Lk-GAL4, tsh-LexA/tubP-FRT-GAL80-FRT; LexAop-FLP.L/attP2*

- *ABLK>Lk RNAi* (*n* = 33): *w[*]/y[1] v[1]; Lk-GAL4, tsh-LexA/tubP-FRT-GAL80-FRT; LexAop-FLP.L/UAS-LK-RNAi*
- *y v, attP2* (*n* = 48): *w[*]/y[1] v[1]; tubP-FRT-GAL80-FRT/+; attP2/+*
- *y v, Lk RNAi* (*n* = 50): *w[*]/y[1] v[1]; tubP-FRT-GAL80-FRT/+; UAS-LK-RNAi/+*

The *P*-values obtained from the Wilcoxon rank sum test were 0.02627 and 0.04064, respectively.

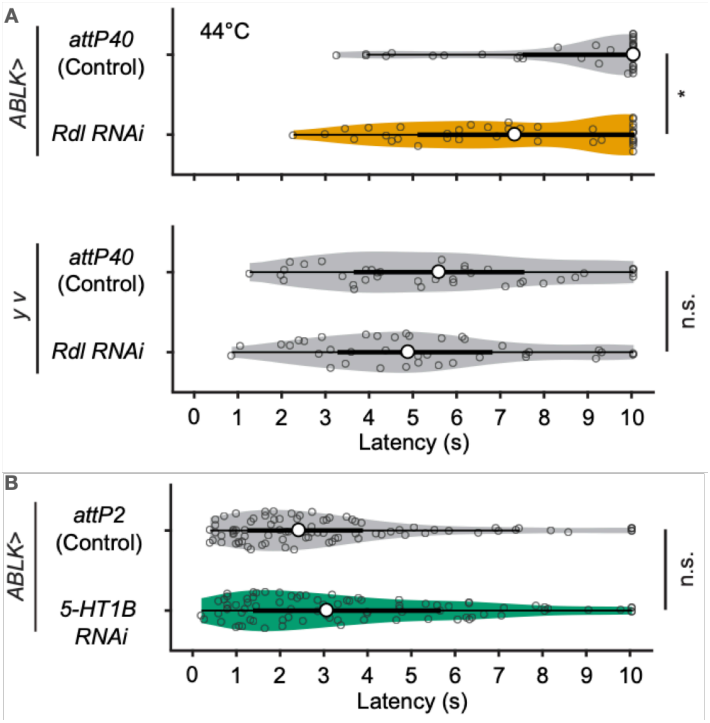

Figure 26. Examining the relevance of ABLK neuronal receptors in facilitating nociceptive escape behavior

(A) The rolling latency of control was compared to that of ABLK-specific *Rdl* knockdown larvae following heat stimulations at 44°C. A set of effector-control is also presented. The genotypes and sample numbers for each group were as follows:

- *ABLK>attP40* (n = 42): *w[*]/y[1] v[1]; Lk-GAL4, tsh-LexA/attP40; LexAop-FLP.L/tubP-FRT-GAL80-FRT*
- *ABLK>Rdl RNAi* (n = 38): *w[*]/y[1] v[1]; Lk-GAL4, tsh-LexA/UAS-Rdl RNAi; LexAop-FLP.L/tubP-FRT-GAL80-FRT*
- *y v, attP40* (n = 38): *w[*]/y[1] v[1]; attP40/+; tubP-FRT-GAL80-FRT/+*
- *y v, Rdl RNAi* (n = 40): *w[*]/y[1] v[1]; UAS-Rdl RNAi/+; tubP-FRT-GAL80-FRT/+*

The *P*-values obtained from the Wilcoxon rank sum test were 0.01213 and 0.52204, respectively.

(B) The rolling latency of control was compared to that of ABLK-specific *5-HT1B* knockdown larvae. The genotypes and sample numbers for each group were as follows:

- *ABLK>attP2* (n = 86): *w[*]/y[1] v[1]; Lk-GAL4, tsh-LexA/tubP-FRT-GAL80-FRT; LexAop-FLP.L/attP2*
- *ABLK>5-HT1B RNAi* (n = 83): *w[*]/y[1] v[1]; Lk-GAL4, tsh-LexA/tubP-FRT-GAL80-FRT; LexAop-FLP.L/UAS-5-HT1B-RNAi*

The *P*-values obtained from the Wilcoxon rank sum test was 0.20274.

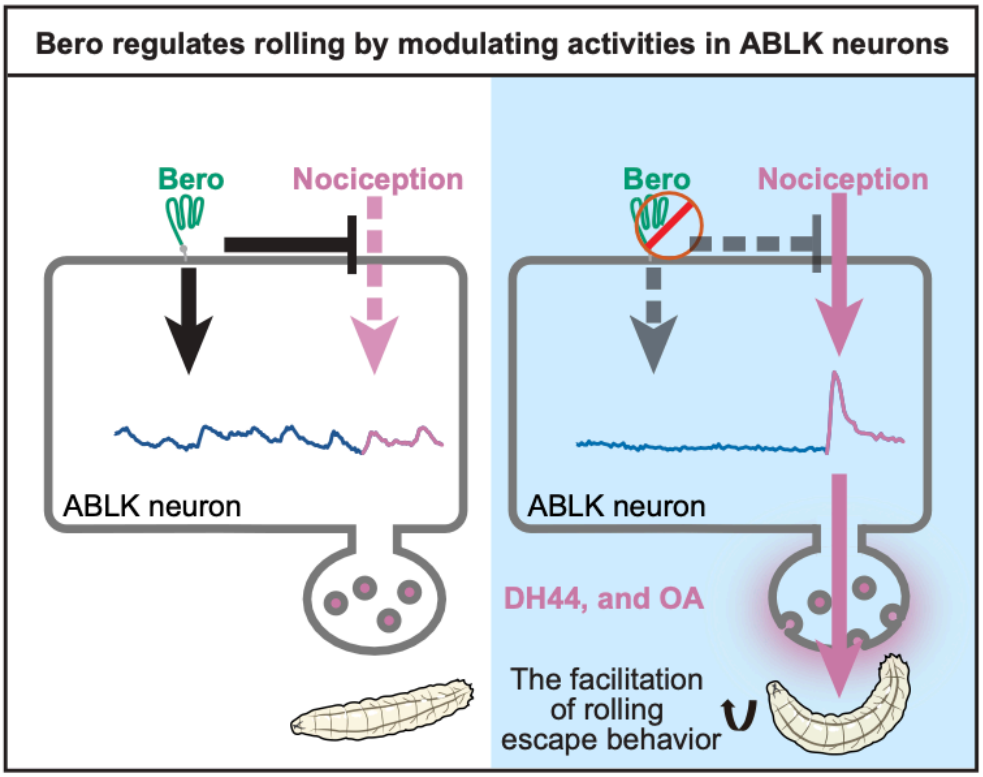

Figure 27. A diagram summarizing the regulatory role of Bero in escape behavior

In the left panel, in the present of *bero*, the activity of ABLK neurons exhibited normal sustained oscillatory patterns and effectively suppressed nociceptive responses upon stimulation. Conversely, in the right panel, the knockdown of *bero* in ABLK neurons resulted in diminished sustained oscillatory activities and heightened nociceptive responses. Furthermore, the knockdown of *bero* in ABLK neurons promoted the rolling escape behavior of the larvae. These findings highlight the essential role of ABLK neurons and *bero* in facilitating nociceptive escape behavior, with DH44 and octopamine identified as significant neurotransmitters involved in this process. The gray regions represent ABLK neurons, while the green three-finger structure represents Bero protein. The blue lines represent the spontaneous activities in ABLK neuron, while the pink lines represent the nociceptive responses.

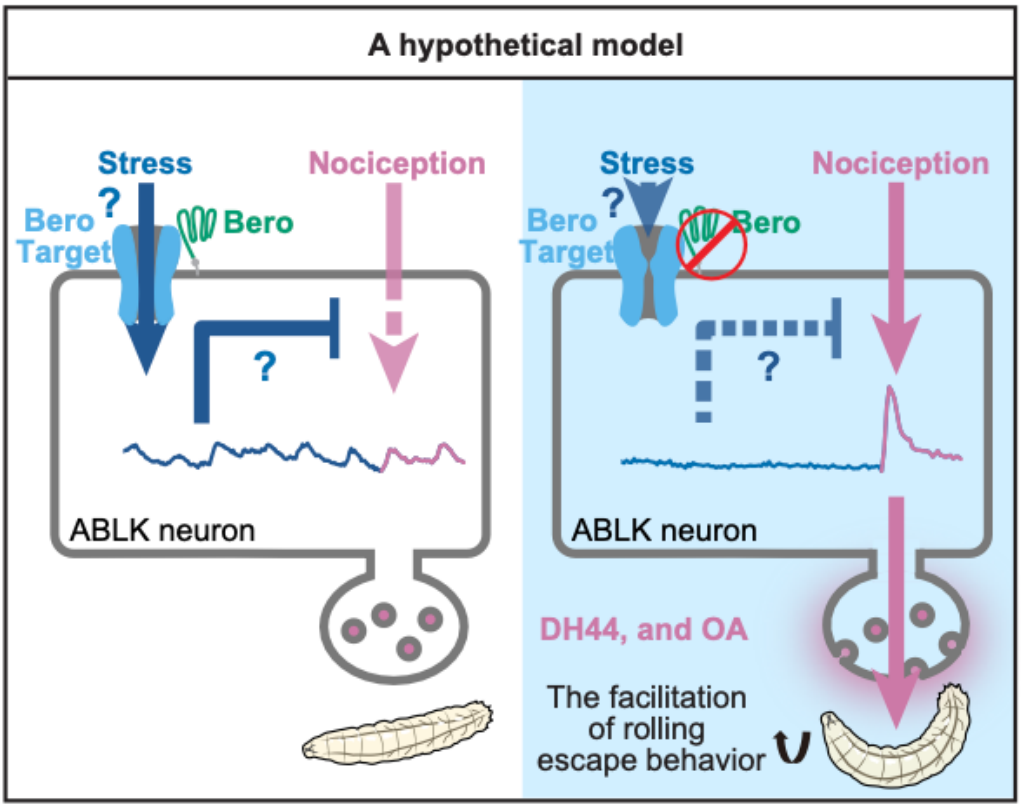

Figure 28. A hypothetical model illustrating how Bero regulates rolling escape behavior through the modulation of activities in ABLK neurons

In the left panel, Bero specifically interacts with a critical protein involved in initiating sustained oscillatory activities in ABLK neurons, leading to the modulation of nociceptive responses in ABLK neurons and ultimately suppressing nociceptive escape behavior. Conversely, in the right panel, the downregulation of *bero* in ABLK neurons hinders the functionality of its specific target effector protein, resulting in reduced sustained oscillatory activities and heightened nociceptive responses, ultimately promoting escape behavior. The underlying hypothesis is based on the Ca^{2+}-dependent inhibition of excitatory signals within ABLK neurons. Specifically, the effector protein targeted by *bero* has the potential to elevate intracellular calcium levels, thereby interfering with the opening of voltage-gated cation channels and suppressing nociceptive responses in ABLK neurons. The gray regions represent ABLK neurons, while the green three-finger structure represents the Bero protein. The blue barrel structure represents the hypothetical effector protein targeted by Bero. The blue lines depict spontaneous activities in ABLK neurons, while the pink lines represent nociceptive responses.

Supplemental Tables

Statistical metrics	Genetic variant	Association p-value	Associating genes (location)
Rolling probability in 5 seconds	2L_12154931_SNP	3.87E-07	CG31760[intron]
	2R_15876464_SNP	4.85E-07	Intergenic
	2R_11379158_SNP	1.25E-06	CG12964[intron]
	2L_12155190_SNP	1.58E-06	CG31760[intron]
	2L_12155191_SNP	1.58E-06	CG31760[intron]
	2R_5702481_SNP	1.59E-06	CG1648[intron], lectin-46Cb[upstream]
	2L_14862649_SNP	1.70E-06	Intergenic
	2L_20859945_SNP	2.21E-06	CG9336[intron]
	2L_2576383_SNP	3.70E-06	insv[non synonymous coding]
	3L_21799863_SNP	4.06E-06	Intergenic
	3L_16030154_SNP	4.37E-06	CG5895[synonymous coding]
	X_10938087_SNP	5.04E-06	CG11160[upstream]
	X_15876214_SNP	5.04E-06	CG9170[intron]
	3L_14482462_SNP	5.08E-06	bbg[intron]
	X_10937994_SNP	5.65E-06	CG11160[upstream]
	3R_8376371_SNP	6.40E-06	mir-284[downstream], Octβ2R[UTR5']
	X_5208599_SNP	6.79E-06	CG4198[non synonymous coding]
	3L_11536089_SNP	7.07E-06	Mob2[intron]
	X_19001836_SNP	7.11E-06	Intergenic
	3L_5559190_SNP	8.00E-06	bc10[UTR3']
	X_11111441_SNP	9.47E-06	Intergenic
Rolling probability in 10 seconds	3R_1271336_SNP	4.85E-07	CG14669[intron]
	2R_10010517_SNP	8.16E-07	Prosap[intron]
	3R_14831753_SNP	1.24E-06	gukh[intron]
	3L_22130777_SNP	4.36E-06	olf413[intron]
	2L_15180803_SNP	5.86E-06	CG4168[intron]
	2L_15180836_SNP	5.86E-06	CG4168[intron]
	2L_15180861_SNP	5.86E-06	CG4168[intron]
	2L_15180863_SNP	5.86E-06	CG4168[intron]
	X_8937856_DEL	5.95E-06	CR43836[intron], Nost[intron]
	2L_15180815_SNP	6.85E-06	CG4168[intron]

	2L_15180816_SNP	6.85E-06	CG4168[intron]
	2R_20406585_SNP	7.64E-06	Ir60c[pseudogene], Ir60d[upstream]
	2L_14474334_SNP	8.02E-06	Intergenic
	3L_13762224_INS	8.77E-06	bru-3[intron]
	2L_15180827_SNP	8.89E-06	CG4168[intron]
	2R_17750945_SNP	9.30E-06	Intergenic
	3R_14832050_SNP	9.72E-06	gukh[intron]
	2R_15876464_SNP	8.17E-05	Intergenic
Average rolling latency	3L_17309565_SNP	3.48E-07	Intergenic
	2R_6913332_SNP	9.68E-07	luna[intron]
	2L_12154931_SNP	2.07E-06	CG31760[intron]
	X_3935741_SNP	2.80E-06	Intergenic
	2L_2343034_SNP	4.30E-06	eys[intron], CG9967[intron]
	2R_14977756_SNP	4.48E-06	5-HT1A[UTR5']
	3L_5860694_SNP	6.39E-06	Intergenic
	3L_17309558_SNP	6.81E-06	Intergenic
	3R_11000337_SNP	9.26E-06	Gyc88E[intron], Mf[intron]
	2R_15876464_SNP	9.27E-06	Intergenic
	2L_4020135_SNP	9.27E-06	Intergenic
	2L_3871457_INS	9.37E-06	CG31957[UTR5'], Cep97[downstream]
	2R_18117701_SNP	1.26E-05	Intergenic
	2R_6872535_SNP	2.10E-05	luna[intron]
Median rolling latency	3R_1271336_SNP	6.03E-07	CG14669[intron]
	2L_20859945_SNP	6.19E-07	CG9336[intron]
	2R_10010517_SNP	7.62E-07	Prosap[intron]
	2L_14474334_SNP	1.22E-06	Intergenic
	2R_15876464_SNP	2.14E-06	Intergenic
	2L_12154931_SNP	3.29E-06	CG31760[intron]
	X_9161361_INS	3.38E-06	Erk7[UTR5']
	2L_14474335_DEL	5.10E-06	Intergenic
	2L_2348898_SNP	8.23E-06	eys[intron], CG9967[intron]
	3L_21799863_SNP	8.26E-06	Intergenic
	3L_9821866_SNP	8.38E-06	CG43897[intron]
	3L_7638753_SNP	8.62E-06	Intergenic
	3L_14482462_SNP	8.65E-06	bbg[intron]

	2L_15180815_SNP	9.04E-06	CG4168[intron]
	2L_15180816_SNP	9.04E-06	CG4168[intron]
	3R_2776988_DEL	9.49E-06	Antp[intron]
	3R_2777001_SNP	9.49E-06	Antp[intron]

Table S1. GWAS results for escape behavior: 57 Hits

The term "associating genes" refers to genes located within a 1-kilobase range upstream or downstream of the target genetic variant.

Associating genes	Annotation Symbol	FlyBase ID	Genetic variant
CG4198	CG4198	FBgn0029753	X_5208599_SNP
CR43836	CR43836	FBgn0264384	X_8937856_DEL
Nost	CG42388	FBgn0259734	X_8937856_DEL
Erk7	CG32703	FBgn0052703	X_9161361_INS
SmydA-4	CG11160	FBgn0030257	X_10937994_SNP
			X_10938087_SNP
CG9170	CG9170	FBgn0030716	X_15876214_SNP
eys	CG33955	FBgn0031414	2L_2343034_SNP
			2L_2348898_SNP
CG9967	CG9967	FBgn0031413	2L_2343034_SNP
			2L_2348898_SNP
insv	CG3227	FBgn0031434	2L_2576383_SNP
Cep97	CG3980	FBgn0031575	2L_3871457_INS
CG31957	CG31957	FBgn0051957	2L_3871457_INS
CG31760	CG31760	FBgn0051760	2L_12154931_SNP
			2L_12155190_SNP
			2L_12155191_SNP
CG4168	CG4168	FBgn0028888	2L_15180803_SNP
			2L_15180815_SNP
			2L_15180816_SNP
			2L_15180827_SNP
			2L_15180836_SNP
			2L_15180861_SNP
			2L_15180863_SNP
CG9336	CG9336	FBgn0032897	2L_20859945_SNP
CG1648	CG1648	FBgn0033446	2R_5702481_SNP
lectin-46Cb	CG1652	FBgn0040092	2R_5702481_SNP
luna	CG33473	FBgn0040765	2R_6872535_SNP
			2R_6913332_SNP
Prosap	CG30483	FBgn0040752	2R_10010517_SNP
CG12964	CG12964	FBgn0034022	2R_11379158_SNP
5-HT1A	CG16720	FBgn0004168	2R_14977756_SNP
Ir60c[pseudogene]	CR42290	FBgn0259186	2R_20406585_SNP
Ir60d	CG42291	FBgn0259187	2R_20406585_SNP
bc10	CG4867	FBgn0040239	3L_5559190_SNP
CG43897	CG43897	FBgn0264489	3L_9821866_SNP
Mob2	CG11711	FBgn0259481	3L_11536089_SNP
bru-3	CG43744	FBgn0264001	3L_13762224_INS

bbg	CG42230	FBgn0087007	3L_14482462_SNP
CG5895	CG5895	FBgn0036560	3L_16030154_SNP
olf413	CG12673	FBgn0037153	3L_22130777_SNP
CG14669	CG14669	FBgn0037326	3R_1271336_SNP
Antp	CG1028	FBgn0260642	3R_2776988_DEL
			3R_2777001_SNP
mir-284	CR42906	FBgn0262383	3R_8376371_SNP
Octβ2R	CG33976	FBgn0038063	3R_8376371_SNP
Gyc88E	CG4154	FBgn0038295	3R_11000337_SNP
Mf	CG6803	FBgn0038294	3R_11000337_SNP
gukh	CG31043	FBgn0026239	3R_14831753_SNP
			3R_14832050_SNP

Table S2. GWAS results for escape behavior: 36 Associating genes

The term "associating genes" refers to genes located within a 1-kilobase range upstream or downstream of the target genetic variant. The 16 genes that were tested in the validation test in Figure 5 are indicated in bold font.

Putative sites for sequence with Minor allele: CTATAACATATAG			
Name	**Relative score**	**Strand**	**Predicted sequence**
MA0173.1.CG11617	0.890853417	+	ATAACAT
MA0015.1.Cf2	0.853220966	-	CTATATGTTA
MA0217.1.caup	0.999999992	+	TAACA
MA0233.1.mirr	0.996821244	+	TAACA
MA0210.1.ara	0.999999992	+	TAACA
MA0216.1.cad	0.814981804	-	GTTATAG
MA0448.1.H2.0	0.829190182	-	GTTATAG
MA0094.1.Ubx	0.851036034	-	TTAT
MA0094.1.Ubx	0.810436904	+	TAAC
Putative sites for sequence with Major allele: CTATAATATATAG			
Name	**Relative score**	**Strand**	**Predicted sequence**
MA0015.1.Cf2	0.857610372	-	CTATATATTA
MA0182.1.CG4328-RA	0.944635935	-	TATATTA
MA0174.1.Dbx	0.911159485	-	TATATTA
MA0197.1.nub	0.861809247	+	TATAATAT
MA0094.1.Ubx	1.000000009	+	TAAT
MA0216.1.cad	0.863038683	-	TATATTA
MA0448.1.H2.0	0.87320649	-	TATATTA
MA1836.1.dsx	0.827114096	+	CTATAATATAT
MA0178.1.CG32105	0.81884777	-	TATATTA
MA0176.1.CG15696-RA	0.828988741	-	TATATTA
MA0165.1.Abd-B	0.825259365	-	TATATTA
MA0448.1.H2.0	0.846453467	-	ATTATAG
MA0457.1.PHDP	0.82358773	+	ATAATAT
MA0195.1.Lim3	0.814150147	-	TATATTA
MA0216.1.cad	0.814981804	-	ATTATAG
MA0182.1.CG4328-RA	0.838716542	-	ATTATAG
MA0094.1.Ubx	0.851036034	-	TTAT
MA0216.2.cad	0.807256186	+	TATAATATATA

Table S3. Preliminary sequence analysis of the neighbouring sequence of 2L_20859945_SNP

A preliminary sequence analysis was conducted on the neighboring sequence of the 2L_20859945_SNP using the JASPAR CORE TF-binding profiles. This analysis aimed to identify potential transcription factor (TF) binding sites and their associated regulatory elements. Putative site(s) were predicted with relative profile score threshold 80%.

Genotypes of fly lines	SOURCE
w[1118]	BDSC: 3605
Canton-S	E-10002, *Drosophila* Stocks of Ehime University
y[1] w[1118]; P{y[+t7.7] w[+mC]=nSyb-GAL4.P}attP2	BDSC: 51941
y[1] v[1]; P{y[+t7.7] v[+t1.8]=TRiP.JF02463}attP2	BDSC: 33764
y[1] v[1]; P{y[+t7.7] v[+t1.8]=TRiP.JF02708}attP2	BDSC: 33766
y[1] v[1]; P{y[+t7.7] v[+t1.8]=TRiP.JF03422}attP2	BDSC: 31988
y[1] v[1]; P{y[+t7.7] v[+t1.8]=TRiP.JF02430}attP2	BDSC: 27084
y[1] sc[*] v[1] sev[21]; P{y[+t7.7] v[+t1.8]=TRiP.HMS02177}attP2/TM3, Sb[1]	BDSC: 40929
y[1] sc[*] v[1] sev[21]; P{y[+t7.7] v[+t1.8]=TRiP.HMS03010}attP2	BDSC: 36750
y[1] sc[*] v[1] sev[21]; P{y[+t7.7] v[+t1.8]=TRiP.HMC03681}attP2	BDSC: 55858
y[1] sc[*] v[1] sev[21]; P{y[+t7.7] v[+t1.8]=TRiP.HMC05799}attP2	BDSC: 64926
y[1] v[1]; P{y[+t7.7] v[+t1.8]=TRiP.HMC04378}attP2	BDSC: 56939
y[1] v[1]; P{y[+t7.7] v[+t1.8]=TRiP.JF01852}attP2	BDSC: 25834
y[1] v[1]; P{y[+t7.7] v[+t1.8]=TRiP.HMJ22879}attP40	BDSC: 60486
y[1] sc[*] v[1] sev[21]; P{y[+t7.7] v[+t1.8]=TRiP.HMC03410}attP2	BDSC: 51838
y[1] v[1]; P{y[+t7.7] v[+t1.8]=TRiP.JF03163}attP2/TM3, Sb[1]	BDSC: 28736
y[1] v[1]; P{y[+t7.7] v[+t1.8]=TRiP.JF01132}attP2	BDSC: 31560
y[1] sc[*] v[1] sev[21]; P{y[+t7.7] v[+t1.8]=TRiP.HMS02702}attP40	BDSC: 43318
y[1] v[1]; P{y[+t7.7] v[+t1.8]=TRiP.HM05096}attP2	BDSC: 28608
y[1] v[1]; P{y[+t7.7] v[+t1.8]=TRiP.JF02439}attP2	BDSC: 29547
y[1] v[1]; +; UAS-bero[shRNA #1]/TM6C Sb Tb	This paper
y[1] v[1]; +; UAS-bero[shRNA #2]/TM6C Sb Tb	This paper
w[1118]; P{y[+t7.7] w[+mC]=GMR57C10-GAL4}attP2	BDSC: 39171
w[1118]; PBac{681.P.FSVS-1}CG9336[CPTI001654]	DGRC: 115180, Kyoto *Drosophila* Stock Center
CS; bero[KO]/CyO Bacc[Wee-P20]	This paper

w[1118]; PBac{y[+mDint2] w[+mC]=UAS-CD4-tdTom}VK00033	BDSC: 35837
w[1118]; P{y[+t7.7] w[+mC]=GMR72F11-GAL4}attP2	BDSC: 39786
w[*]; P{w[+mC]=Ilp2-GAL4.R}2/CyO	BDSC: 37516
P{w[+mC]=GAL4-Eh.2.4}C21	BDSC: 6301
w[*]; P{w[+mW.hs]=GawB}dimm[929] crc[929]	BDSC: 25373
w[1118]; P{w[+mC]=Lk-GAL4.TH}2M	BDSC: 51993
y[1] sc[*] v[1] sev[21]; P{y[+t7.7] v[+t1.8]=VALIUM20-EGFP.shRNA.1}attP2	BDSC: 41556
w[*]; P{w[+mC]=ppk-GAL4.G}3	BDSC: 32079
w[1118]; P{y[+t7.7] w[+mC]=GMR69F06-GAL4}attP2	BDSC: 39497
w; tsh-LexA/CyO; MKRS/TM6B	J. Simpson, UCSB, Santa Barbara, USA
w; Sp/CyO; Scr-LexA/TM6B	J. Simpson, UCSB, Santa Barbara, USA
w[*]; Bl[1]/CyO; P{w[+mC]=alphaTub84B(FRT.GAL80)}3	BDSC: 38881
w[*]; P{w[+mC]=alphaTub84B(FRT.GAL80)}2/CyO; TM2/TM6B, Tb[1]	BDSC: 38880
w[1118]; P{y[+t7.7] w[+mC]=8XLexAop2-FLPL}attP40	BDSC: 55820
w[1118]; P{y[+t7.7] w[+mC]=8XLexAop2-FLPL}attP2	BDSC: 55819
w;; 20XUAS-IVS-FLAG:Bero(attP2)/TM6B, Tb1	This paper
w[*]; P{y[+t7.7] w[+mC]=10XUAS-IVS-myr::GFP}attP2	BDSC: 32197
w[1118]; P{y[+t7.7] w[+mC]=20XUAS-IVS-CsChrimson.mVenus}attP40	BDSC: 55135
w[1118]; P{y[+t7.7] w[+mC]=20XUAS-IVS-CsChrimson.mVenus}attP2	BDSC: 55136
y[1] w[*]; P{w[+mC]=UAS-CD4-tdGFP}8M2	BDSC: 35839
w[*]; TI{2A-lexA::GAD}VGlut[2A-lexA]/CyO	BDSC: 84442
w[*]; PBac{y[+mDint2] w[+mC]=20XUAS-IVS-NES-jRCaMP1b-p10}VK00005	BDSC: 63793
w[*]; P{y[+t7.7] w[+mC]=13XLexAop2-IVS-NES-jRCaMP1b-p10}su(Hw)attP5	BDSC: 64428
y[1] w[*]; PBac{y[+mDint2] w[+mC]=10XQUAS-ChR2.T159C-HA}VK00018/CyO, P{Wee-P.ph0}Bacc[Wee-P20]; Dr[1]/TM6C, Sb[1] Tb[1]	BDSC: 52259
y[1] w[*]; wg[Sp-1]/CyO, P{Wee-P.ph0}Bacc[Wee-P20]; PBac{y[+mDint2] w[+mC]=20XUAS-ChR2.T159C-HA}VK00027/TM6C, Sb[1]	BDSC: 52257
y[1] v[1]; P{y[+t7.7] v[+t1.8]=TRiP.JF01816}attP2	BDSC: 25798
y[1] v[1]; P{y[+t7.7] v[+t1.8]=TRiP.JF01822}attP2	BDSC: 25804

y[1] v[1]; P{y[+t7.7] v[+t1.8]=TRiP.JF02746}attP2	BDSC: 27667
y[1] w[*]; P{y[+t7.7] w[+mC]=TrpA1-QF.P}attP40; Dr[1]/TM6C, Sb[1] Tb[1]	BDSC: 36348
y[1] w[67c23]; P{y[+t7.7]=CaryP}attP2	BDSC: 8622
y[1] v[1]; P{y[+t7.7]=CaryP}attP40	BDSC: 36304
w[*]; P{w[+mC]=UAS-Hsap\KCNJ2.EGFP}7	BDSC: 6595
y[1] sc[*] v[1] sev[21]; P{y[+t7.7] v[+t1.8]=TRiP.HMC03643}attP40	BDSC: 52903
y[1] v[1]; P{y[+t7.7] v[+t1.8]=TRiP.JF01851}attP2	BDSC: 25833

Table S4. The detailed genotypes and source of the fly lines utilized in the study

The majority of the fly lines were obtained from the Bloomington *Drosophila* Stock Center (BDSC), unless stated otherwise.

shRNA#1 Upper	5'-ctagcagtGCACCAAGGACGAGTGCAACGtagttatatt caagcataCGTTGCACTCGTCCTTGGTGCgcg-3'
shRNA#1 Lower	5'-aattcgcGCACCAAGGACGAGTGCAACGtatgcttgaat ataactaCGTTGCACTCGTCCTTGGTGCactg-3'
shRNA#2 Upper	5'-ctagcagtCCTCTATGCCGTTCGTTAAGCtagttatatt caagcataGCTTAACGAACGGCATAGAGGgcg-3'
shRNA#2 Lower	5'-aattcgcCCTCTATGCCGTTCGTTAAGCtatgcttgaa tataactaGCTTAACGAACGGCATAGAGGactg-3'
bero RT-PCR top 5UTR primer	5'-ATGCGGCCGCCACACTCGAAGTATT CGCGAAAATGGTGTC-3'
bero RT-PCR bot Term primer	5'-ATTCTAGACTAGGCCAGCAGAC GAGCCACGCCGAAGAA-3'
αTub84B RT-PCR tub-F primer	5’-GGACGTCAACGCCGCTATTG-3’
αTub84B RT-PCR tub-R primer	5’-TTGGACAACATGCACACGGC-3’
top FLAG primer	5'-GCTGACTACAAAGACGATGACGACAAG GCTTGCTACCAGTGCGAGTCCCTCACAATG-3'
bot FLAG primer	5'-AGCCTTGTCGTCATCGTCTTTGTAGTC AGCCTTGATGGCGTAGGCCGAACAAGCCAG-3'
Upstream PCR Foward primer	5'-CTCTCGTGCCAAGATGAGC-3'
Upstream PCR Reverse primer	5'-CGAGGGTTCGAAATCGATAA-3'
Downstream PCR Foward primer	5'-AACGCAAGCAAATGTGTCAG-3'
Downstream PCR Reverse primer	5'-AAGCTAGCGCTCGATCTTGA-3'
5' Homology arm Forward primer	5’-ACCAGACGGGTCTTCCAAAG-3’
5' Homology arm Reverse primer	5’-CTTCGAGTGTGGGAATTGCT-3’
3' Homology arm Forward primer	5’-ATCTTAACTAGCTAGTAAATTACCTG-3’
3' Homology arm Reverse primer	5’-CGCCTTGCTGAAAGTTCTTC-3’
Oligo DNA for the upstream gRNA	5'-CAGACTGATCATAACGGCCA[CGG]-3'
Oligo DNA for the downstream gRNA	5'-CATCCTGCTCTTCTTCGGCG[TGG]-3'

Table S5. The detail sequences of primers and other oligonucleotides utilized in this study

References

Almagro Armenteros JJ, Tsirigos KD, Sønderby CK, Petersen TN, Winther O, Brunak S, von Heijne G, Nielsen H. 2019. SignalP 5.0 improves signal peptide predictions using deep neural networks. *Nat Biotechnol* **37**:420–423. doi:10.1038/s41587-019-0036-z

Bergland AO, Behrman EL, O'Brien KR, Schmidt PS, Petrov DA. 2014. Genomic Evidence of Rapid and Stable Adaptive Oscillations over Seasonal Time Scales in Drosophila. *PLoS Genet* **10**. doi:10.1371/journal.pgen.1004775

Berndt A, Schoenenberger P, Mattis J, Tye KM, Deisseroth K, Hegemann P, Oertner TG. 2011. High-efficiency channelrhodopsins for fast neuronal stimulation at low light levels. *Proc Natl Acad Sci U S A* **108**:7595–7600. doi:10.1073/pnas.1017210108

Bohm RA, Welch WP, Goodnight LK, Cox LW, Henry LG, Gunter TC, Bao H, Zhang B. 2010. A genetic mosaic approach for neural circuit mapping in Drosophila. *Proc Natl Acad Sci U S A* **107**:16378–16383. doi:10.1073/pnas.1004669107

Bourbia N, Ansah OB, Pertovaara A. 2010. Corticotropin-releasing factor in the rat amygdala differentially influences sensory-discriminative and emotional-like pain response in peripheral neuropathy. *J Pain* **11**:1461–1471. doi:10.1016/j.jpain.2010.05.004

Branco T, Redgrave P. 2020. The Neural Basis of Escape Behavior in Vertebrates. *Annu Rev Neurosci* **43**:417–439. doi:10.1146/annurev-neuro-100219-122527

Budde T, Meuth S, Pape HC. 2002. Calcium-dependent inactivation of neuronal calcium channels. *Nat Rev Neurosci* **3**:873–883. doi:10.1038/nrn959

Burgos A, Honjo K, Ohyama T, Qian CS, Shin GJ, Gohl DM, Silies M, Tracey WD, Zlatic M, Cardona A, Grueber WB. 2018. Nociceptive interneurons control modular motor pathways to promote escape behavior in Drosophila. *Elife* **7**:e26016. doi:10.7554/eLife.26016

Burnett CJ, Li C, Webber E, Tsaousidou E, Xue SY, Brüning JC, Krashes MJ. 2016. Hunger-Driven Motivational State Competition. *Neuron* **92**:187–201. doi:10.1016/j.neuron.2016.08.032

Burrell BD. 2017. Comparative biology of pain: What invertebrates can tell us about how nociception works. *J Neurophysiol* **117**:1461–1473. doi:10.1152/jn.00600.2016

Castro-Mondragon JA, Riudavets-Puig R, Rauluseviciute I, Berhanu Lemma R, Turchi L, Blanc-Mathieu R, Lucas J, Boddie P, Khan A, Perez NM, Fornes O, Leung TY,

Aguirre A, Hammal F, Schmelter D, Baranasic D, Ballester B, Sandelin A, Lenhard B, Vandepoele K, Wasserman WW, Parcy F, Mathelier A. 2022. JASPAR 2022: The 9th release of the open-access database of transcription factor binding profiles. *Nucleic Acids Res* **50**:D165–D173. doi:10.1093/nar/gkab1113

Chin MR, Tracey WD. 2017. Nociceptive Circuits: Can't Escape Detection. *Curr Biol* **27**:R796–R798. doi:10.1016/j.cub.2017.07.031

Choo YM, Lee BH, Lee KS, Kim BY, Li J, Kim JG, Lee JH, Sohn HD, Nah SY, Jin BR. 2008. Pr-lynx1, a modulator of nicotinic acetylcholine receptors in the insect. *Mol Cell Neurosci* **38**:224–235. doi:10.1016/j.mcn.2008.02.011

Corrales M, Cocanougher BT, Kohn AB, Wittenbach JD, Long XS, Lemire A, Cardona A, Singer RH, Moroz LL, Zlatic M. 2022. A single - cell transcriptomic atlas of complete insect nervous systems across multiple life stages. *Neural Development* **17** 1–23. doi:10.1186/s13064-022-00164-6

Dana H, Mohar B, Sun Y, Narayan S, Gordus A, Hasseman JP, Tsegaye G, Holt GT, Hu A, Walpita D, Patel R, Macklin JJ, Bargmann CI, Ahrens MB, Schreiter ER, Jayaraman V, Looger LL, Svoboda K, Kim DS. 2016. Sensitive red protein calcium indicators for imaging neural activity. *Elife* **5**:1–24. doi:10.7554/eLife.12727

Dason JS, Cheung A, Anreiter I, Montemurri VA, Allen AM, Sokolowski MB. 2019. Drosophila foraging regulates a nociceptive-like escape behavior through a developmentally plastic sensory circuit. *Proc Natl Acad Sci* **117**:23286–23291. doi:10.1073/pnas.1820840116

De Haro M, Al-Ramahi I, Benito-Sipos J, López-Arias B, Dorado B, Veenstra JA, Herrero P. 2010. Detailed analysis of leucokinin-expressing neurons and their candidate functions in the Drosophila nervous system. *Cell Tissue Res* **339**:321–336. doi:10.1007/s00441-009-0890-y

Eisenhaber B, Bork P, Eisenhaber F. 1999. Prediction of potential GPI-modification sites in proprotein sequences. *J Mol Biol* **292**:741–758. doi:10.1006/jmbi.1999.3069

Fadok JP, Krabbe S, Markovic M, Courtin J, Xu C, Massi L, Botta P, Bylund K, Müller C, Kovacevic A, Tovote P, Lüthi A. 2017. A competitive inhibitory circuit for selection of active and passive fear responses. *Nature* **542**:96–99. doi:10.1038/nature21047

Flavell SW, Gogolla N, Lovett-Barron M, Zelikowsky M. 2022. The emergence and influence of internal states. *Neuron* **110**:2545-2570. doi:10.1016/j.neuron.2022.04.030

Fleury F, Ris N, Allemand R, Fouillet P, Carton Y, Boulétreau M. 2004. Ecological and genetic interactions in Drosophila-parasitoids communities: A case study with D. melanogaster, D. simulans and their common Leptopilina parasitoids in south-eastern France. *Genetica* **120**:181–194. doi:10.1023/B:GENE.0000017640.78087.9e

Gupta R, Brunak S. 2001. Prediction of glycosylation across the human proteome and the correlation to protein functionPacific Symposium on Biocomputing 2002. pp. 310–322.

Hijazi A, Masson W, Augé B, Waltzer L, Haenlin M, Roch F. 2009. Boudin is required for septate junction organisation in Drosophila and codes for a diffusible protein of the Ly6 superfamily. *Development* **136**:2199–2209. doi:10.1242/dev.033845

Hu C, Petersen M, Hoyer N, Spitzweck B, Tenedini F, Wang D, Gruschka A, Burchardt LS, Szpotowicz E, Schweizer M, Guntur AR, Yang C, Soba P. 2017. Sensory integration and neuromodulatory feedback facilitate Drosophila mechanonociceptive behavior. *Nat Neurosci* **20**:1085–1095. doi:10.1038/nn.4580

Hu Y, Wang C, Yang L, Pan G, Liu H, Yu G, Ye B. 2020. A Neural Basis for Categorizing Sensory Stimuli to Enhance Decision Accuracy. *Curr Biol* 30:4896–4909. doi:10.1016/j.cub.2020.09.045

Huang W, Massouras A, Inoue Y, Peiffer J, Ràmia M, Tarone AM, Turlapati L, Zichner T, Zhu D, Lyman RF, Magwire MM, Blankenburg K, Carbone MA, Chang K, Ellis LL, Fernandez S, Han Y, Highnam G, Hjelmen CE, Jack JR, Javaid M, Jayaseelan J, Kalra D, Lee S, Lewis L, Munidasa M, Ongeri F, Patel S, Perales L, Perez A, Pu LL, Rollmann SM, Ruth R, Saada N, Warner C, Williams A, Wu YQ, Yamamoto A, Zhang Y, Zhu Y, Anholt RRH, Korbel JO, Mittelman D, Muzny DM, Gibbs RA, Barbadilla A, Johnston JS, Stone EA, Richards S, Deplancke B, Mackay TFC. 2014. Natural variation in genome architecture among 205 Drosophila melanogaster Genetic Reference Panel lines. *Genome Res* **24**:1193–1208. doi:10.1101/gr.171546.113

Hwang RY, Stearns NA, Tracey WD. 2012. The ankyrin repeat domain of the trpa protein painless is important for thermal nociception but not mechanical nociception. *PLoS One* **7**. doi:10.1371/journal.pone.0030090

Hwang RY, Zhong L, Xu Y, Johnson T, Zhang F, Deisseroth K, Carolina N. 2007. Nociceptive Neurons Protect Drosophila Larvae from Parasitoid Wasps *Curr Biol* **17**:2105–2116. doi:10.1016/j.cub.2007.11.029

Im SH, Galko MJ. 2012. Pokes, sunburn, and hot sauce: Drosophila as an emerging model for the biology of nociception. *Dev Dyn* **241**:16–26. doi:10.1002/dvdy.22737

Imambocus BN, Zhou F, Formozov A, Wittich A, Tenedini FM, Hu C, Sauter K, Macarenhas Varela E, Herédia F, Casimiro AP, Macedo A, Schlegel P, Yang CH, Miguel-Aliaga I, Wiegert JS, Pankratz MJ, Gontijo AM, Cardona A, Soba P. 2022. A neuropeptidergic circuit gates selective escape behavior of Drosophila larvae. *Curr Biol* **32**:149-163.e8. doi:10.1016/j.cub.2021.10.069

Itoga CA, Roltsch Hellard EA, Whitaker AM, Lu YL, Schreiber AL, Baynes BB, Baiamonte BA, Richardson HN, Gilpin NW. 2016. Traumatic Stress Promotes Hyperalgesia via Corticotropin-Releasing Factor-1 Receptor (CRFR1) Signaling in

Central Amygdala. *Neuropsychopharmacology* **41**:2463–2472. doi:10.1038/npp.2016.44

Jennings EM, Okine BN, Roche M, Finn DP. 2014. Stress-induced hyperalgesia. *Prog Neurobiol* **121**:1–18. doi:10.1016/j.pneurobio.2014.06.003

Ji G, Fu Y, Adwanikar H, Neugebauer V. 2013. Non-pain-related CRF1 activation in the amygdala facilitates synaptic transmission and pain responses. *Mol Pain* **9**:11–15. doi:10.1186/1744-8069-9-2

Johnson AC, Tran L, Greenwood-Van Meerveld B. 2015. Knockdown of corticotropin-releasing factor in the central amygdala reverses persistent viscerosomatic hyperalgesia. *Transl Psychiatry* **5**:e517. doi:10.1038/tp.2015.16

Jovanic T, Schneider-Mizell CM, Shao M, Masson JB, Denisov G, Fetter RD, Mensh BD, Truman JW, Cardona A, Zlatic M. 2016. Competitive Disinhibition Mediates Behavioral Choice and Sequences in Drosophila. *Cell* **167**:858-870.e19. doi:10.1016/j.cell.2016.09.009

Jumper J, Evans R, Pritzel A, Green T, Figurnov M, Ronneberger O, Tunyasuvunakool K, Bates R, Žídek A, Potapenko A, Bridgland A, Meyer C, Kohl SAA, Ballard AJ, Cowie A, Romera-Paredes B, Nikolov S, Jain R, Adler J, Back T, Petersen S, Reiman D, Clancy E, Zielinski M, Steinegger M, Pacholska M, Berghammer T, Bodenstein S, Silver D, Vinyals O, Senior AW, Kavukcuoglu K, Kohli P, Hassabis D. 2021. Highly accurate protein structure prediction with AlphaFold. *Nature* **596**:583–589. doi:10.1038/s41586-021-03819-2

Kaneko T, Macara AM, Li R, Yang C, Kaneko T, Macara AM, Li R, Hu Y, Iwasaki K, Dunnings Z, Firestone E. 2017. Serotonergic Modulation Enables Pathway-Specific Plasticity in a Developing Sensory Circuit in Drosophila. *Neuron* **95**:623–638.e4. doi:10.1016/j.neuron.2017.06.034

Khan SJ, Abidi SNF, Skinner A, Tian Y, Smith-Bolton RK. 2017. The Drosophila Duox maturation factor is a key component of a positive feedback loop that sustains regeneration signaling. *PLoS Genetics* **13**:e1006937. doi:10.1371/journal.pgen.1006937

Kim YJ, Žitňan D, Galizia CG, Cho KH, Adams ME. 2006. A Command Chemical Triggers an Innate Behavior by Sequential Activation of Multiple Peptidergic Ensembles. *Curr Biol* **16**:1395–1407. doi:10.1016/j.cub.2006.06.027

Klapoetke NC, Murata Y, Kim SS, Pulver SR, Birdsey-Benson A, Cho YK, Morimoto TK, Chuong AS, Carpenter EJ, Tian Z, Wang J, Xie Y, Yan Z, Zhang Y, Chow BY, Surek B, Melkonian M, Jayaraman V, Constantine-Paton M, Wong GK-S, Boyden ES. 2014. Independent optical excitation of distinct neural populations. *Nat Methods* **11**:338–346. doi:10.1038/nmeth.2836

Kondo S, Ueda R. 2013. Highly Improved gene targeting by germline-specific Cas9

expression in Drosophila. *Genetics* **195**:715–721. doi:10.1534/genetics.113.156737

Krogh A, Larsson B, Von Heijne G, Sonnhammer ELL. 2001. Predicting transmembrane protein topology with a hidden Markov model: Application to complete genomes. *J Mol Biol* **305**:567–580. doi:10.1006/jmbi.2000.4315

Lippert C, Listgarten J, Liu Y, Kadie CM, Davidson RI, Heckerman D. 2011. FaST linear mixed models for genome-wide association studies. *Nat Methods* **8**:833–835. doi:10.1038/nmeth.1681

Liu Y, Luo J, Carlsson MA, Nässel DR. 2015. Serotonin and insulin-like peptides modulate leucokinin-producing neurons that affect feeding and water homeostasis in Drosophila. *J Comp Neurol* **523**:1840–1863. doi:10.1002/cne.23768

Liu Z, Cao G, Li J, Bao H, Zhang Y. 2009. Identification of two Lynx proteins in Nilaparvata lugens and the modulation on insect nicotinic acetylcholine receptors. *J Neurochem* **110**:1707–1714. doi:10.1111/j.1471-4159.2009.06274.x

Long AD, Macdonald SJ, King EG. 2014. Dissecting complex traits using the Drosophila Synthetic Population Resource. *Trends Genet* **30**:488–495. doi:10.1016/j.tig.2014.07.009

Loughner CL, Bruford EA, McAndrews MS, Delp EE, Swamynathan S, Swamynathan SK. 2016. Organization, evolution and functions of the human and mouse Ly6/uPAR family genes. *Hum Genomics* **10**:10. doi:10.1186/s40246-016-0074-2

Lowe N, Rees JS, Roote J, Ryder E, Armean IM, Johnson G, Drummond E, Spriggs H, Drummond J, Magbanua JP, Naylor H, Sanson B, Bastock R, Huelsmann S, Trovisco V, Landgraf M, Knowles-Barley S, Douglas Armstrong J, White-Cooper H, Hansen C, Phillips RG, Azevedo R, Bailey AP, Battisti V, Belaya K, Bergstralh D, Bloor JW, Booth H, Brand AH, Bray S, Brown NH, Brown S, Chang C wen, Chell J, Coiffic A, Cols M, Cranston M, Davidson CM, Davis I, Dods JS, Doerflinger H, Edoff K, Egger B, Faria C, Gold KS, Gould AP, Gregory LM, Gubb D, Flower R, Hall J, Huen D, Inoue Y, Jarman A, Kyriacou C, Le Droguen PM, Lenoir O, Lye C, Ma L, Gutierrez Mazariegos J, McNeilly L, Maitra S, Mirouse V, Morais de Sa E, Nashchekin D, Nieuwburg R, Okkenhaug H, Pezeron G, Raghu P, Roberts I, Rosato E, Sehadova´ H, Southall TD, Speder P, Stanewsky R, Szabo G, Szular J, Tear G, Thompson ARC, Valles AM, Vega-Rioja A, Welchman DP, Wheatley L, White RH, Zwart M, Lilley KS, Russell S, Johnston DS. 2014. Analysis of the expression patterns, Subcellular localisations and interaction partners of drosophila proteins using a pigp protein trap library. *Development* **141**:3994–4005. doi:10.1242/dev.111054

Luo J, Liu Y, Nässel DR. 2013. Insulin/IGF-Regulated Size Scaling of Neuroendocrine Cells Expressing the bHLH Transcription Factor Dimmed in Drosophila. *PLoS Genet* **9**. doi:10.1371/journal.pgen.1004052

Mackay TFC, Huang W. 2018. Charting the genotype–phenotype map: lessons from the

Drosophila melanogaster Genetic Reference Panel. *Wiley Interdiscip Rev Dev Biol* **7**:1–18. doi:10.1002/wdev.289

MacKay TFC, Richards S, Stone EA, Barbadilla A, Ayroles JF, Zhu D, Casillas S, Han Y, Magwire MM, Cridland JM, Richardson MF, Anholt RRH, Barrón M, Bess C, Blankenburg KP, Carbone MA, Castellano D, Chaboub L, Duncan L, Harris Z, Javaid M, Jayaseelan JC, Jhangiani SN, Jordan KW, Lara F, Lawrence F, Lee SL, Librado P, Linheiro RS, Lyman RF, MacKey AJ, Munidasa M, Muzny DM, Nazareth L, Newsham I, Perales L, Pu LL, Qu C, Ràmia M, Reid JG, Rollmann SM, Rozas J, Saada N, Turlapati L, Worley KC, Wu YQ, Yamamoto A, Zhu Y, Bergman CM, Thornton KR, Mittelman D, Gibbs RA. 2012. The Drosophila melanogaster Genetic Reference Panel. *Nature* **482**:173–178. doi:10.1038/nature10811

Mohammad F, Stewart JC, Ott S, Chlebikova K, Chua JY, Koh T-W, Ho J, Claridge-Chang A. 2017. Optogenetic inhibition of behavior with anion channelrhodopsins. *Nat Methods* **14**:271–274. doi:10.1038/nmeth.4148

Mu Y, Li X quan, Zhang B, Du J lin. 2012. Visual Input Modulates Audiomotor Function via Hypothalamic Dopaminergic Neurons through a Cooperative Mechanism. *Neuron* **75**:688–699. doi:10.1016/j.neuron.2012.05.035

Nässel DR, Winther ÅME. 2010. Drosophila neuropeptides in regulation of physiology and behavior. *Prog Neurobiol* **92**:42–104. doi:10.1016/j.pneurobio.2010.04.010

Ni JQ, Markstein M, Binari R, Pfeiffer B, Liu LP, Villalta C, Booker M, Perkins L, Perrimon N. 2008. Vector and parameters for targeted transgenic RNA interference in Drosophila melanogaster. *Nat Methods* **5**:49–51. doi:10.1038/nmeth1146

Oh Y, Lai JSY, Min S, Huang HW, Liberles SD, Ryoo HD, Suh GSB. 2021. Periphery signals generated by Piezo-mediated stomach stretch and Neuromedin-mediated glucose load regulate the Drosophila brain nutrient sensor. *Neuron* **109**:1979-1995.e6. doi:10.1016/j.neuron.2021.04.028

Ohyama T, Schneider-Mizell CM, Fetter RD, Aleman JV, Franconville R, Rivera-Alba M, Mensh BD, Branson KM, Simpson JH, Truman JW, Cardona A, Zlatic M. 2015. A multilevel multimodal circuit enhances action selection in Drosophila. *Nature* **520**:633–9. doi:10.1038/nature14297

Okusawa S, Kohsaka H, Nose A. 2014. Serotonin and Downstream Leucokinin Neurons Modulate Larval Turning Behavior in Drosophila. *J Neurosci*. **34**:2544–2558 doi:10.1523/JNEUROSCI.3500-13.2014

Onodera K, Baba S, Murakami A, Uemura T, Usui T. 2017. Small conductance Ca2+-activated K+ channels induce the firing pause periods during the activation of drosophila nociceptive neurons. *Elife* **6**:1–17. doi:10.7554/eLife.29754.001

Peirs C, Seal RP. 2016. Neural circuits for pain: Recent advances and current views. *Science* **354**:578–584. doi:10.1126/science.aaf8933

Risse B, Berh D, Otto N, Klämbt C, Jiang X. 2017. FIMTrack: An open source tracking and locomotion analysis software for small animals. *PLoS Comput Biol* **13**:1–15. doi:10.1371/journal.pcbi.1005530

Simpson JH. 2016. Rationally subdividing the fly nervous system with versatile expression reagents. *J Neurogenet* **30**:185–194. doi:10.1080/01677063.2016.1248761

Taghert PH, Nitabach MN. 2012. Peptide Neuromodulation in Invertebrate Model Systems. *Neuron* **76**:82–97. doi:10.1016/j.neuron.2012.08.035

Takagi S, Cocanougher BT, Niki S, Miyamoto D, Kohsaka H, Kazama H, Fetter RD, Truman JW, Zlatic M, Cardona A, Nose A. 2017. Divergent Connectivity of Homologous Command-like Neurons Mediates Segment-Specific Touch Responses in Drosophila. *Neuron* **96**:1373–1387. doi:10.1016/j.neuron.2017.10.030

Terada SI, Matsubara D, Onodera K, Matsuzaki M, Uemura T, Usui T. 2016. Neuronal processing of noxious thermal stimuli mediated by dendritic Ca2+ influx in Drosophila somatosensory neurons. *Elife* **5**:1–26. doi:10.7554/eLife.12959

Tracey WD, Wilson RI, Laurent G, Benzer S. 2003. painless, a Drosophila gene essential for nociception. *Cell* **113**:261–273. doi:10.1016/S0092-8674(03)00272-1

Tsetlin VI. 2015. Three-finger snake neurotoxins and Ly6 proteins targeting nicotinic acetylcholine receptors: Pharmacological tools and endogenous modulators. *Trends Pharmacol Sci* **36**:109–123. doi:10.1016/j.tips.2014.11.003

Turner HN, Armengol K, Patel AA, Himmel NJ, Sullivan L, Iyer SC, Bhattacharya S, Iyer EPR, Landry C, Galko MJ, Cox DN. 2016. The TRP Channels Pkd2, NompC, and Trpm Act in Cold-Sensing Neurons to Mediate Unique Aversive Behaviors to Noxious Cold in Drosophila. *Curr Biol* **26**:3116–3128. doi:10.1016/j.cub.2016.09.038

Veenstra JA, Khammassi H. 2017. Rudimentary expression of RYamide in Drosophila melanogaster relative to other Drosophila species points to a functional decline of this neuropeptide gene. *Insect Biochem Mol Biol* **83**:68–79. doi:10.1016/j.ibmb.2017.03.001

Wietek J, Rodriguez-Rozada S, Tutas J, Tenedini F, Grimm C, Oertner TG, Soba P, Hegemann P, Simon Wiegert J. 2017. Anion-conducting channelrhodopsins with tuned spectra and modified kinetics engineered for optogenetic manipulation of behavior. *Sci Rep* **7**:1–18. doi:10.1038/s41598-017-14330-y

Wu M, Robinson JE, Joiner WJ. 2014. SLEEPLESS is a bifunctional regulator of excitability and cholinergic synaptic transmission. *Curr Biol* **24**:621–629. doi:10.1016/j.cub.2014.02.026

Wu MN, Joiner WJ, Dean T, Yue Z, Smith CJ, Chen D, Hoshi T, Sehgal A, Koh K. 2010. SLEEPLESS, a Ly-6/neurotoxin family member, regulates the levels, localization and activity of Shaker. *Nat Neurosci* **13**:69–75. doi:10.1038/nn.2454

Xiang Y, Yuan Q, Vogt N, Looger LL, Jan LY, Jan YN. 2010. Light-avoidance-mediating photoreceptors tile the Drosophila larval body wall. *Nature* **468**:921–926. doi:10.1038/nature09576

Yoshino J, Morikawa RK, Hasegawa E, Emoto K. 2017. Neural Circuitry that Evokes Escape Behavior upon Activation of Nociceptive Sensory Neurons in Drosophila Larvae. *Curr Biol* **27**:2499–2504. doi:10.1016/j.cub.2017.06.068

Zandawala M, Marley R, Davies SA, Nässel DR. 2018a. Characterization of a set of abdominal neuroendocrine cells that regulate stress physiology using colocalized diuretic peptides in Drosophila. *Cell Mol Life Sci* **75**:1099–1115. doi:10.1007/s00018-017-2682-y

Zandawala M, Yurgel ME, Texada MJ, Liao S, Rewitz KF, Keene AC, Nässel DR. 2018b. Modulation of Drosophila post-feeding physiology and behavior by the neuropeptide leucokinin. *PLoS genetics* **14**: e1007767 doi:10.1371/journal.pgen.1007767

Zhong L, Bellemer A, Yan H, Honjo K, Robertson J, Hwang RY, Pitt GS, Tracey WD. 2012. Thermosensory and Nonthermosensory Isoforms of Drosophila melanogaster TRPA1 Reveal Heat-Sensor Domains of a ThermoTRP Channel. *Cell Rep* **1**:43–55. doi:10.1016/j.celrep.2011.11.002